REPORT 1252

QUASI-CYLINDRICAL THEORY OF WING-BODY INTERFERENCE AT SUPERSONIC SPEEDS AND COMPARISON WITH EXPERIMENT [1]

By JACK N. NIELSEN

SUMMARY

A theoretical method is presented for calculating the flow field about a wing-body combination employing bodies deviating only slightly in shape from a circular cylinder. If the combination possesses a horizontal plane of symmetry, no restrictions are required on wing plan form in the application of the method to the zero angle-of-attack condition. If the combination is lifting, the method requires that the wing leading edges be supersonic. Then the extent of the flow field that can be calculated depends on the wing aspect ratio and whether or not the trailing edges are supersonic. Two methods of calculating the flow field, the W-function method and the multipole method, are presented. The methods as presented are accurate to the order of quasi-cylindrical theory.

The method is applied to the calculation of the pressure field acting between a circular cylindrical body and a rectangular wing. These calculations are for combinations for which the effective aspect ratio of the wing panels joined together is greater than 2 and for which the effective chord-radius ratio is 4 or less. Two cases are calculated, the case in which the body remains at zero angle of attack while the wing incidence is varied and the case in which the wing remains at zero angle of incidence while the body angle of attack is varied. It was found that four Fourier components of the interference field are required to establish the pressure field, but that only one component is necessary to establish the span loading. A detailed discussion of the physical nature of the interference pressure field is given.

An experiment was performed especially for the purpose of checking the calculative examples. The investigation was performed at Mach numbers of 1.48 and 2.00 with a rectangular wing and body combination. Both the variable wing-incidence and angle-of-attack cases were covered. It was found that for sufficiently small angles, about 2° or less, the present method predicts the pressure distributions within about ±10 percent for both cases. Important nonlinear effects were found for angles of attack and incidence of 4° to 6°, and important viscous effects were usually found where laminar boundary layers encountered shock waves.

INTRODUCTION

In recent years the problems of supersonic wing-body interference have occupied the attention of many workers in aerodynamics. The large amount of effort expended on the subject is a result of the important effects that interference can have on the overall aerodynamic characteristics of wing-body combinations. The trend toward using large bodies and small wings at supersonic speeds, especially for missiles, is the prime reason for the increased importance of wing-body interference at these speeds.

Much significant work has already been done in the field. In reference 1, Spreiter has shown that when a wing-body combination is slender in the sense of his paper simple expressions for the lift and moment coefficients can be derived. These results were obtained by reducing a three-dimensional problem for the wave equation to a two-dimensional problem for Laplace's equation. Another approach is that of simplifying the differential equation by using conical boundaries. Following this approach, Browne, Friedman, and Hodes in reference 2 obtained a solution for the pressure field of a wing-body combination composed of a flat triangular wing and a cone both with a common apex. The use of all-conical boundaries reduces the problem to one of conical flow for which powerful methods of solution are available.

Several investigators have presented methods for determining the pressure field, including the effect of interference, acting on wing-body combinations employing circular fuselages and wings not necessarily slender. In reference 3, Ferrari has given an approximate method of obtaining the "interference of the wing on the streamlined body, assuming that the induced field generated by the wing is that which would exist around the wing if it were placed in the uniform stream alone." Similarly, the interference of the body on the wing has been determined. The results of Ferrari thus represent a first approximation, and while a second approximation using the method is possible in principle it appears that too much labor would be involved. Morikawa in reference 4 has obtained an approximate solution by solving a boundary-value problem and has also obtained a closed solution by approximating the three-dimensional model by a planar model. Bolton-Shaw in reference 5 has obtained a solution by satisfying boundary conditions at a finite number of points rather than over a surface.

Another method for estimating the effect of interference on the aerodynamic properties of wing-body combinations which are not necessarily slender is given in reference 6. In this reference the method is applied to determining the drag of symmetrical wing-body combinations; it is also applicable to the calculations of the lifting pressures acting on combinations employing wings with supersonic edges. In

[1] Supersedes NACA TN 2677 "Wing-Body Interference at Supersonic Speeds With an Application to Combinations With Rectangular Wings," by Jack N. Nielsen and William C. Pitts, 1952, and NACA TN 3128 "Comparison Between Theory and Experiment for Interference Pressure Field Between Wing and Body at Supersonic Speeds," by William C. Pitts, Jack N. Nielsen, and Maurice P. Gionfriddo, 1954.

reference 7, an essentially new method of solving a wide class of wing-body interference problems has been presented. The method is based on decomposing the interference of a wing-body combination into a number of Fourier components and solving the problem for each component in a manner similar to that used by von Kármán and Moore in reference 8 for bodies of revolution.

Phinney, reference 9, has compared the methods of references 3, 6, and 7 by applying each to the calculation of the pressure field acting on a circular cylinder intersected by an oblique shock wave. In reference 10 the theory of reference 7 has been applied to the computation of the pressure distributions acting on a rectangular wing and body combination with the body at zero angle of attack and the wing at incidence. In reference 11 Bailey and Phinney have applied the method of reference 7 to the calculation of the pressures on the body of a rectangular wing and body combination at angle of attack but with the wing at zero angle of attack. In reference 12 the same authors have compared their calculations with some experimental measurements made at a Mach number of 1.9. In reference 13 the experimental pressure distributions acting on a rectangular wing and body combination at Mach number 1.48 and 2.00 are extensively compared with theoretical calculations based on the method of reference 7.

In part I of the present report the theory of wing-body interference for combinations employing quasi-cylindrical bodies is presented, including recent developments not previously reported in references 7, 10, or 13. The theory is applicable to combinations at zero angle of attack with horizontal planes of symmetry or combinations at angle of attack if the wing leading edges are supersonic. In part II the theory is applied to the calculation of the pressures and span loadings for a rectangular wing and body combination for the case of the body at zero angle of attack and variable wing incidence and for the case of the wing at zero wing incidence and variable body angle of attack. The calculations for the second case are more complete than hitherto. In part III extensive comparison is made between the calculations of part II and the result of experiments at Mach numbers of 1.48 and 2.00 especially designed to check the calculations.

SYMBOLS

a	body radius, in.
A	aspect ratio of wing formed by joining exposed half-wings together
c	chord of rectangular wing, in.
c^*	effective chord-radius ratio, $\frac{c}{\beta a}$
$c_{2n}(x)$	strength of multipole of order $2n$ at point x of body axis
c_r	chord at wing-body juncture, in.
c_t	chord at wing tip, in.
$C_{2n}(s)$, $D_{2n}(s)$	arbitrary functions of s
$f_{2n}(x)$	velocity amplitude function of nth Fourier component, in./sec
i_W	wing-incidence angle, radians except where otherwise designated, positive for trailing edge down
$I_{2n}(s)$, $K_{2n}(s)$	modified Bessel functions of the first and second kinds, respectively
k_W	$\frac{L_{WC}}{L_W}$, $\alpha_B=0$
K_W	$\frac{L_{WC}}{L_W}$, $i_W=0$
L	lift of combination back to wing trailing edge, lb; Laplace transform operator
L^{-1}	inverse Laplace transform operator
L_W	lift on exposed half-wings joined together, lb
L_{WC}	lift on exposed half-wings in combination with body, lb
m	index identifying sets of multipole solutions
M	free-stream Mach number
$M_{2n}(x)$	characteristic functions for obtaining multipole strengths
n	number of Fourier component
p	static pressure, lb/sq in.
p_o	static pressure in free stream, lb/sq in.
p_1	static pressure at any particular orifice of wing-body combination when $\alpha_B=i_W=0$, lb/sq in.
p_T	static pressure at wind-tunnel wall orifice, lb/sq in.
P	pressure coefficient, $\frac{p-p_1}{q_o}$; $-\frac{2u}{V}$ for theoretical calculations
P_{2n}	interference pressure coefficient due to nth Fourier component
q_o	free-stream dynamic pressure, lb/sq in.
q_T	dynamic pressure based on condition at wall orifice of wind tunnel, lb/sq in.
r,θ,x	cylindrical coordinates: $y=r\cos\theta$, $z=r\sin\theta$ (See fig. 1.)
R	Reynolds number based on wing-chord length
$R.P.$	real part
s	semispan of wind-body combination, in.; Laplace transform of x coordinate
u,v,w	axial, lateral, and vertical perturbation velocities, respectively, in./sec
V	free-stream velocity, in./sec
$W_{2n}(x,r)$	characteristic functions for calculating pressure coefficient
x,y,z	Cartesian coordinates: x, axial coordinate; y, lateral coordinate; z, vertical coordinate, in. (See fig. 1.)
α_B	body angle of attack, radians except where otherwise designated
α_u	upwash angle of body-alone flow, radians
α_W	wing angle of attack, radians
β	$\sqrt{M^2-1}$
βA	effective aspect ratio
$\delta(x)$	Dirac delta function; $\delta(x)=0$, $x\neq 0$; $\int_{-\infty}^{+\infty}\delta(x)dx=1$
θ	polar angle (See fig. 1.)
λ	taper, $\frac{c_t}{c_r}$
ξ	dummy variable of integration
Λ	sweep angle of wing leading edge

φ	interference perturbation velocity potential
φ_{2n}	nth Fourier component perturbation velocity potential
φ_C	combination perturbation velocity potential
φ_W	wing-alone perturbation velocity potential
φ_{W_R}	wing-alone perturbation velocity potential due to the exposed right half of the wing
φ_{W_L}	wing-alone perturbation velocity potential due to the exposed left half of the wing
φ_{W_B}	wing-alone perturbation velocity potential due to the portion of wing inside the region occupied by body
Φ	Laplace transform of φ

SUBSCRIPTS

L	lower surface of combination
U	upper surface of combination

I. GENERAL INTERFERENCE THEORY

PHYSICAL PRINCIPLES

Prior to a mathematical formulation of the wing-body interference problem, it is well to define interference and to explain how it arises. With a stationary wing or a stationary body in a uniform parallel flow, there are associated the wing-alone and body-alone flow fields. The wing-alone flow field does not, in general, produce flow tangential to the position to be occupied by the body surface. As a result an interference flow field must arise to cancel the flow field induced normal to the body by the wing. For this reason, the sum of the body-alone plus wing-alone flow fields will not be the flow field for the body and wing together. The difference between the flow field of the body and wing together and the sum of the body-alone and wing-alone flow fields is defined to be the interference flow field.

The effects of wing-body interference on the flow field of a wing-body combination are illustrated by considering separately the effects of each component on the others. For the purposes of this discussion figure 1 shows a wing-body combination divided into the part in front of the leading edge of the wing-body juncture, henceforth called the nose, the winged part and the part behind the wing trailing edge, henceforth called the afterbody. If the combination possesses a horizontal plane of symmetry and the angle of attack is zero, no restrictions on wing plan form are necessary. However, if the wing is twisted or cambered or if the nose is at angle of attack, then the wing leading edges must be supersonic for the following discussion to apply.

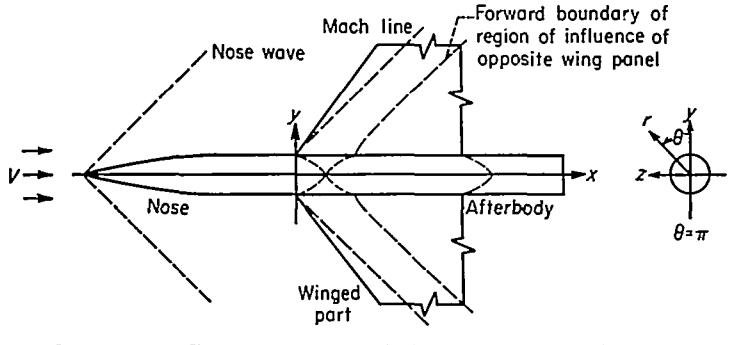

FIGURE 1.—Components of typical wing-body combination.

Effect of nose on wing.—Consider now the flow as it progresses past the body. At the body nose the flow is that around a body of revolution, and it can be treated by existing methods such as those of references 8 and 14. When the body is at angle of attack α_B, there is an upwash field in the horizontal plane of symmetry of the body. If the body is sufficiently slender, the flow field in a plane at right angles to the body axis corresponds to that around a circular cylinder in a uniform stream of velocity, $V \sin \alpha_B$. This gives an upwash field in the horizontal plane of symmetry of the body of

$$\alpha_u = \alpha_B(1+a^2/y^2) \tag{1}$$

The effect of this upwash on the wing can be obtained by considering the wing to be at angle of attack and twisted according to equation (1) and by applying the formulas of supersonic wing theory. The wing pressure field so obtained is exact, within the limitations of the theory, for that section of the wing outboard of the Mach line emanating from the leading edge of the wing-body juncture. If the wing is located close to the body nose so that there is a chordwise variation in the upwash field due to the body, then the wing is effectively cambered, and the solution is more difficult. However, for most wing-body combinations it is possible to disregard the effect of the nose, and to assume that the wing is attached to a circular cylinder that extends upstream indefinitely.

Mutual effects between body and wing.—The mutual interference between the body and wing on the winged part of a combination causes an interference field acting on the body and on the wing inboard of the Mach line emanating from the leading edge of the wing-body juncture. The wing-alone flow field does not, in general, produce flow tangential to the position to be occupied by the body surface. An interference flow field must arise that cancels the velocity induced by the wing-alone flow field normal to the body while not changing the wing shape. Alternately, the origin of the interference field can be explained in the following manner. The wing and body can be thought of as sources of pressure disturbances that radiate in all directions in downstream Mach cones. The wing disturbances which radiate toward the body are, in part, reflected back by the body onto the wing and in part transmitted onto the body giving rise to interference pressures. Likewise, the disturbances originating on the body pass onto the wing and affect the pressures there. It is apparent that the determination of the interference pressure field on the body and on the wing inboard of the Mach line of the juncture is the crux of the wing-body interference problem.

Mutual effects between wing panels.—To determine the region of influence of one wing panel on another, it is necessary to trace the path of a pulse from one wing panel across the body onto the other. The path traced across the body by the pulse originating at the leading edge of the wing-body juncture is the forward boundary of the region of influence of one wing panel on the body. (See fig. 1.) It is clearly the helix intersecting all parallel elements of the cylinder at the Mach angle. The boundary crosses the top of the body a distance of $\frac{\pi a}{2}\sqrt{M^2-1}$ downstream and reaches the opposite wing-body juncture a distance $\pi a\sqrt{M^2-1}$ downstream. A

pulse originating at a point on one wing panel and traveling to a point on the other panel can travel around the body on its surface to the opposite juncture and then along the wing to a given point, or it can leave the body tangentially before reaching the opposite wing juncture in a straight path to the point. The second means of transmitting the impulse is shorter in distance than the first and is the one which determines the forward boundary of the region of influence of one wing panel on the other. Applying this consideration to the pulse originating at the leading edge of one wing-body juncture, it is easy to show that the forward boundary of the region of influence of one wing panel on the opposite wing panel is given by the equation

$$\frac{x}{\sqrt{M^2-1}}=\left(\pi-\cos^{-1}\frac{a}{y}\right)a+\sqrt{y^2-a^2} \qquad (2)$$

This boundary is also shown in figure 1, and it becomes parallel to the Mach line at distances far from the body.

Effects on the afterbody.—As far as the interference effect of the body on the wing is concerned, it is confined to the winged part of the combination, but the effect of the wing on the body is felt also on the afterbody. For a symmetrical configuration at zero angle of attack there is no downwash in the horizontal plane of symmetry and the afterbody presents no particular problem. However, behind a lifting wing there is a downwash field. If the downwash were known everywhere in the wing wake, then the wake could be considered as an extension of the wing with twist and camber. The wing wake and afterbody could then be incorporated with the winged part of the combination and treated in the same manner. However, the actual downwash pattern in the wing wake depends on the interference effect of the body on the wing. It is thus apparent that the solution of the afterbody problem requires that the interference problem for the winged part of the combination be solved first. Only the winged part of the combination is analyzed in detail in this report.

Regions of applicability of the theory.—The present interference theory can be applied to all or part of a wing-body combination depending on the configuration and the lift. If the combination is not lifting and possesses a horizontal plane of symmetry, then the interference pressure field can be determined for the entire combination. For a lifting combination with subsonic leading edges the upwash field in front of the wing makes the present method inapplicable.

For a lifting combination with supersonic leading edges several geometric factors considerably influence the difficulty of calculating the interference field or indeed the extent to which it can be calculated. The effect of one of these factors, the sweep of the trailing edge, is illustrated in figure 2 (a). A subsonic trailing edge gives rise to multiple Mach wave reflections which greatly complicate the determination of the interference field over the rear part of the wing. Another important effect limiting the applicability of the theory is illustrated in figure 2 (b). This figure indicates that the interference field behind the incident wave can influence the tip upwash field which, in turn, influences the pressure field behind the reflected wave from the tip in a complicated way.

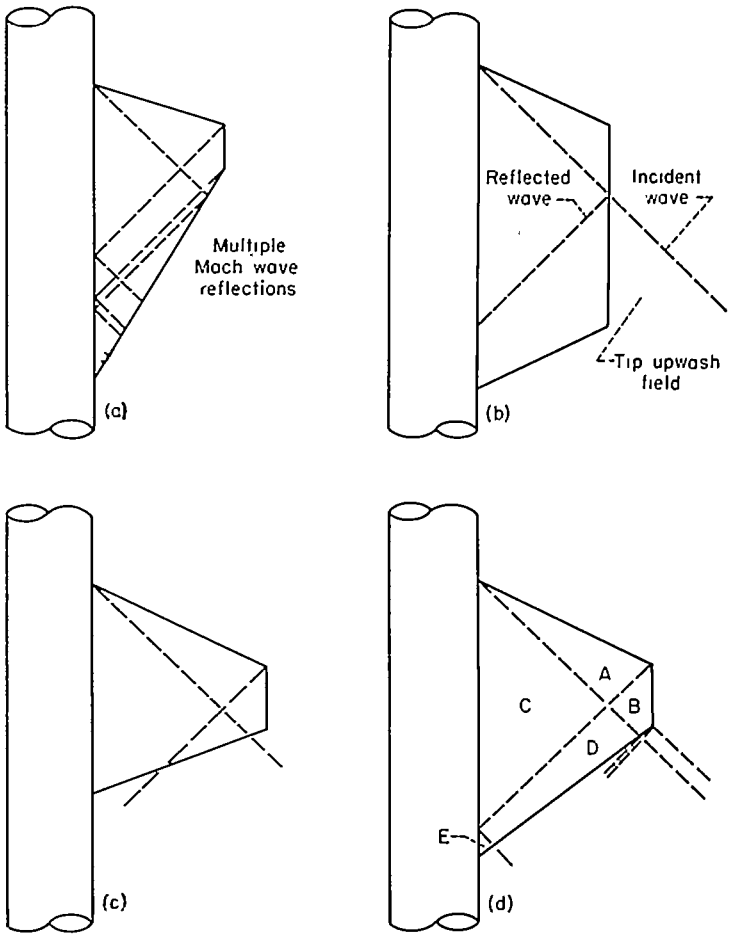

(a) Subsonic trailing edge.
(b) Effect of wing-body interference on tip upwash field.
(c) Simple case.
(d) Tractable case.

FIGURE 2.—Classes of interference problems for lifting wing and body combinations.

Avoidance of this complication requires that the incident wave intersect the trailing edge rather than the wing tip. To assure this condition, the aspect ratio must be greater than a certain minimum value in accordance with the following inequality:

$$\beta A \geq \frac{4\lambda}{(1+\lambda)\left(1-\frac{\tan\Lambda}{\beta}\right)}$$

One of the simple cases of wing-body interference for a lifting wing and body combination is shown in figure 2 (c). Here the leading and trailing edges are both supersonic, and the root-chord Mach wave intersects the trailing edge. Also the wing-tip Mach wave intersects the body downstream of the wing-body juncture so that no wing-tip effects occur on the wing interference pressure field. This condition imposes the aspect-ratio inequality:

$$\beta A \geq \frac{4}{(1+\lambda)\left(1+\frac{\tan\Lambda}{\beta}\right)}$$

Under the circumstances of this figure, the interference problem proceeds as if the combination had a horizontal plane of symmetry. Any body upwash field in front of

the wing can be treated as equivalent to a change in thickness distribution. The rectangular wing of aspect ratio greater than two is an example of the simple case, and it will be treated as an illustrative example in this paper.

An example of a tractable although fairly complicated case to which the present theory can be directed is shown in figure 2 (d). In region A the pressure field is determined as a pure wing-alone problem with any body upwash being treated as equivalent to a change in thickness distribution. In region B the problem is still a wing-alone problem which is complicated by upwash outboard of the tip. In region C there are body interference effects but no tip effects. In region D both effects prevail. In region E the tip has influenced the flow at the body surface and produced a secondary effect on the interference pressure field.

MATHEMATICAL FORMULATION OF PROBLEM

Throughout the analysis, the body radius is taken as unity and M^2 is taken as 2 so that $\beta=1$. Any formula can be generalized to any body radius by dividing all length symbols by a, and to any Mach number by dividing all streamwise lengths by β, by multiplying all pressure and lift coefficients by β, and leaving all potentials, lift forces, and span loading unaltered. It is necessary to specify the wing alone before any detailed interference calculation can be carried out. However, in the theoretical solution of the problem the wing-alone definition is arbitrary. The flow field about the combination does not depend on the definition of the wing alone.

General decomposition of boundary-value problem.—The general case of a combination at angle of attack with the wing at incidence as shown in figure 3 is considered. The mathematical details of the decomposition of this configuration into tractable configurations is carried out in detail in Appendix A following the suggestions in reference 15. A simplified discussion of the decomposition is now presented. The complete combination can be decomposed into three component configurations as shown in figure 4 (a) in which the wing boundary conditions are to be applied in the $z=0$ plane and the body conditions on the $r=1$ cylinder. Component (1) is simply the body alone, which creates an upwash field α_u in that region to be occupied by the wing in accordance with equation (1). Components (2) and (3) are combinations with wings of the same plan form; but while component (2) has a wing at angle of attack i_W, component (3) has a wing with angle of attack $-\alpha_u$. The significance of this particular method of decomposing the general wing-body problem is that component (1), the body alone, can be solved by known methods and components (2) and (3) with bodies at zero angle of attack can be solved by the methods of this report. In the wing-incidence case where $\alpha_B=0$, only configuration (2) remains. This configuration can be decomposed into a wing-alone problem and a distorted-body problem as shown in figure 4 (b). We confine our attention to this wing-incidence case for the time being.

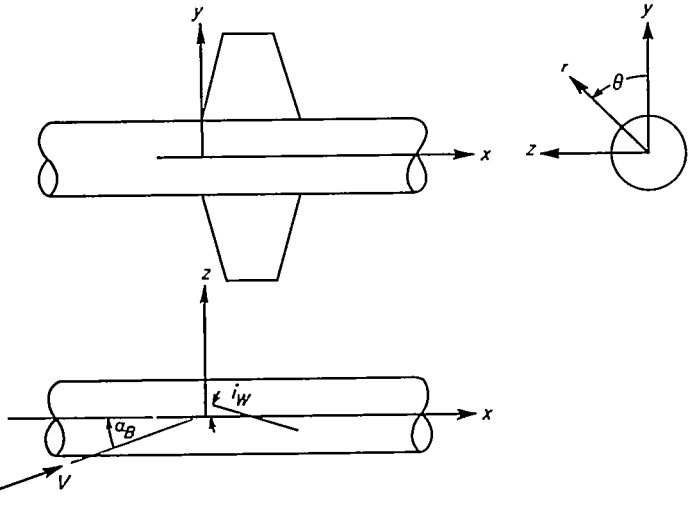

FIGURE 3.—General combination under combined effects of angle of attack and wing incidence.

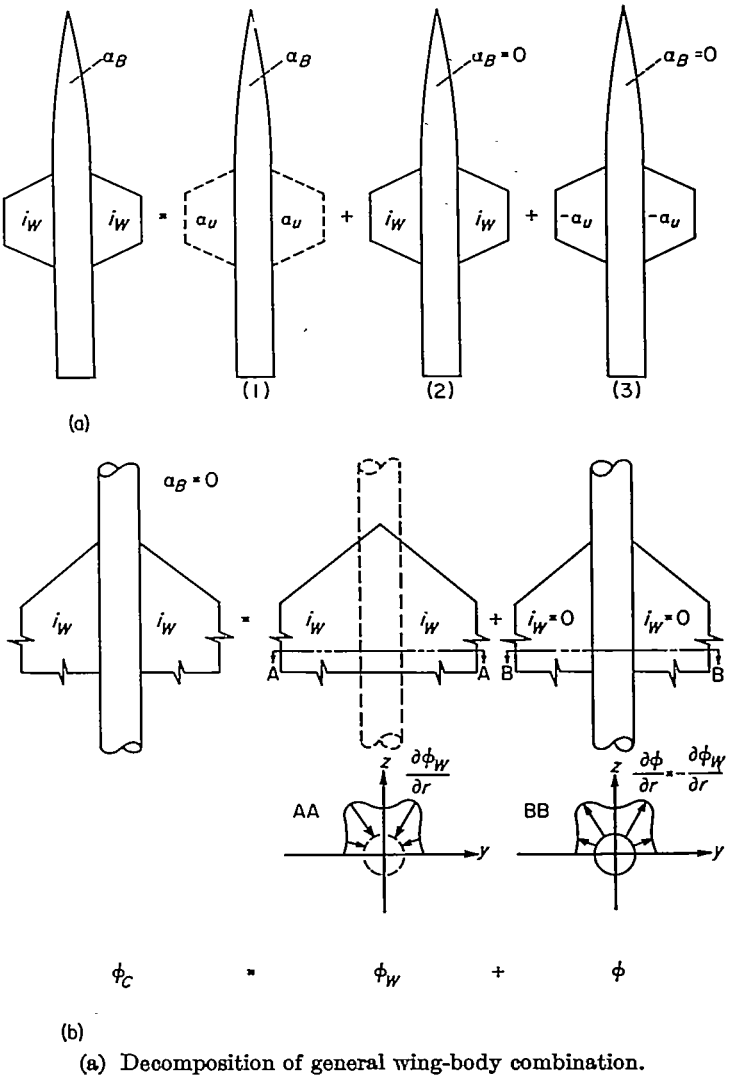

(a) Decomposition of general wing-body combination.
(b) Decomposition for wing-incidence case.

FIGURE 4.—Decomposition of wing-body combinations into simpler combinations.

Consider now a combination with the body at zero angle of attack and let φ_C be its potential. (See fig. 4(b).) This potential can be considered the sum of a wing-alone potential φ_W and of an interference potential φ.

$$\varphi_C=\varphi_W+\varphi \tag{3}$$

Since the body is an infinite circular cylinder at zero angle of attack, it produces no flow field. If the body were quasi-cylindrical with small distortions, a potential due to the body could be included in equation (3). If the body has a horizontal plane of symmetry, the inclusion of a potential due to body distortion will not change the interference potential.

The essential problem is to determine φ. First, select a convenient way of extending the wing through the body to form the wing alone, thereby specifying φ_W. The wing-alone flow field in general produces velocities $\frac{\partial \varphi_W}{\partial r}$ normal to the surface that will enclose the circular cylinder as illustrated in figure 4(b) for the region above the wing. In figure 4(b) and subsequent figures, all bodies are shown as cylinders parallel to the x axis. While the bodies of the component configurations in some cases are slightly distorted cylinders, they are nevertheless shown as true cylinders. This procedure is compatible with the fact that the boundary conditions are to be applied on a true cylinder. The value of $\frac{\partial \varphi_W}{\partial r}$ varies with θ and with x. This means that a body conforming to the wing-alone flow field is distorted in a complicated fashion. Now since the body must be circular, there must arise an interference potential φ that identically cancels $\frac{\partial \varphi_W}{\partial r}$ at the body surface, thereby straightening it.

$$\frac{\partial \varphi}{\partial r}=-\frac{\partial \varphi_W}{\partial r} \text{ at } r=1 \tag{4}$$

There are two other conditions to be fulfilled by φ. It must not distort the shape of the wing when added to φ_W to produce φ_C. Thus when $\theta=0$,

$$\frac{1}{r}\frac{\partial \varphi}{\partial \theta}=0 \tag{5}$$

or $i_W=0$ for the interference combination as shown in figure 4(b). The last condition is that the interference potential must be zero ahead of the winged part of the combination.

$$\varphi=0,\ x\leq 0 \tag{6}$$

Equations (4), (5), and (6) are the essential boundary conditions on φ.

The normal velocity $\frac{\partial \varphi}{\partial r}$ to be induced at the body surface by the interference potential can be analyzed at any given streamwise position as a Fourier cosine series. The amplitudes of the various Fourier cosine terms, $f_{2n}(x)$, vary with x, the streamwise distance. Thus,

$$\frac{\partial \varphi}{\partial r}=\sum_{n=0}^{\infty} f_{2n}(x)\cos 2n\theta=-\frac{\partial \varphi_W}{\partial r} \text{ at } r=1 \tag{7}$$

Only even multiples of θ are considered because of the vertical plane of symmetry. Consider that the interference potential is decomposed into a series of potentials such that each cancels one Fourier component of the velocity at the body surface; that is,

$$\varphi=\sum_{n=0}^{\infty} \varphi_{2n} \tag{8}$$

with

$$\frac{\partial \varphi_{2n}}{\partial r}=f_{2n}(x)\cos 2n\theta \text{ at } r=1 \tag{9}$$

Then the combination giving the interference potential φ can be decomposed in a series of combinations, each giving one of the φ_{2n} values. The decomposition is illustrated in figure 5.

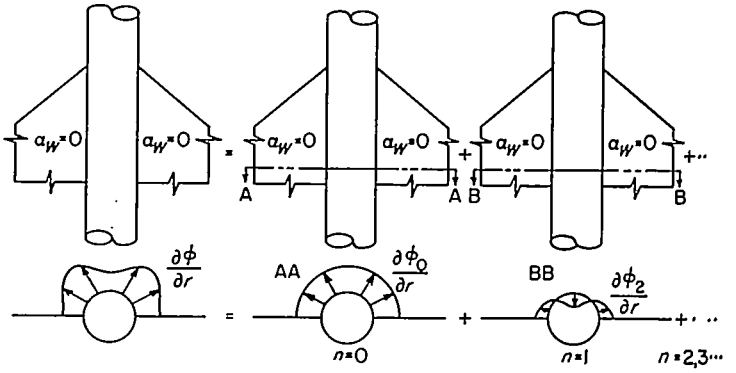

FIGURE 5.—Decomposition of interference combination into series of Fourier component interference combinations.

For $n=0$

$$\frac{\partial \varphi_0}{\partial r}=f_0(x)$$

and there is no variation of the normal velocity, pressure, or potential with θ. Thus the first interference combination is a body of revolution. The pressure field acting on the body of such a combination can be determined by the method of reference 16. This $n=0$ interference combination has the very simple significance that its flow normal to the $r=1$ cylinder, $\frac{\partial \varphi_0}{\partial r}$, subtracted from $\frac{\partial \varphi}{\partial r}$ reduces the flow across the body to zero when averaged from $\theta=0$ to $\theta=\pi$ at any streamwise location. For $n=1$,

$$\frac{\partial \varphi_2}{\partial r}=f_2(x)\cos 2\theta$$

and the normal velocity, pressure, and potential will vary as $\cos 2\theta$.

To summarize briefly, it has been shown that the general interference problem of a body and wing at different angles of attack can be broken down into wing-body problems with bodies at zero angle of attack as shown in figure 4 (a). Combinations with the body at zero angle of attack are decomposed into wings alone plus interference combinations as in figure 4 (b). The interference combinations are finally decomposed into their Fourier components as in figure 5.

A general method for determining the characteristics of any Fourier component will now be given. It will be shown that good accuracy can be obtained for the interference potential with few Fourier components.

SOLUTION BY METHOD OF W FUNCTIONS

The problem to be solved is that of a supersonic wing and body combination subject to the conditions already mentioned, but with the wing and body possibly at different angles of attack. This problem is reduced to a body-alone problem and two wing-body problems with the body at zero

angle of attack as shown in figure 4 (a). The body-alone problem can be solved by existing methods such as references 8 and 14. The procedure necessary to solve either wing-body problem as given in reference 7 is now summarized together with recent improvements.

The potentials φ_C, φ_W, and φ must all fulfill the equation of linearized compressible flow

$$(M^2-1)\varphi_{xx}-\varphi_{yy}-\varphi_{zz}=0 \tag{10}$$

If we restrict ourselves for the time being to the case $M=\sqrt{2}$ and transform equation (10) to polar coordinates, we have

$$\varphi_{rr}+\frac{1}{r}\varphi_r+\frac{1}{r^2}\varphi_{\theta\theta}-\varphi_{xx}=0 \tag{11}$$

with the coordinate system of figure 1. In solving the problem we change from the physical space, x, r, θ, to the transformed space, s, r, θ, by means of the Laplace transformation

$$L[\varphi(x)]\equiv\int_o^\infty e^{-sx}\varphi(x)dx=\Phi(s) \tag{12}$$

With the boundary condition given by equation (6) that φ is zero [2] for $x\leq 0$, equation (11) can be transformed to

$$\Phi_{rr}+\frac{1}{r}\Phi_r+\frac{1}{r^2}\Phi_{\theta\theta}-s^2\Phi=0 \tag{13}$$

Expanding Φ in a cosine series of multiples of θ, we can satisfy the boundary conditions given by equation (5), and since there is a vertical plane of symmetry, we can confine ourselves to even multiples of θ. With this restriction, general solutions to equation (13) can be written

$$\Phi=\sum_{n=0}^{\infty}\cos 2n\theta\,[C_{2n}(s)K_{2n}(sr)+D_{2n}(s)I_{2n}(sr)] \tag{14}$$

where $I_{2n}(sr)$ and $K_{2n}(sr)$ are modified Bessel functions. The constants $C_{2n}(s)$ and $D_{2n}(s)$ are arbitrary functions of s. The functions $I_{2n}(sr)$ can logically be eliminated at this point since from their asymptotic forms they can be shown to represent waves traveling upstream. The function $C_{2n}(s)$ can be evaluated by means of the remaining boundary condition given by equation (7). If we let

$$F_{2n}(s)=L[f_{2n}(x)] \tag{15}$$

then

$$C_{2n}(s)=\frac{F_{2n}(s)}{sK_{2n}'(s)} \tag{16}$$

We then have as the operational solution to our problem

$$\Phi=\sum_{n=0}^{\infty}\cos 2n\theta F_{2n}(s)\frac{K_{2n}(sr)}{sK_{2n}'(s)} \tag{17}$$

The solution can be split into the product of two transforms, one dependent on the particular boundary conditions as represented by the $F_{2n}(s)$ functions and another part independent of the boundary conditions. The inverse transform of the product of the two transforms can then be determined by the convolution integral. The part of the transform independent of the boundary condition can be thought of as defining a set of characteristic functions or influence coefficients. A tabulation of these functions allows a numerical solution of the problem for all boundary conditions.

The manner of splitting equation (17) into two transforms depends also on the existence of the inverse transforms of the parts into which it is split. Let us write equation (17) as

$$s\,\Phi=\sum_{n=0}^{\infty}\cos 2n\theta F_{2n}(s)e^{-s(r-1)}\left[\frac{e^{s(r-1)}K_{2n}(sr)}{K_{2n}'(s)}+\frac{1}{\sqrt{r}}-\frac{1}{\sqrt{r}}\right] \tag{18}$$

With the aid of the following relationships

$$L^{-1}[F_{2n}(s)e^{-s(r-1)}]=f_{2n}(x-r+1) \tag{19}$$

$$L^{-1}(s\,\Phi)=\varphi_x \tag{20}$$

and the definition of the characteristic functions

$$L^{-1}\left[e^{s(r-1)}\frac{K_{2n}(sr)}{K_{2n}'(s)}+\frac{1}{\sqrt{r}}\right]\equiv W_{2n}(x,r) \tag{21}$$

we obtain

$$\varphi_x=\sum_{n=0}^{\infty}\cos 2n\theta\left[\int_{r-1}^{x}f_{2n}(\xi-r+1)W_{2n}(x-\xi,r)d\xi-\frac{f_{2n}(x-r+1)}{\sqrt{r}}\right]$$

$$=\sum_{n=0}^{\infty}\cos 2n\theta\left[\int_{o}^{x-r+1}f_{2n}(\xi)W_{2n}(x-r+1-\xi,r)d\xi-\frac{f_{2n}(x-r+1)}{\sqrt{r}}\right] \tag{22}$$

With the aid of the $W_{2n}(x,r)$ functions, the value of φ_x, and hence the pressure or potential anywhere, can be calculated from equation (22) by numerical integration for as many harmonics as desired. This result was previously given (refs. 7 and 10) for the $r=1$ case only as

$$\varphi_x=\sum_{n=0}^{\infty}\cos 2n\theta\left[\int_{o}^{x}f_{2n}(\xi)W_{2n}(x-\xi)d\xi-f_{2n}(x)\right] \tag{23}$$

and the $W_{2n}(x)$ functions were tabulated for numerical calculation of the body pressure distributions only. The generalization of the $W_{2n}(x)$ function to $W_{2n}(x, r)$ functions by means of equation (21) is a natural extension that permits the simple calculation of the pressure anywhere in the flow field. Some mathematical properties of $W_{2n}(x, r)$ functions and methods for their evaluation by automatic computing machinery have been studied by Dr. W. Mersman of the NACA. A résumé of his results is reported in reference 18.

Properties of the $W_{2n}(x,r)$ functions.—Two important properties of the $W_{2n}(x, r)$ functions that make them useful for numerical work are that they possess no singularities in the field and their magnitudes never become large. These advantages are in distinct contrast to several disadvantages of the multipole method subsequently to be described. Curves of the $W_{2n}(x, r)$ function are presented in chart 1 for $n=0$, 1, 2, and 3 for use in numerical computations.

[2] The condition frequently stated in deriving equation (13), that $\phi_x=0$ for $x=0^+$, is not required as proven in reference (17). This is in accord with the intuitive physical idea that any step in ϕ_x at the origin can be replaced by a continuous curve which for engineering purposes can have an effect different from that of the step only in a limited local region.

A simple physical picture of the $W_{2n}(x, r)$ functions can be obtained from equation (22). Write the interference pressure coefficient [3] due to any harmonic as

$$P_{2n}=-\left(\frac{2}{V}\right)\frac{\partial\varphi_{2n}}{\partial x}=\frac{2\cos 2n\theta}{V}\left[\frac{f_{2n}(x-r+1)}{\sqrt{r}}-\int_0^{x-r+1} f_{2n}(\xi)W_{2n}(x-r+1-\xi,r)d\xi\right] \quad (24)$$

Let the velocity amplitude function be a delta function at the origin as shown in figure 6. Then

$$P_{2n}=\frac{2\cos 2n\theta}{V}\left[\frac{\delta(x-r+1)}{\sqrt{r}}-W_{2n}(x-r+1,r)\right] \quad (25)$$

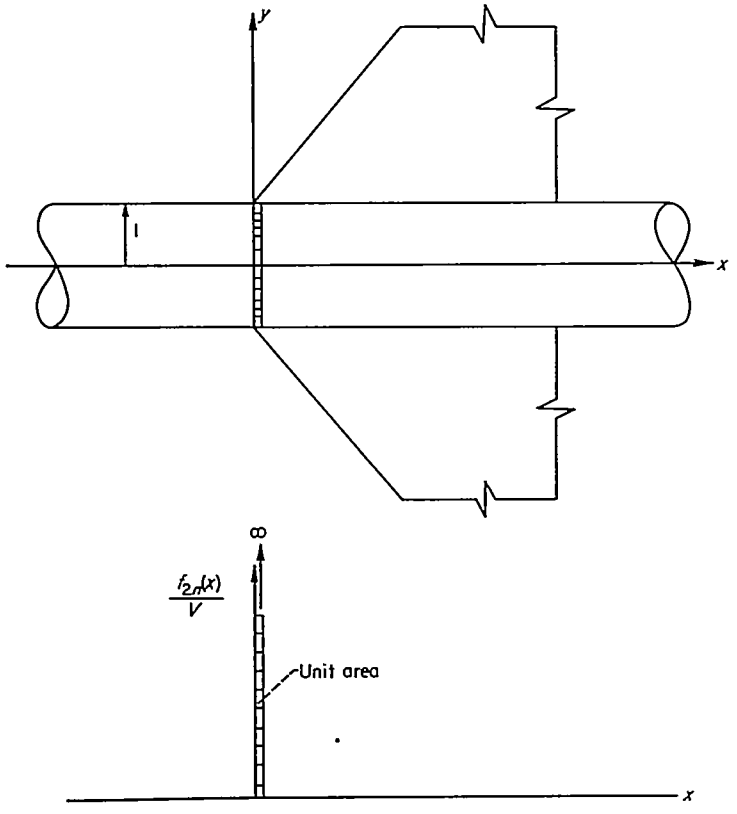

FIGURE 6.—Fourier component interference combination with "delta function" protuberence at $x=0$.

It is seen that physically the $W_{2n}(x, r)$ function represents the pressure field due to a delta function in the velocity amplitude function. The first term represents an infinite pulse propagated along the Mach cone with apex at $x=-1$ and attenuating inversely as $\sqrt{r}$. The $W_{2n}(x-r+1, r)$ term represents the overexpansion behind the bump where the pressure would be zero if the flow were two-dimensional.

Formulas for the $W_{2n}(x, r)$ functions for small x and large x can be obtained from Laplace transform theory. In fact these results are

$$W_o(x,r)\sim\frac{1}{x^2}+0\left(\frac{1}{x^3}\right) \quad (26)$$

$$W_{2n}(x,r)\sim\frac{4(r^{2n}+r^{-2n})(4n+1)!}{2^{4n+1}(2n!)^2}\left(\frac{1}{x}\right)^{4n+2} \quad (27)$$

[3] The equation for pressure coefficient to be used with equation (23) can on theoretical grounds be changed in going from the wing to the body of the configuration as discussed in reference 11. However, for simplicity, the linearized form of the Bernoulli equation is retained throughout the theoretical calculations. The contribution of the quadratic terms to the body pressure coefficient is subsequently discussed for the case of the combination at angle of attack.

$$W_o(x,r)\approx\frac{1}{8\sqrt{r}}\left(3+\frac{1}{r}\right)-\frac{3x}{128\sqrt{r}}\left(11+\frac{2}{r}+\frac{3}{r^2}\right)+0(x^2) \quad (28)$$

$$W_{2n}(0,r)=\frac{1}{8\sqrt{r}}\left[(16n^2+3)-\frac{(16n^2-1)}{r}\right] \quad (29)$$

It should be noted that the value of $W_{2n}(0, r)$ is known precisely.

SOLUTION BY METHOD OF MULTIPOLES

Multipole types.—In references 7 and 10 a multipole method was used to determine the pressure field off the body. The singularities arising in this method, together with the loss of accuracy for the higher harmonics due to large numbers, led to the development of the $W_{2n}(x, r)$ method just described. Since the multipole method has application to certain problems and since its connection to the $W_{2n}(x, r)$ method is of interest, it will be given here. In the $W_{2n}(x, r)$ method the pressure field is determined by using boundary conditions on the body surface and continuing the pressure field outward from the body. It is intuitively obvious that any quasi-cylindrical flow can be generated by distributing sources and multipoles along the body axis in variable strength. If the strength of the axial multipole distributions can be related to the body shape (velocity amplitude functions), then the entire flow field can be calculated outward from the axis.

Consider equation (14) which, with $D_{2n}(s)$ equal to zero, is

$$\Phi=\sum_{n=0}^{\infty}C_{2n}(s)\cos 2n\theta K_{2n}(sr) \quad (30)$$

This equation can be interpreted to mean that the potential is built up from a distribution of multipoles corresponding to the inverse transform of $\cos 2n\theta K_{2n}(sr)$ along the x axis in strength $c_{2n}(x)$. However, there are many possible sets of multipoles corresponding to x integrals or derivatives of the set just mentioned. These are generated simply by rewriting equation (30) as

$$\Phi=\sum_{n=0}^{\infty}[s^m C_{2n}(s)]\left[\frac{\cos 2n\theta K_{2n}(sr)}{s^m}\right] \quad (31)$$

The first term represents the axial strength function, and the second term represents the fundamental multipole solutions. For each value of the index m there is obtained a distinct set of multipole solutions. For selected values of m the multipoles have the following forms:

$$\left.\begin{aligned}
&m=0\\
&\cos 2n\theta L^{-1}[K_{2n}(sr)]=\frac{\cos 2n\theta\cosh(2n\cosh^{-1}x/r)}{\sqrt{x^2-r^2}}; && x>r\\
&\qquad=0; && x<r\\
&m=1\\
&\cos 2n\theta L^{-1}\left[\frac{K_{2n}(sr)}{s}\right]=\cos 2n\theta\frac{\sinh(2n\cosh^{-1}x/r)}{2n}; && x>r\\
&\qquad=0; && x<r\\
&m=2n\\
&\cos 2n\theta L^{-1}\left[\frac{K_{2n}(sr)}{s^{2n}}\right]=\cos 2n\theta\frac{(2n)!}{(4n)!}\left(\frac{2}{r}\right)^{2n}(x^2-r^2)^{2n-1/2}; && x>r\\
&\qquad=0; && x<r
\end{aligned}\right\} \quad (32)$$

For positive values of m it is clear that at the Mach cone ($x=r$) no nonintegrable singularities occur. For negative values of m, derivatives of the $m=0$ multipoles are encountered and the singularities occur on the Mach cone rather than on the axis. Since these singularities occur in the flow field, they are not well suited to numerical methods of analysis. Another set of simple multipoles with singularities on the Mach cone are those of reference 19 given by

$$\frac{r^{2n}\cos 2n\theta}{(x^2-r^2)^{2n+1/2}}$$

Multipole strengths.—The first step in determining the interference potential by the method of multipoles is to determine the multipole strength from the velocity amplitude functions. For the $m=0$ set of multipoles the relationship between these two quantities is already given by equation (16)

$$C_{2n}(s)=\frac{F_{2n}(s)}{sK_{2n}'(s)} \tag{33}$$

If the potential at a point P as shown in figure 7 is desired, the

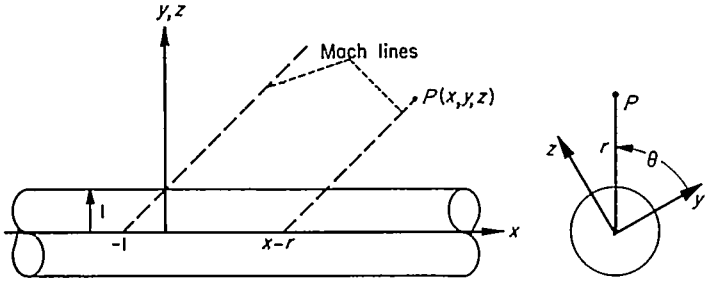

FIGURE 7.—General point at which potential is to be determined.

multipoles must be distributed from -1 to $x-r$ along the body axis. Since Laplace transforms must be zero for $x\leq 0$, the axial distribution must be shifted a distance at least unity to the right by introducing e^{-s} into the transform

$$e^{-s}C_{2n}(s)=\left[\frac{1}{e^{s}sK_{2n}'(s)}\right][F_{2n}(s)] \tag{34}$$

Equation (34) defines a Faltung integral involving a new set of characteristic functions given by

$$M_{2n}(x)\equiv L^{-1}\left[\frac{1}{e^{s}sK_{2n}'(s)}\right] \tag{35}$$

These characteristic functions have been studied in reference 7, are tabulated in table I, and are plotted in figure 8. Forming now the

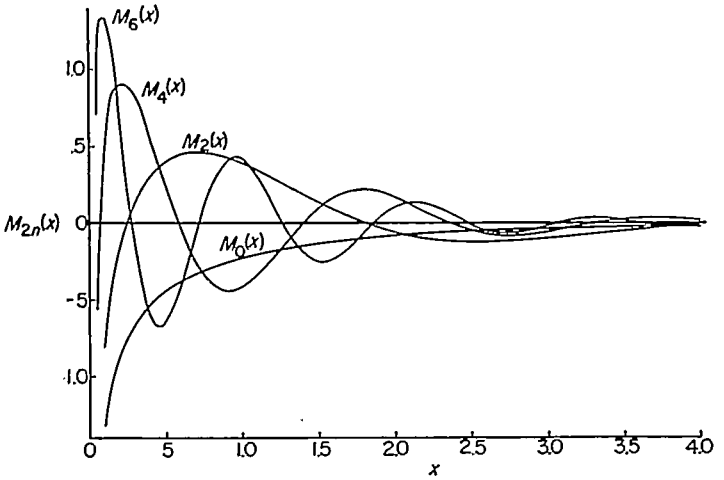

FIGURE 8.—Graphical representation of $M_{2n}(x)$ functions.

Faltung integral of equation (34) we obtain

$$c_{2n}(x-1)=\int_o^x f_{2n}(\xi)M_{2n}(x-\xi)\,d\xi \tag{36}$$

The function $M_{2n}(x)$ has a square-root singularity at the origin so that $c_{2n}(x-1)$ will be finite if $f_{2n}(x)$ is finite. However, $f_{2n}(x)$ may have a singularity which in confluence with the square-root singularity of $M_{2n}(x)$ produces a singularity in $c_{2n}(x-1)$.

Increasing the index m by unity has the effect of integrating the set of multipoles with respect to x and of differentiating the axial strength functions by x. While this decreases the order of the singularities of the multipole solutions, it increases the order of the singularities of the axial strength functions. The highest index m that does not lead to singularities thus depends on how many nonsingular derivatives $c_{2n}(x-1)$ possesses, which, in turn, depends on the smoothness of $f_{2n}(x)$. In the calculations for the wing-incidence case (ref. 7) $f_{2n}'(x)$ has a square-root singularity at $x=1$ so that $c_{2n}'(x-1)$ has a logarithmic singularity. Since $c_{2n}(x-1)$ corresponds to $m=0$, it was possible to use multipole solutions of the $m=1$ class and still obtain integrable singularities in the axial strength functions.

Properties of the $M_{2n}(x,r)$ functions.—The $M_{2n}(x,r)$ functions have simple physical significance. Let the velocity amplitude function be that corresponding to a delta function as shown in figure 6. Then by equation (36)

$$c_{2n}(x-1)=M_{2n}(x)$$

Thus the $M_{2n}(x)$ function represents the distribution along the axis of multipole strength for the $m=0$ set of multipoles necessary to make the velocity amplitude function a delta function. Correspondingly, it is the distribution necessary to produce a pressure field corresponding to the $W_{2n}(x-r+1,r)$ function. Equations (25) and (30) yield the relationship between the $W_{2n}(x,r)$ and $M_{2n}(x)$ functions.

$$W_{2n}(x-r+1,\,r)=\frac{\partial}{\partial x}\int_{r-1}^{x}M_{2n}(x-\xi)\frac{\cosh\left(2n\cosh^{-1}\dfrac{\xi+1}{r}\right)}{\sqrt{(\xi+1)^2-r^2}}\,d\xi$$

$$x>r-1 \tag{37}$$

Series for the $M_{2n}(x)$ functions for small and large values of the argument have been obtained by the standard methods of Laplace transform theory in reference 7

$$M_{2n}(x)\approx-\frac{\sqrt{2}}{\pi}\left[\frac{1}{\sqrt{x}}-\frac{(16n^2+3)}{4}\sqrt{x}+\frac{256n^4-32n^2+33}{96}x^{3/2}+\ldots\right] \tag{38}$$

The square-root singularity of $M_{2n}(x)$ at the origin is noteworthy. For the asymptotic result only a single term has been calculated

$$M_o(x)\sim-\frac{1}{x^3} \tag{39}$$

$$M_{2n}(x)\sim\frac{-16n(6n)!}{(2n!)^3 2^{6n+1}}\left(\frac{1}{x}\right)^{6n+1} \tag{40}$$

Span loading and pressure coefficient.—From equation (31) the potential can be written

$$\Phi=\sum_{n=0}^{\infty}\cos 2n\theta\,[e^{-s}C_{2n}(s)]\,[K_{2n}(sr)e^{s}] \tag{41}$$

so that

$$\varphi=\sum_{n=0}^{\infty}\cos 2n\theta\int_{r-1}^{x}\frac{c_{2n}(x-1-\xi)\cosh\left(2n\cosh^{-1}\frac{\xi+1}{r}\right)}{\sqrt{(\xi+1)^2-r^2}}\,d\xi \tag{42}$$

From this result the potential can readily be obtained and hence the span loading. The pressure coefficient follows directly from equation (42) using the linearized form of Bernoulli's equation

$$P=-\frac{2}{V}\varphi_x \tag{43}$$

Thus

$$P=-\frac{2}{V}\sum_{n=0}^{\infty}\cos 2n\theta\left\{\frac{c_{2n}(-1)\cosh\left(2n\cosh^{-1}\frac{x+1}{r}\right)}{\sqrt{(x+1)^2-r^2}}+\int_{r-1}^{x}\frac{\partial}{\partial x}\frac{c_{2n}(x-1-\xi)\cosh\left(2n\cosh^{-1}\frac{\xi+1}{r}\right)}{\sqrt{(\xi+1)^2-r^2}}\,d\xi\right\} \tag{44}$$

The practicability of using this result for calculating the pressures depends in the first place on the accuracy with which $\frac{\partial}{\partial x}c_{2n}(x-1-\xi)$ can be calculated. Since this calculation depends on the $M_{2n}(x)$ functions, which are tabulated at the present time only to the third decimal place, only three significant figures will usually be obtained for the axial strength functions. For higher harmonics and large values of x, loss of accuracy is incurred through the nature of the multipole solutions themselves. The following tabulation illustrates the point.

$\cosh(2n\cosh^{-1}x)$

x \ n	0	1	2	3
1	1	1	1	1
2	1	7	97	1, 350
3	1	17	580	19, 600
4	1	31	1920	119, 000

Although the set of multipoles used here is not well adapted to the calculation of pressure coefficient for high harmonics and large values of x, it nevertheless is useful for calculating span loadings since only one or two harmonics are needed in this case. The difficulties of computing pressure coefficient are alleviated in part by the fact that the pressure disturbances due to higher harmonics damp out within a few downstream radii. In reference 7 the pressure coefficients were computed up to the fourth harmonic ($n=3$) but with some difficulty. The use of a set of multipole solutions other than the $m=0$ set does not hold much promise since increasing the value of m introduces singularities into the axial strength functions and decreasing the value of m introduces singularities into the multipole solutions. While these singularities are tractable using the methods of analysis, they are not adapted to the numerical methods used herein. The method utilizing the $W_{2n}(x,r)$ function avoids difficulties with large numbers and with singularities.

II. APPLICATION OF THEORY TO COMBINATION OF CIRCULAR BODY AND RECTANGULAR WING

In this part of the report calculations are carried out to determine the pressure field acting on a wing-body combination employing a rectangular wing with no thickness. The calculations are first made for the body at zero angle of attack with the wing at incidence—the wing-incidence case. The calculations are then made for the body at angle of attack with the wing at zero angle of incidence—the angle-of-attack case. For the calculations attention is focused on the upper half of the combination since the experimental measurements were made for the upper half.

WING-INCIDENCE CASE

The complete pressure field will now be calculated. As previously mentioned, the wing alone can be specified in any convenient manner and, for the purpose of the example, the wing alone is taken as the rectangular wing extending straight through the body from side to side. Although the analysis as carried out is for $M=\sqrt{2}$, the results are presented in a form applicable to a range of Mach numbers. The steps in performing the calculation are: (1) to determine φ_W, the wing-alone potential; (2) to determine the velocity amplitude functions, $f_{2n}(x)$; and (3) to determine the potential or pressure, as desired, anywhere in the field. No tip effects are considered until the results are presented as a function of wing aspect ratio.

Wing-alone potential.—The wing-alone flow, exclusive of tip effects, can be determined from the Ackeret theory. The flow at a spanwise station out of the region of influence of the wing tips is illustrated in figure 9. The potential for the flow above the wing is

$$\varphi_W=Vx \text{ when } z\geq x \tag{45}$$

$$\varphi_W=Vx+i_W V(x-z) \text{ when } z\leq x \tag{46}$$

The sidewash produced by such a potential $\frac{\partial\varphi_W}{\partial y}$ is zero, and

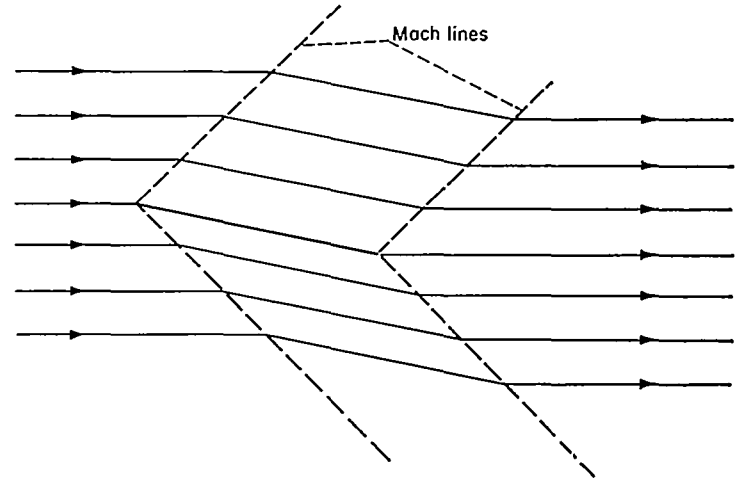

FIGURE 9.—Flow field produced by wing alone.

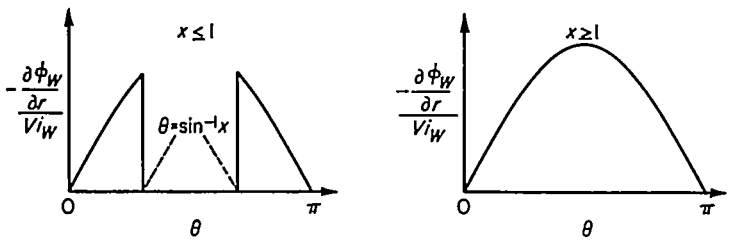

FIGURE 10.—Variation of normal velocity induced at body surface by wing alone; unit body radius; wing-incidence case.

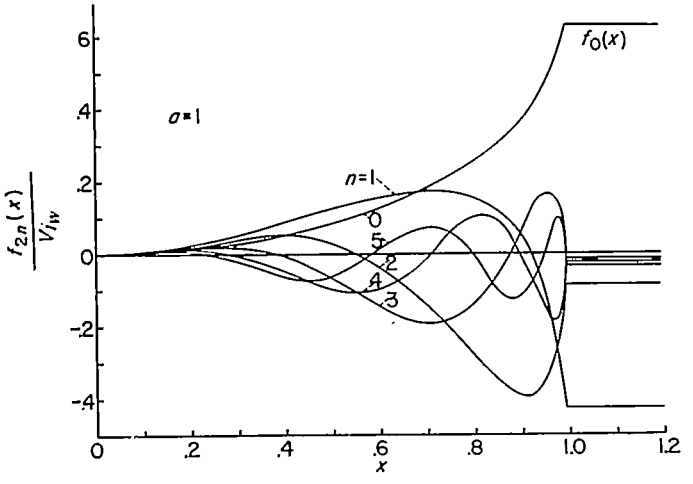

FIGURE 11.—Graphical representation of velocity amplitude functions; wing-incidence case.

the downwash $\frac{\partial \varphi_W}{\partial z}$ is uniformly $-i_W V$. The downwash causes a flow normal to the surface $r=1$ in amount $-i_W V \sin \theta$. This means that, for a body conforming to the wing-along flow, the deformation is zero at the wing-body junctures and a maximum on the top of the body. The interference combinations when added to the deformed body straighten it out Fourier component by Fourier component.

Fourier amplitudes of body normal velocity.—The Fourier amplitudes of the normal velocity induced by the wing-alone potential at the body are determined by expanding $\frac{\partial \varphi_W}{\partial r}$ at $r=1$ in a Fourier cosine series of even multiples of θ. The normal velocity distribution is shown in figure 10. For $x \geq 1$ the body is totally immersed in the wing downwash field. With the usual equation for obtaining the Fourier amplitudes of a function, there is obtained

$$f_0(x) = \frac{2}{\pi} \int_0^{\sin^{-1} x} i_W V \sin \theta \, d\theta \tag{47}$$

$$f_{2n}(x) = \frac{4}{\pi} \int_0^{\sin^{-1} x} i_W V \sin \theta \cos 2n\theta \, d\theta \tag{48}$$

The integrations give

$$f_0(x) = \frac{2 V i_W}{\pi} (1 - \sqrt{1-x^2}) \text{ when } x \leq 1 \tag{49}$$

$$f_0(x) = \frac{2 V i_W}{\pi} \text{ when } x \geq 1 \tag{50}$$

$$f_{2n}(x) = \frac{V i_W}{\pi} \left[\frac{2 \cos (2n-1)\omega}{2n-1} - \frac{2 \cos (2n+1)\omega}{2n+1} - \frac{4}{4n^2-1} \right] \text{ when } x \leq 1 \tag{51}$$

$$f_{2n}(x) = \frac{-4 V i_W}{\pi (4n^2-1)} \text{ when } x \geq 1 \tag{52}$$

where $\omega = \sin^{-1} x$. The $f_{2n}(x)$ functions are shown in figure 11. The constant values of $f_{2n}(x)$ for $x \geq 1$ are noteworthy. The values of $f_{2n}(x)$ are tabulated in table II.

Interference pressure distributions.—The interference pressure distributions have been calculated for the first four Fourier components and are presented in figure 12. In this figure the abscissa is proportional to distance behind the Mach line originating at the leading edge of the juncture, as illustrated in part (a) of the figure. Although the calculations have been carried out for $M=\sqrt{2}$, that is, $\beta=1$, and for unit radius, they are generalized to all Mach numbers and body radii by replacing $x-r+1$ by $\frac{x}{\beta a} - \frac{r}{a} + 1$ and P_{2n} by βP_{2n} as has been done in the figure. From the figure it is apparent that the cusps in the pressure distributions are propagated downstream along lines of constant $\frac{x}{\beta a} - \frac{r}{a} + 1$ or $x - \beta r$; that is, along the downstream characteristics. As the pressure distributions move outward from the body along the downstream characteristics, they are distorted and decreased in magnitude.

Increasing the order of the Fourier harmonics causes two important effects: first, the number of points of zero pressure is increased and, second, the pressure coefficient damps more rapidly. As a result of the first effect, the contributions of the higher harmonics to the combination span loading are proportionally less than their contributions to the pressure coefficient; while, as a result of the second effect, the more remote a point is from the leading edge of the wing-body juncture, the fewer the number of Fourier components that must be included to obtain its pressure coefficient accurately. All interference pressure distributions exhibit discontinuities in slope at $\frac{x}{\beta a} - \frac{r}{a} + 1 = 1$. This behavior is a consequence of the fact that the body becomes totally immersed in the wing-alone flow field for this condition. When the pressure distributions of the various Fourier components are added together to obtain the interference pressure distributions, the discontinuities in slope tend to cancel so that the pressure distribution for the combination will be smooth.

A detailed examination of the interference pressure distribution for the first Fourier component illustrates several points of interest. The importance of the component arises from the fact that it accounts for most of the effect of interference on the span loading. The reason for this is that the pressure coefficients for $n=0$ are of invariable sign. The effect of the first Fourier component is to reduce the velocity induced normal to the body by the wing-alone flow field to zero averaged around the body from $\theta=0$ to $\theta=\pi$ at any streamwise location.

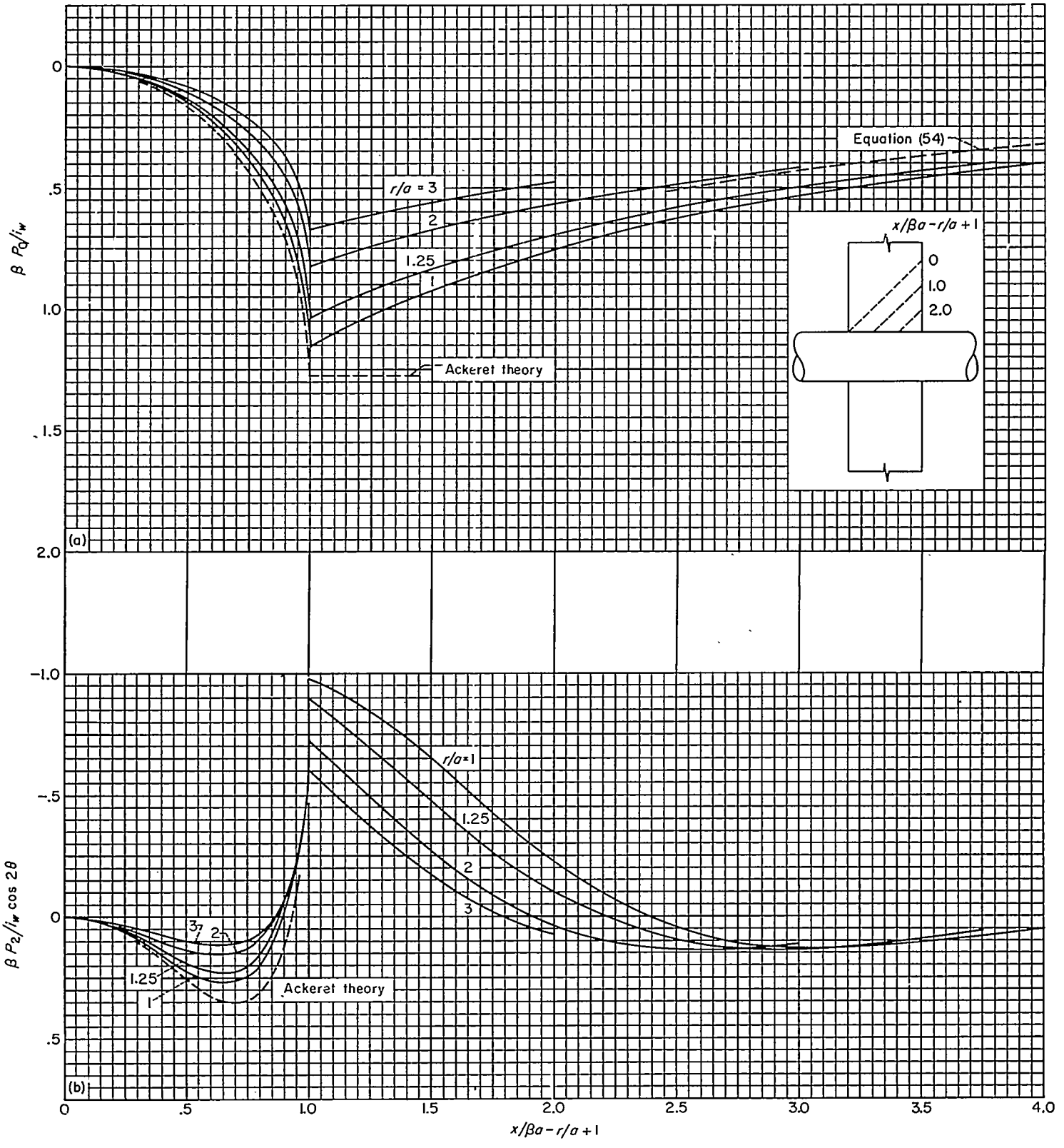

(a) $n=0$
(b) $n=1$

FIGURE 12.—Interference pressure distributions of various Fourier components; wing-incidence case.

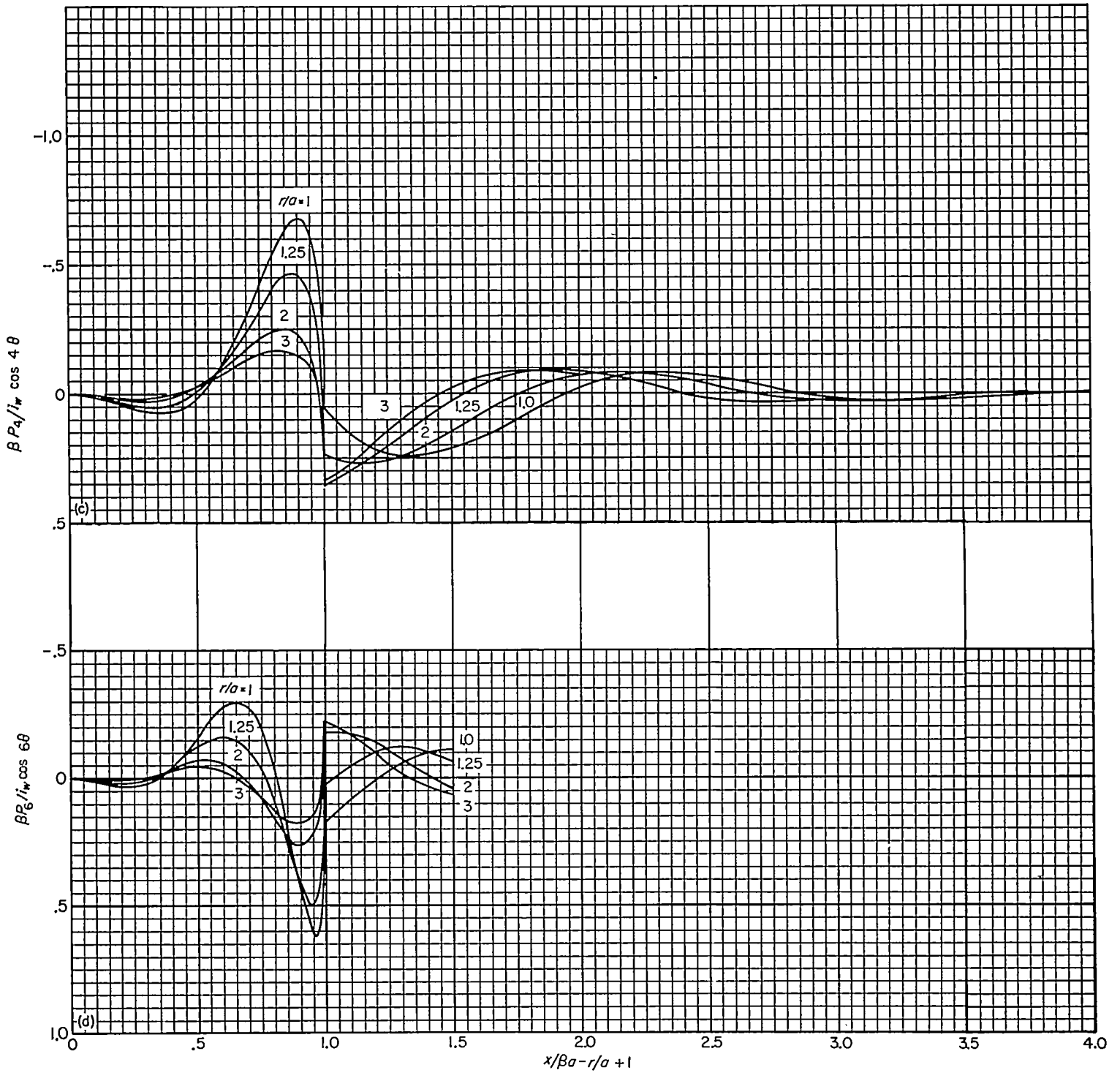

(c) $n=2$
(d) $n=3$

FIGURE 12.—Concluded.

For purposes of comparison with the exact results for $n=0$, some approximate results have been included in figure 12 (a). For values of $\frac{x}{\beta a}<1$ on the body, the Ackeret value of P_o (twice the local stream angle divided by β) is a close approximation to the true pressure coefficient. This is the result of the facts that the part of the body affecting the interference is effectively plane for points near the leading edge of the wing-body juncture and that there is no variation of any quantities with θ so that an approximate two-dimensional situation prevails. As $\frac{x}{\beta a}$ increases beyond unity on the body, there is a rapid decrease in the pressure coefficient below the Ackeret value due to the effect of all disturbances in front of the point in question as represented by the integral of equation (24).

In reference 7, the following approximate results were obtained for small and large values of $\frac{x}{\beta a}-\frac{r}{a}+1$ for the pressure coefficient:

$$\left.\begin{aligned}\beta P_o &\rightarrow \frac{2i_W}{\pi\sqrt{r}}\left(\frac{x}{\beta a}-\frac{r}{a}+1\right)^2 \\ \beta P_{2n} &\rightarrow \frac{4i_W}{\pi\sqrt{r}}\left(\frac{x}{\beta a}-\frac{r}{a}+1\right)^2 \cos 2n\theta\end{aligned}\right\} \quad (53)$$

as $\frac{x}{\beta a}-\frac{r}{a}+1\rightarrow 0$

$$\left.\begin{aligned}\beta P_o &\rightarrow \frac{4i_W}{\pi}\left(\frac{x}{\beta a}\right)^{-1} \\ \beta P_{2n} &\rightarrow -\frac{32i_W(4n!)(r^{2n}+r^{-2n})\cos 2n\theta}{\pi(2n!)^2(4n^2-1)2^{4n+1}}\left(\frac{x}{\beta a}\right)^{-(4n+1)}\end{aligned}\right\} \quad (54)$$

as $\frac{x}{\beta a}\rightarrow\infty$

For $\frac{x}{\beta a}-\frac{r}{a}+1\leq 0.6$ equation (53) is a good approximation for $n=0$ although it is of little value for higher-order harmonics. There is a general tendency of P_o to approach a uniform value independent of r as $\frac{x}{\beta a}-\frac{r}{a}+1$ becomes large, as shown by equation (54). The damping in the characteristic direction, although initially inversely proportional to the square root of r, is ultimately independent of r.

Pressure distribution in juncture of wing-body combination.—By adding the interference pressure coefficients of the various Fourier components to that for the wing alone, the pressure distribution for the combination is obtained. The addition has been carried out for the wing-body juncture using four Fourier components and six Fourier components, and the results are presented in figure 13. The pressure coefficient with interference is less in magnitude than 2, the value without interference, showing that significant losses of lift occur in the wing-body juncture. A comparison of the results for four components and six components shows that four components give good over-all accuracy for all values of $\frac{x}{\beta a}$ greater than 1. For small values of $\frac{x}{\beta a}$ in the wing-body juncture, the curvature of the body insofar as the flow is concerned is not large so that the body is effectively a vertical boundary on which a given distribution of normal velocity is producing an interference field. Supersonic wing theory applied to this condition gives for the net interference pressure coefficient (ref. 7).

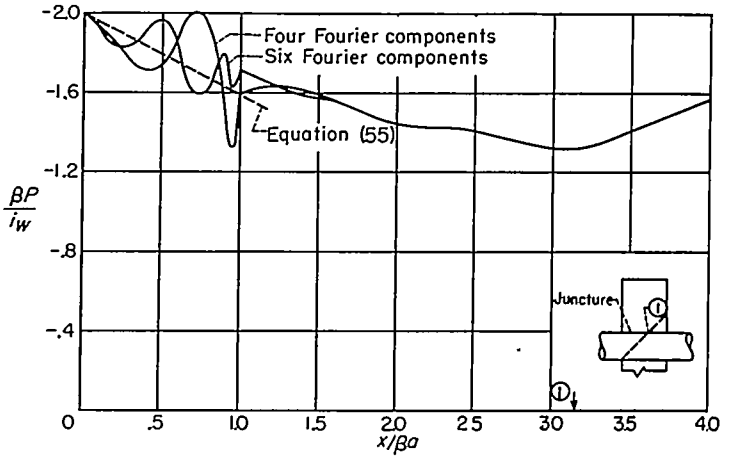

FIGURE 13.—Theoretical pressure distribution at wing-body juncture of combination using four and six Fourier components; wing-incidence case.

$$\frac{\beta P}{i_W}\rightarrow\frac{4x}{3\pi\beta a} \text{ when } \frac{x}{\beta a}\rightarrow 0 \quad (55)$$

It is clear that the calculated results can be jointed smoothly to this result. Using the result of equation (55) enables satisfactory results to be obtained with four Fourier components.

The critical region in the convergence of the solution is that near the leading edge of the wing-body juncture. The higher harmonics have their most important effect near here and rapidly damp downstream along the body. Hence more and more Fourier components would be required to get accuracy for smaller and smaller values of $\frac{x}{\beta a}$. However, with the result of equation (55), this extra work is unnecessary.

One point of interest in figure 13 is the fact that when $\frac{x}{\beta a}$ equals approximately 3, the pressure coefficient increases in magnitude. This is due to the fact that for $\frac{x}{\beta a}\geq\pi$ the influence of the opposite half-wing is felt in the wing-body juncture.

Pressure distribution on top meridian of wing-body combination.—The pressure distribution on the top meridian of the wing-body combination is obtained in the same fashion as that at the wing-body juncture, the difference being that the pressures due to the even number Fourier components have the same sign at the meridian as at the juncture, whereas the odd numbered components have reversed signs. The pressure distributions based on four and six Fourier components are shown in figure 14.

Several interesting effects are exhibited by the results. The step in the wing-alone pressure at $\frac{x}{\beta a}=1$ is effectively canceled by the interference pressures of the Fourier com-

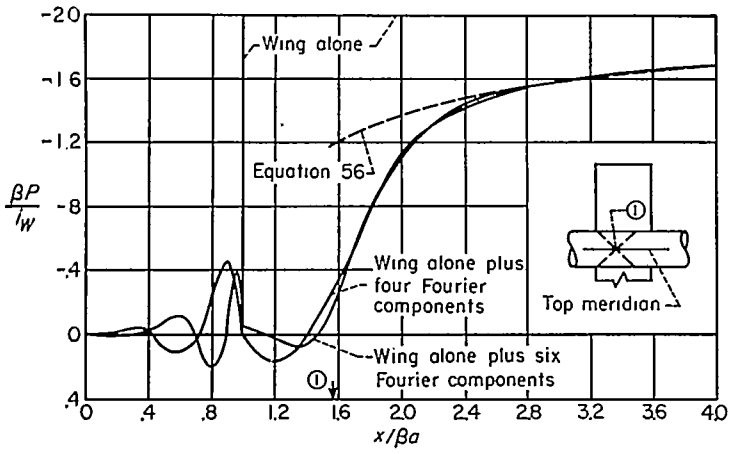

FIGURE 14.—Theoretical pressure distribution on top of combination using four and six Fourier components; wing-incidence case.

ponents from $\frac{x}{\beta a}=1$ to $\frac{x}{\beta a}=\pi/2$, and for $\frac{x}{\beta a}>\pi/2$ the pressure increases rapidly and tends toward the two-dimensional value. The effect of the interference pressure in canceling the effect of the wing alone on the top of the body from $\frac{x}{\beta a}=1$ to $\frac{x}{\beta a}=\pi/2$ is to be expected since the wing of the combination can have no effect on the top of the body unless $\frac{x}{\beta a}\geq\pi/2$, as has been already pointed out. If an infinite number of Fourier components had been taken, the pressure coefficients would be identically zero from $\frac{x}{\beta a}=0$ to $\frac{x}{\beta a}=\pi/2$. The general behavior in this regard is evidence of the plausibility of the calculated results.

The tendency of the pressures to approach an asymptotic value is also illustrated by figure 14. This asymptotic value represented by the sum of the wing-alone pressure plus the asymptotic results for the first Fourier component is given by the following equation:

$$\frac{\beta P}{i_W}\sim -2+\frac{4}{\pi x/\beta a} \tag{56}$$

For $\frac{x}{\beta a}>2.4$, the results of this equation are in good agreement with the results of figure 14.

Some evidence is furnished from the pressure calculations for the juncture and top of the body concerning the number of Fourier components necessary for accuracy. Comparisons made in figures 13 and 14 show that about four components are sufficient and that the addition of two more is not worth the extra work.

Pressure distribution on wing of wing-body combination.—The distribution of the pressure acting on the wing of the combination can be determined in a manner similar to that for the wing-body juncture by adding to the wing-alone pressure those due to the Fourier components. The resultant pressure distribution for the wing based on four Fourier components is shown in figure 15. For small values of $\frac{x}{\beta a}$ the higher-order oscillations in the pressure coefficient as shown in figure 13 have been ignored, and the curves have been faired through them.

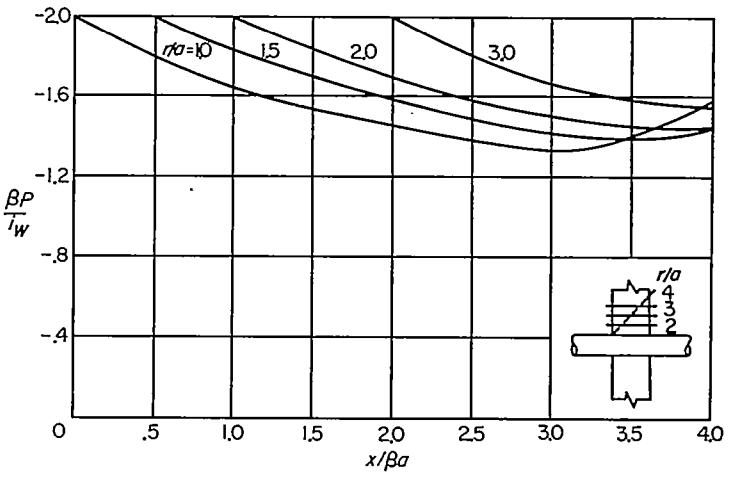

FIGURE 15.—Theoretical pressure distribution acting on wing of combination; wing-incidence case.

Since the region of influence of the body on the wing is confined to the wing region downstream of the Mach lines emanating from the leading edge of the juncture, in front of this line the pressures are uniform at the two-dimensional value, and behind the line there is a decrease in the magnitude of the pressure coefficient. If the body were a perfect reflector, that is, a vertical wall of infinite extent, then there would be no pressure loss. However, the pressure pulses originating on the wing are only in part reflected by the circular body. The efficiency of the body as a reflector is discussed subsequently in connection with span loading. The tendency of the pressure to increase in magnitude near the inboard trailing edge is due to the effect of the opposite wing panel which at the wing juncture is felt downstream of the point $\frac{x}{\beta a}=\pi$.

Span loading.—The span load distributions for a range of rectangular wing-body combinations with the body at zero angle of attack can be determined from the pressure distributions of figures 13, 14, and 15. Since the pressure distributions of figure 15 are in a form independent of Mach number, it is convenient to define a span loading which is an integral of these distributions.

$$\begin{aligned}\frac{L}{q\alpha_W a^2}&=\int_{-s/a}^{s/a}\left[\int_0^{c/\beta a}\left(\frac{\beta P_L}{i_W}-\frac{\beta P_U}{i_W}\right)d\left(\frac{x}{\beta a}\right)\right]d\left(\frac{y}{a}\right)\\&=\frac{1}{a}\int_{-s}^{+s}\left[\frac{1}{a}\int_0^c\left(\frac{P_L}{i_W}-\frac{P_U}{i_W}\right)dx\right]dy\\&=\frac{1}{a}\int_{-s}^{+s}\left[\frac{1}{a}\int_0^c\left(\frac{-2P}{i_W}\right)dx\right]dy\end{aligned} \tag{57}$$

The quantity in the square brackets is taken to be the span loading. If all distances are taken in units of the body radius, then "a" can be set equal to unity in the formulas.

The pressure results of figure 15 are for values of the effective chord-radius ratio of 4 or less and for values of the effective aspect ratio of 2 or greater. Span loadings for any combination of $\frac{c}{\beta a}$ (or c^*) and βA in these ranges can be obtained by integrating the pressure distributions. The span loading evaluations have been made for $c^*=4$ and $\beta A\geq 2$. First the span loadings due to the various Fourier

components are discussed, and then the span loadings for the actual wing-body combinations are presented.

In figure 16, the contributions to the span loading for the first three Fourier components are shown. For $n=0$ the pressure field does not depend on θ, being axially symmetric, and a constant loading exists on the body. However, on the wing as the spanwise distance increases there is a decrease in the span loading, due primarily to decrease in the length of chord over which the interference pressures act. The span loading due to the first Fourier component causes a loss of lift everywhere along the span.

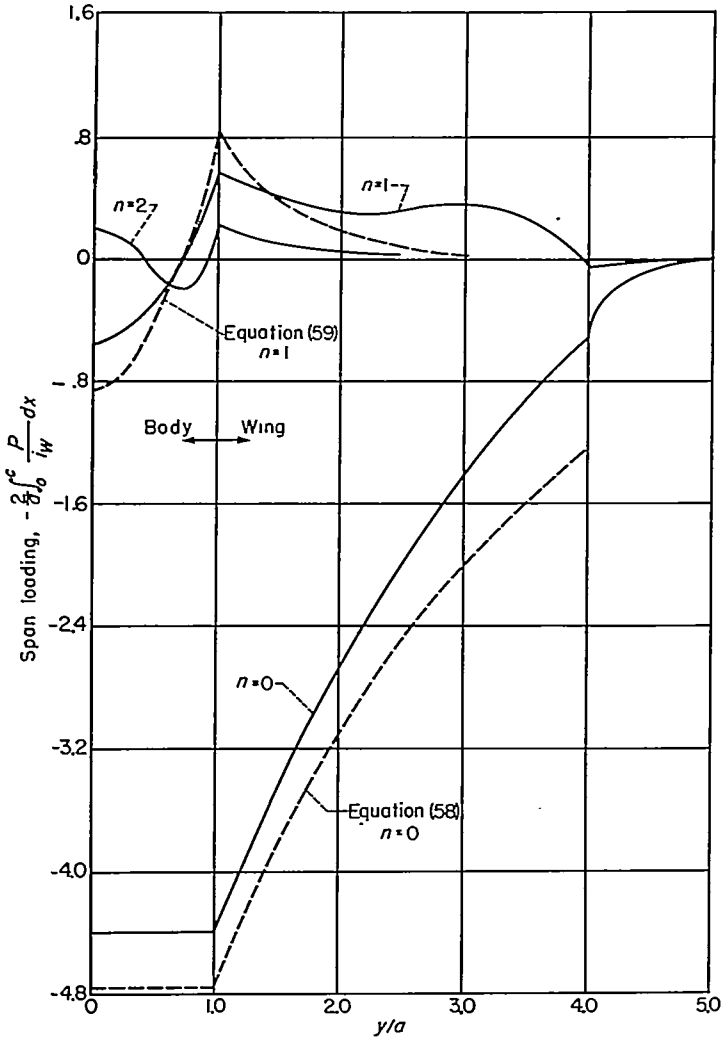

FIGURE 16.—Theoretical span loading of various Fourier components acting on combination of body and rectangular wing having effective chord-radius ratio of 4; wing-incidence case.

A comparison of the results of figure 16 for $n=0$ and $n=1$ shows that the first Fourier component accounts almost entirely for the effect of interference on the span loading of the combination. For the body this fact is even more true than for the wing. This fact is of considerable importance since it gives a simple means of extending the lift and moment results to larger values of $\frac{c}{\beta a}$ than those for which the pressure distributions have been calculated. Also, it suggests a simple means of minimizing the adverse effects of interference on lift as will subsequently be pointed out.

With the techniques of Laplace transform theory, it is possible to obtain asymptotic formulas for the span loadings of the various Fourier components. For the first Fourier component the following asymptotic result has been obtained by the standard methods of Laplace transform theory. (See Appendix B.)

$$-2\int_0^{\frac{x}{\beta a}}\left(\frac{\beta P_o}{i_W}\right)d\left(\frac{x}{\beta a}\right)=\frac{-2}{a}\int_0^x\frac{P_o}{i_W}dx\rightarrow\frac{8}{\pi}\log\left(\frac{r/2a}{x/\beta a}\right)+\frac{2}{x/\beta a}$$

$$\text{when } \frac{x}{\beta a}\rightarrow\infty \tag{58}$$

The asymptotic result for the span loading given by this equation, when compared with the results of the exact calculations in figure 16, is seen to be slightly low. However, for values of $\frac{c}{\beta a}$ greater than 4 the difference between the results decreases, and equation (58) thus provides a satisfactory means of extrapolating the results of the present calculations for span loading to larger values of $\frac{c}{\beta a}$.

The asymptotic result has also been determined for the higher-order Fourier components as a matter of interest. The span loading is

$$-2\int_0^{\frac{x}{\beta a}}\left(\frac{\beta P_{2n}}{i_W}\right)d\left(\frac{x}{\beta a}\right)=\frac{-2}{a}\int_0^x\frac{P_{2n}}{i_W}dx\rightarrow\frac{8\cos 2n\theta}{\pi n(4n^2-1)r^{2n}}-\frac{16\left(r^{2n}+\frac{1}{r^{2n}}\right)(4n-1)!\cos 2n\theta}{\pi(2n!)^2(4n^2-1)2^{4n-1}\left(\frac{x}{\beta a}\right)^{4n}}\text{ as }\frac{x}{\beta a}\rightarrow\infty \tag{59}$$

The results of equation (59) and the exact solution for $n=1$ in figure 16 both corroborate the fact that the span loadings of all but the first Fourier component are negligible for $\frac{c}{\beta a}>4$. It is also to be noted that the contribution to the loading of the first component given by equation (58) increases without limit as $x\rightarrow\infty$; whereas the span loadings of the higher-order components are finite.

To obtain the span loading for the family of combinations for which $\frac{c}{\beta a}=4$, it is necessary to consider the loadings of both the wing alone and the Fourier components. The necessary calculations have been carried out, and the span loadings for the family of combinations based on one and four Fourier components are both shown in figure 17. The loading due to the wing alone is also shown. No effect of wing tips has been included. It is to be noted in figure 17 that, whereas the loading on the wing due to its own pressure field is constant, there is some loss on the body because of the fact that the pressure field of the wing alone acts on the body only if $x\geq\beta a\sin\theta$. However, if an afterbody is included, some of the lift lost can be recovered. As has already been pointed out, the pressures due to the first Fourier components are positive on the upper half of the wing-body combination and produce a loss of lift, as figure 17 shows. When the effects of four Fourier components are taken into account, the net lift is slightly higher than that for one Fourier component, but the difference is not signifi-

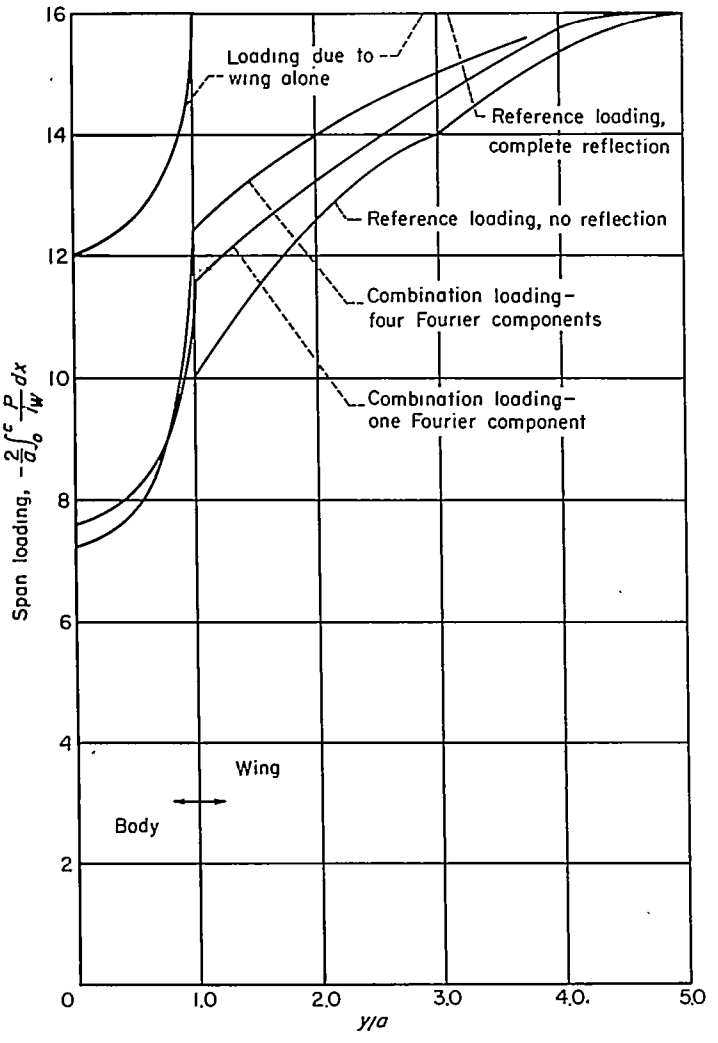

FIGURE 17.—Theoretical span loading for combination of body and rectangular wing having effective chord-radius ratio of 4; wing-incidence case.

cant. For most engineering purposes, one Fourier component is sufficient for determining the span loading when $\frac{c}{\beta a} \geq 4$.

Some insight into the mechanism of wing-body interference can be gained by comparing the span loading for the combination with those for two reference loadings: (1) the complete reflection case for which the blanketed area of the wing acts effectively at i_W, and (2) the no-reflection case for which the blanketed area of the wing is supposed to act effectively at zero angle of attack. The span loading corresponding to the first case of complete reflection of the wing pressure pulses by the body is, in fact, the span loading marked "wing alone" in figure 17. A comparison of this curve with that based on one or four Fourier components shows that the loading given on the assumption that the wing blanketed area is fully effective in lift is too optimistic. Under the conditions of the second reference loading, the sole purpose of the blanketed area is to support lift generated by the wings. A comparison of the span loading for this case with the true loading shows that the average load on the body is well predicted, but that the loading on the wing is underestimated. A comparison of the true loading with those for the two reference cases reveals the interesting fact that the body is somewhat less than 50 percent effective in reflection for this particular family of configurations.

Lift.—For values of $\frac{c}{\beta a} \leq 4$ the pressure distributions already presented are sufficient for obtaining span loading or lift on either the wing or body for all combinations having sufficiently large aspect ratios to avoid effects of the tips on the wing-body interference. This is the case for $\beta A \geq 2$. The lift results are presented in terms of a nondimensional parameter k_W, defined as the ratio of the lift on the exposed half-wings in combination (exclusive of that on the body) to that on the exposed half-wings joined together.

$$k_W = \frac{L_{Wc}}{L_W}, \quad \alpha_B = 0 \tag{60}$$

For $\frac{c}{\beta a} > 4$ the value of k_W can be obtained by using the asymptotic form of the span loading given by equation (58).

$$k_W = 1 - \frac{8\left[c^* + c^* \log\left(\frac{2c^*}{c^*+1}\right) - \frac{\pi}{4} - \log(c^*+1)\right]}{\pi c^{*2}(2\beta A - 1)}$$

$$c^* \to \infty \tag{61}$$

The values of k_W have been determined from the pressure distributions of figure 15 for values of $\frac{c}{\beta a} \leq 4$ and from equation (61) for values [4] of $\frac{c}{\beta a} > 4$. The effect of the wing tips has been taken into account by utilizing reference 20. The results are shown in figure 18 wherein k_W is given as a function

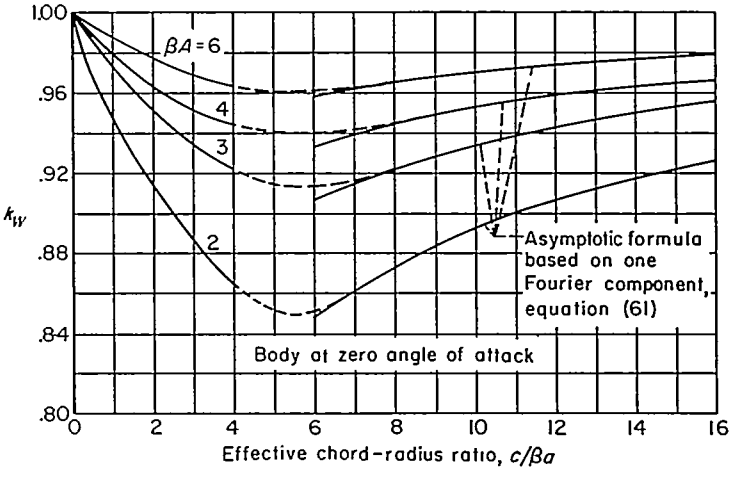

FIGURE 18.—Lift effectiveness for wing or control surface in combination with body.

of $\frac{c}{\beta a}$ for various effective aspect ratios of 2 and greater. It should be borne in mind that the results of the figure are for a combination of body and rectangular wing or an all-movable, rectangular control surface with no gap. It is noted in the figure that the exact results for $\frac{c}{\beta a} \leq 4$ can be faired into the

[4] In reference 10 the asymptotic analytical expressions for k_W and x_{cp}/c are not precise by virtue of an incorrect upper limit on an integral. The maximum numerical error in k_W is about 0.01 and in x_{cp}/c about 0.03 for very large values of c^*. The precise values are given in this report. Those for $\beta A = 2$ are unchanged.

asymptotic results for $\frac{c}{\beta a}>4$, thereby providing a design chart for engineering purposes for the entire range of $\frac{c}{\beta a}$. The curves of figure 18 illustrate the decrease of k_W as $\frac{c}{\beta a}$ increases at constant effective aspect ratio, and the slow increase of k_W as the wing chord becomes very large. The loss of lift is most serious for $\beta A=2$, being about 15 percent in the worst case.

A practical point in connection with the loss of lift on the wing due to interference is that this loss occurs no matter what the body angle of attack, even though the calculations are made for $\alpha_B=0$. It occurs either in the case of a wing mounted on a body or in the case of a deflected all-movable control surface. For wings with swept leading edges for which all of the wing area lies in the region affected by the interference, even larger losses than occur with rectangular wings are to be anticipated. However, the loss of lift at the design condition can, at least in principle, be largely prevented by designing the fuselage so that it conforms to the first Fourier component in the wing-alone flow. This would involve contracting the fuselage above the horizontal plane of symmetry in a rotationally symmetric fashion and expanding a like amount beneath the horizontal plane of symmetry. Whether or not such a change would improve the lift-drag ratio can best be determined by experiment.

Center of pressure.—The center-of-pressure locations have been calculated for the same range as the lift results of figure 18. The center-of-pressure location in chord lengths behind the leading edge are presented in figure 19. For large values of c^*, an asymptotic result has been calculated for x_{cp}/c using the methods of Laplace transform theory and considering only one Fourier component.

$$\frac{x_{cp}}{c}=\frac{\frac{1}{2}-\frac{1}{3\beta A}-\frac{2}{\beta A c^{*3}}\left[\frac{2c^{*2}}{\pi}+\frac{c^*}{2}\log\left(\frac{2c^*}{c^*+1}\right)-\frac{1}{2}\log(c^*+1)\right]}{k_W\left(1-\frac{1}{2\beta A}\right)}$$

as $c^*\to\infty$ (62)

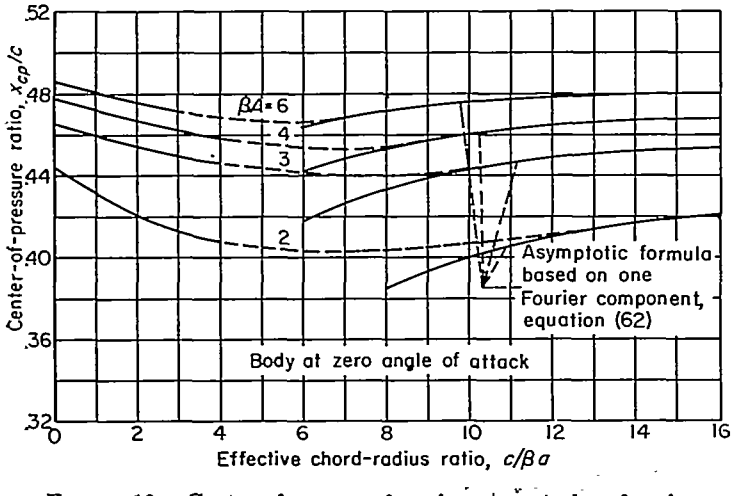

FIGURE 19.—Center of pressure for wing or control surface in combination with body.

The values of $\frac{x_{cp}}{c}$ have been determined from the pressure distributions of figure 15 for values of $\frac{c}{\beta a}\leq 4$ and by equation (62) for values of $\frac{c}{\beta a}>4$. The loss of lift near the tips has been taken into consideration. The exact results for $\frac{c}{\beta a}\leq 4$ have been faired into the asymptotic results for large values of $\frac{c}{\beta a}$ by dashed curves to provide an engineering design chart covering the entire range of $\frac{c}{\beta a}$. It is again mentioned that this chart is applicable both to the wing of an airplane or missile or to an all-movable, rectangular control surface with no gap. The curves of figure 19 start at values of $\frac{x_{cp}}{c}$ corresponding to those for the wing alone at $\frac{c}{\beta a}=0$. As $\frac{c}{\beta a}$ increases for constant βA, there is a forward movement of the center of pressure because of the loss of lift due to interference which is mostly effective on the rear of the wing. For the lowest effective aspect ratio of 2 there is about a 4-percent forward movement of the center of pressure due to interference in the extreme case. For large effective aspect ratios the forward movement is not nearly so large. As the value of $\frac{c}{\beta a}$ increases for constant βA, there is an asymptotic approach of the center of pressure back to the wing-alone value.

ANGLE-OF-ATTACK CASE

In figure 4 (a) it is shown how the flow field of a combination can be built up of a body alone and two wing-body flow fields. The first wing-body flow field ((2) of fig. 4 (a)) has been solved in the preceding section, and we now solve the second wing-body problem ((3) of fig. 4 (a)). The wing is effectively twisted so that the slope of its surface is α_u as given by equation (1). It should be noted that the problem of the combination and body with a rectangular wing twisted according to the second term of equation (1) has been solved by Bailey and Phinney in reference 11 using the present theory. Their calculation is restricted to the body

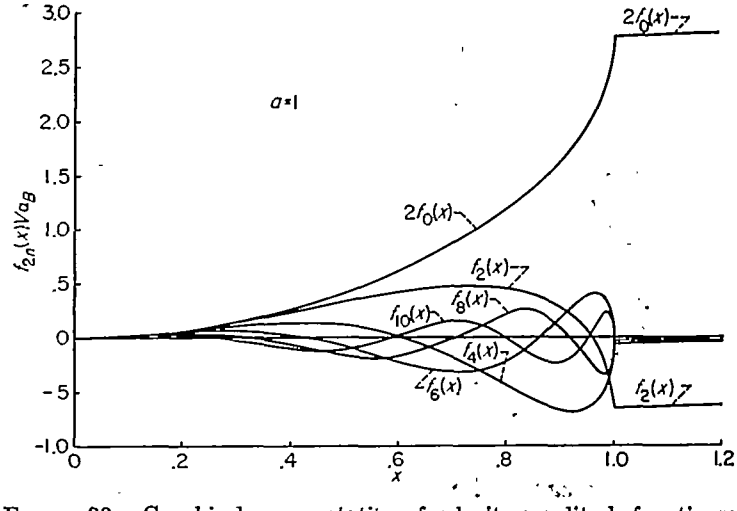

FIGURE 20.—Graphical representation of velocity amplitude functions; angle-of-attack case.

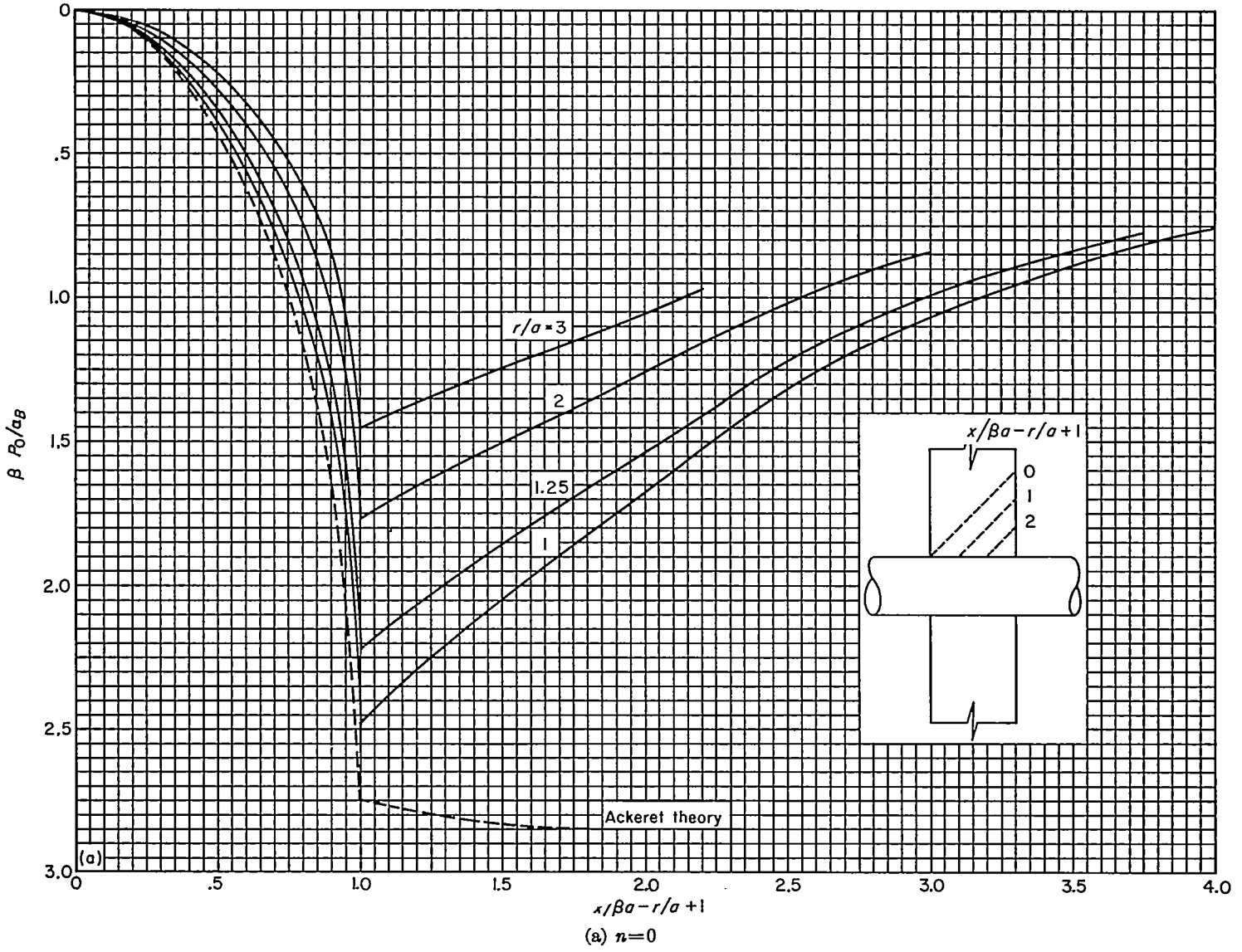

(a) $n=0$

FIGURE 21.—Interference pressure distributions of various Fourier components; angle-of-attack case.

and is carried out for downstream distances of $2\beta a$ from the wing leading edge. Actually, the results of reference 11 represent the difference between the angle-of-attack and wing-incidence cases treated here and are in agreement with the present results. This agreement is, in effect, an independent check on the accuracy of the present numerical results for the interference pressure distributions.

Wing-alone potential.—The first step in the calculation is to determine the wing-alone potential. Because the wing is twisted to conform to the body upwash field, this determination is fairly tedious and has been carried out in Appendix C. The form of the wing-alone potential found in reference 11 is in agreement with those found herein for the wing-incidence and angle-of-attack cases.

Fourier amplitudes of body normal velocity.—The velocity amplitude functions for the present case were computed numerically by performing a Fourier analysis of the calculated body normal velocity distribution at a number of body cross sections. An analytical determination was made of the velocity amplitude functions by the authors of reference 11 for values of $x<2$. However, for $x>2$ the velocity amplitude functions are said by these authors to lead to incomplete elliptic integrals, and no analytical determination was made. A numerical determination has been made herein for $0<x<4$. The numerical values of the $f_{2n}(x)$ functions for this case are tabulated in table II and plotted in figure 20 for illustrative purposes.

Interference pressure distributions.—The interference pressure distributions have been calculated by numerical integration using equation (22). The results are shown in figure 21. The interference pressure distributions are very similar to those for the wing-incidence case, being about twice as large.

Pressure distribution in juncture of wing-body combination.—The pressure distribution of the combination is obtained by adding the interference pressure coefficients to the pressure coefficients of the wing alone. The results, using four and six P_{2n} components, are shown in figure 22. This figure shows that four components give a close approximation to the linear-theory value for $x/\beta a>1$. At $x/\beta a=0$, the wing leading edge, linear theory with Beskin upwash theory gives exactly $\beta P/\alpha=-4.0$. For the region $x/\beta a<1$ the higher harmonics have their greatest importance, and many components would be necessary to get good accuracy.

413672—57——83

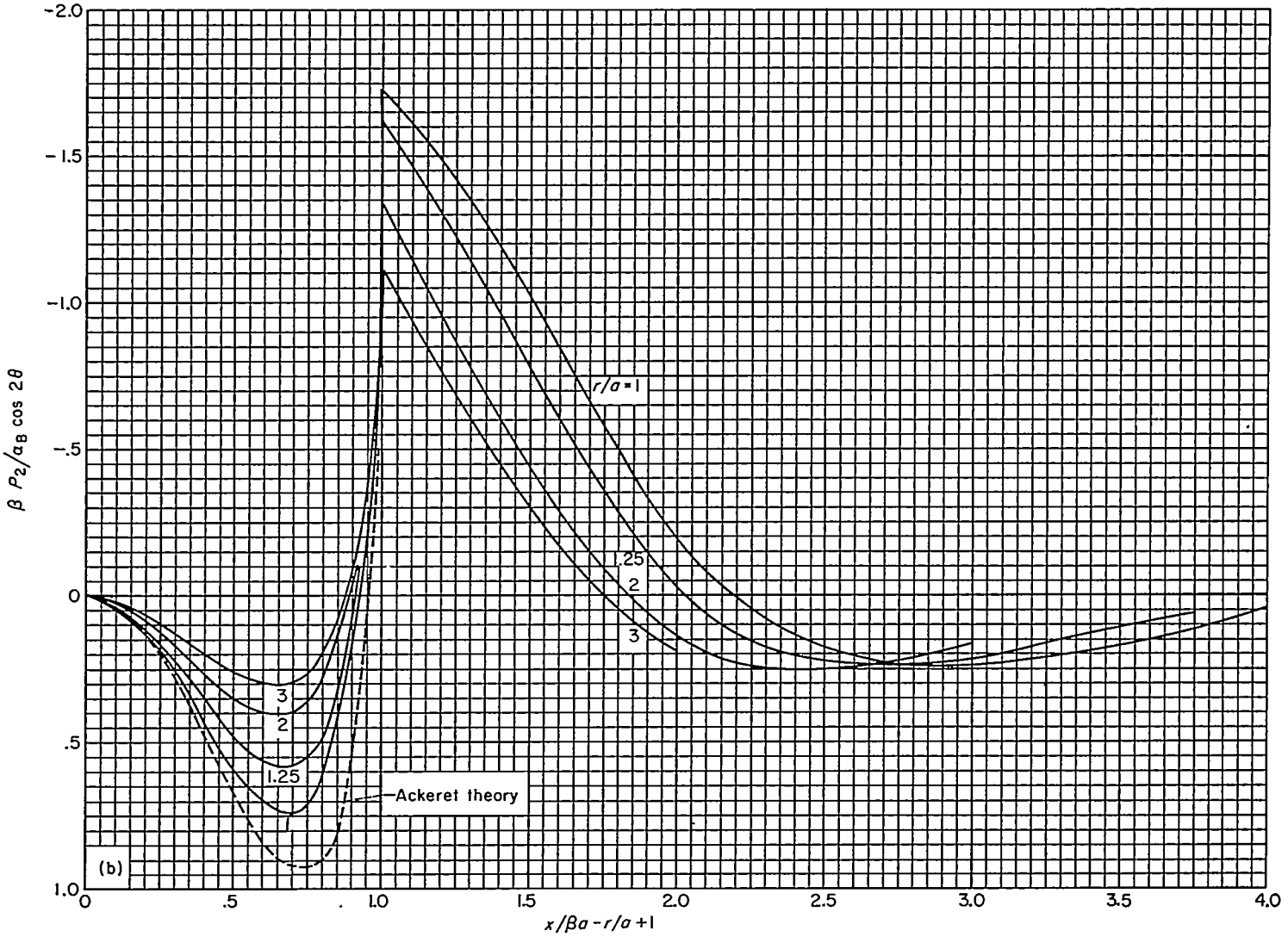

(b) $n=1$

FIGURE 21.—Continued.

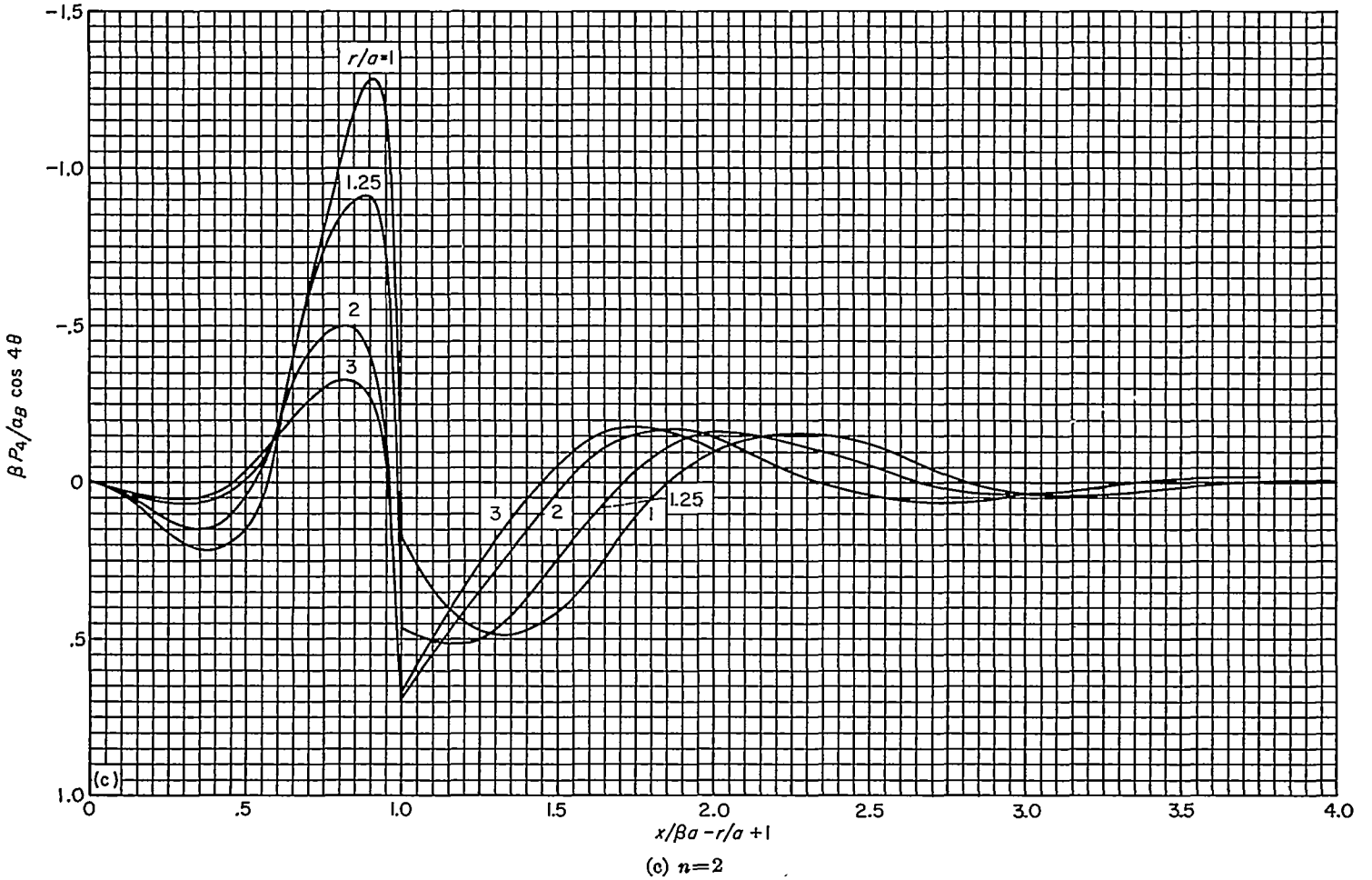

(c) $n=2$

FIGURE 21.—Continued.

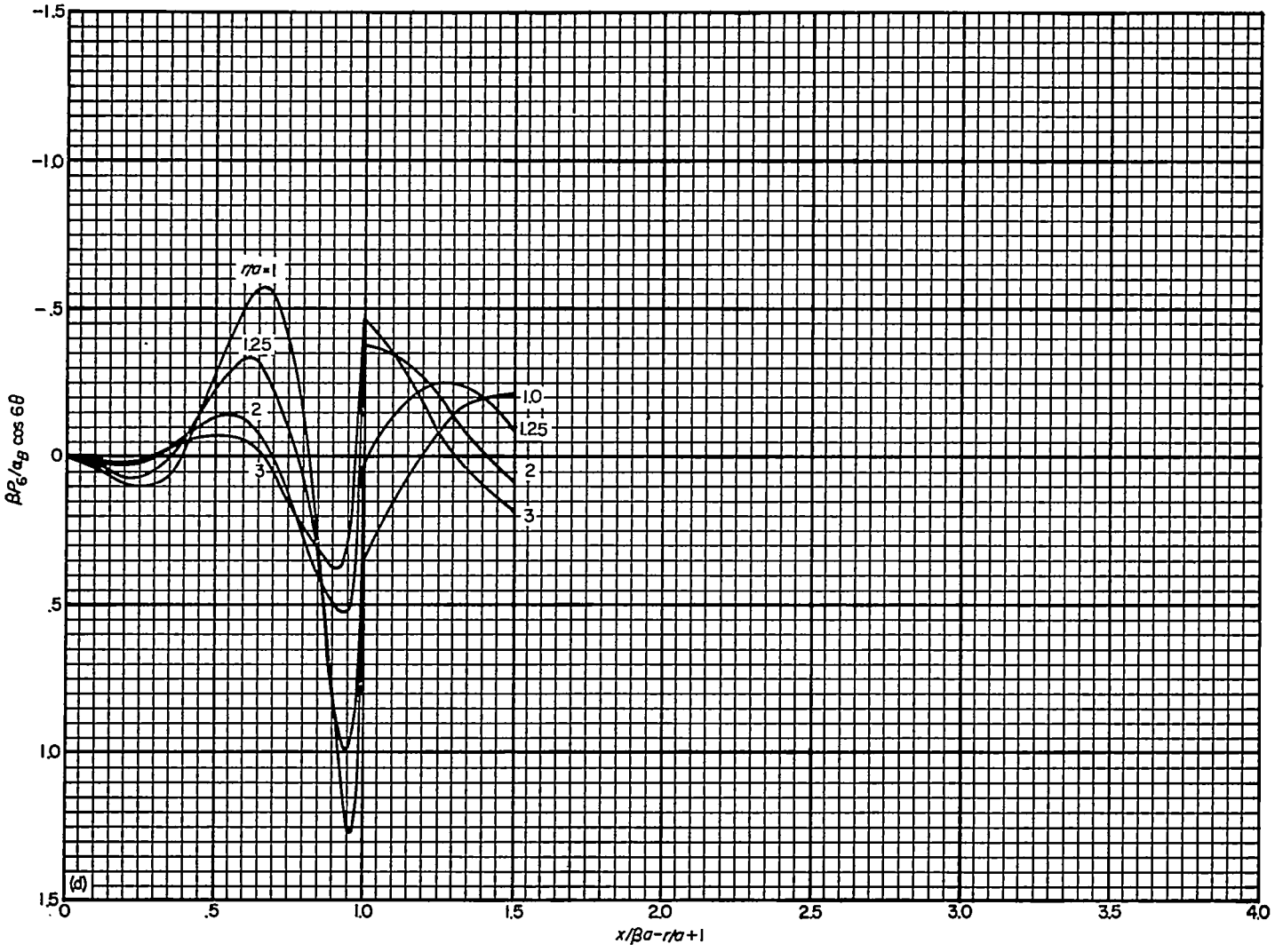

(d) $n=3$

FIGURE 21.—Concluded.

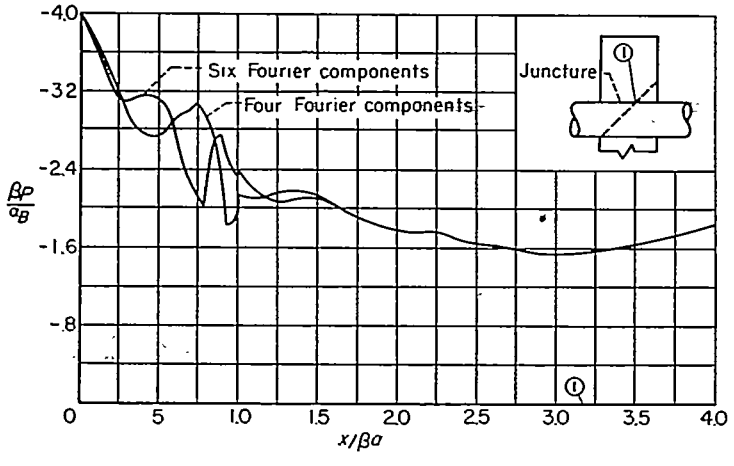

FIGURE 22.—Theoretical pressure distribution at wing-body juncture of combination using four and six Fourier components; angle-of-attack case.

However, satisfactory accuracy can be obtained by fairing a curve through this region since both end points are known.

One item of interest in figure 22 is the increase in the magnitude of $\beta P/\alpha_B$ near point 1. This is due to the influence of the opposite half-wing reaching the wing-body juncture at this point as shown in the sketch.

It should now be noted that the pressure distribution for the case of the body at angle of attack with the wing at zero angle of incidence is represented by the sum of cases (1) and (3) as given by figure 4 (a). However, we are neglecting the contribution of case (1) because it is small. The contribution to the pressure coefficient represented by case (1) is that due to a yawed infinite cylinder since we are neglecting nose effects. This contribution, which is clearly present in front of the wing, is

$$\left(\frac{P}{\alpha_B}\right)=\alpha_B(1-4\cos^2\theta) \tag{63}$$

For the juncture of the combination ($\theta=0°$) the contribution is about 0.1 for $\alpha_B=2°$ and 0.3 for $\alpha_B=6°$. At $\alpha_B=2°$ the effect is thus negligible compared to P/α_B of about 4, and at $\alpha_B=6°$ there are definite nonlinear effects that make a precise application of linear theory inaccurate. For these reasons the contribution given by equation (63) has been neglected. For the top and bottom of the body the contributions are one-third of the foregoing and hence are also negligible.

Pressure distribution on body of wing-body combination.—The pressure distribution on the body is also obtained by adding the interference pressure coefficients to the pressure coefficients due to the wing alone. The interference pressure distribution for any value of θ differs from that in the wing-body juncture, $\theta=0$, only by a $\cos 2n\theta$ factor. For example, in the juncture $\cos 2n\theta$ is always $+1$. On top of the body, $\theta=\pi/2$, $\cos 2n\theta$ alternates between $+1$ and -1 as n increases. On the $\theta=\pi/4$ meridian $\cos 2n\theta$ has values of 0, $+1$, and -1, so that when n is odd $P_{2n}=0$. The pressure distributions on the top meridian of the body and on the $\theta=45°$ meridian of the body are shown in figures 23 and 24, respectively.

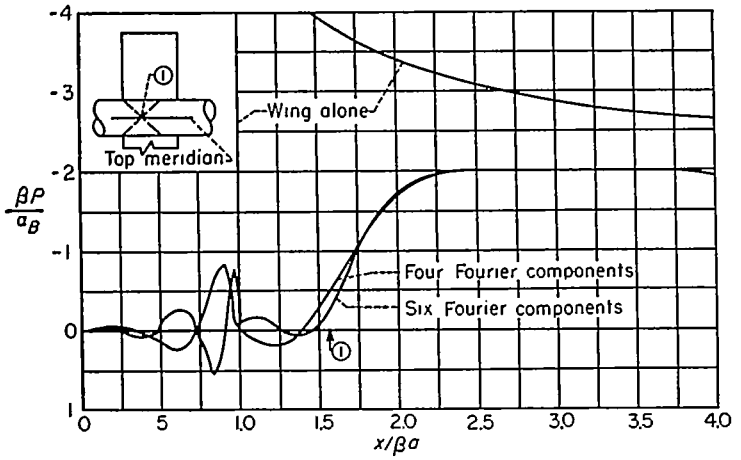

FIGURE 23.—Theoretical pressure distribution on top of combination using four and six Fourier components; angle-of-attack case.

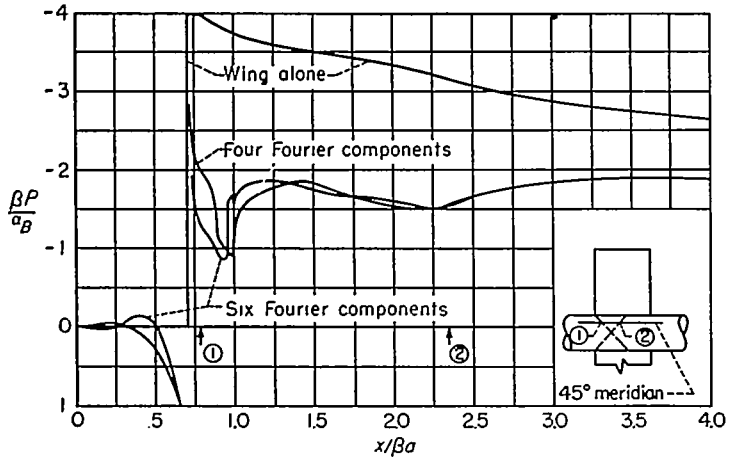

FIGURE 24.—Theoretical pressure distribution on $\theta=45°$ meridian of body of combination using four and six Fourier components; angle-of-attack case.

Several interesting effects are exhibited by figures 23 and 24. The step in the wing-alone pressure at $x/\beta a=1$ in figure 23 is effectively canceled by the interference pressure from $x/\beta a=1$ to $x/\beta a=\pi/2$, and for $x/\beta a>\pi/2$ the pressure increases rapidly. The effect of the interference pressure in canceling the effect of the wing alone on the top of the body from $x/\beta a=1$ to $x/\beta a=\pi/2$ is to be expected since the wing of the combination can have no effect on the body in front of the Mach helix (point 1 of sketch) originating at the leading edge of the wing-body juncture. If an infinite number of components had been computed, the combination pressure coefficients would be identically zero from $x/\beta a=0$ to $x/\beta a=\pi/2$. The same effects are exhibited by figure 24 except that the wing-alone step occurs at $x/\beta a=\sqrt{2}/2$ and the Mach helix intersects the meridian at $x/\beta a=\pi/4$, point 1. The Mach helix from the opposite wing panel intersects the meridian at point 2 causing an additional pressure rise. Since the region in which $\beta P/\alpha_B=0$ is known and since the exact linear theory is well approximated by four components for large values of $x/\beta a$, theoretical curves of good accuracy can be faired from figures 23 and 24. The area under the high peaks in the curves near $x/\beta a=\pi/4$ would become infinitesimal if an infinite number of interference pressure components were taken.

Pressure distribution on wing of wing-body combination.—For the region in front of the Mach wave from the leading edge of the juncture, the calculation of pressure coefficients is just a wing-alone problem. The pressure coefficients in this region can therefore be obtained directly from the wing-alone potential as given in Appendix C. The result is

$$P=-2\alpha_B\left[1+\frac{y}{(y^2-x^2)^{3/2}}\right] \tag{64}$$

In the region behind the Mach wave the pressure coefficients were obtained directly from the $W_{2n}(x, r)$ functions, as was done on the body. The results of these calculations for the wing pressure distributions are shown in figure 25 and are to be compared with the pressure distributions of figure 15.

Span loading.—The span loadings have been determined by graphical integration of the pressure-distribution curves of figures 21 to 25. For a combination with a value of $c/\beta a$ of 4 the span loadings associated with the various Fourier components are shown in figure 26, which is to be compared with figure 16 for the wing-incidence case. The magnitudes for the $n=0$ harmonic of the angle-of-attack case are about twice those for the wing-incidence case, but otherwise the two cases are similar. The span loading including wing-alone and interference effects is shown in figure 27, which is to be compared with figure 17. The important difference is noted that the peak span loading is nearly equal to the root loading in the angle-of-attack case, but is considerably greater than the root loading in the wing-

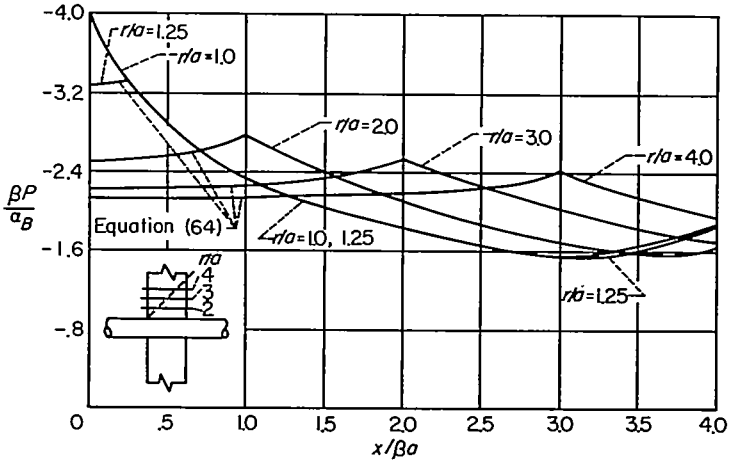

FIGURE 25.—Theoretical pressure distribution acting on wing of combination; angle-of-attack case.

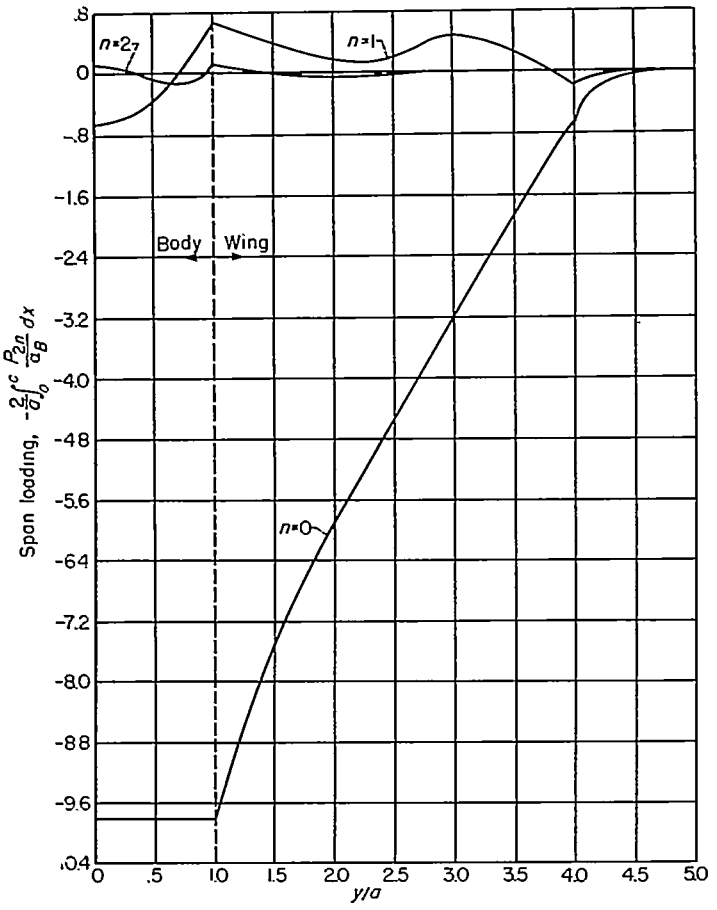

FIGURE 26.—Theoretical span loading of various Fourier components acting on combination of body and rectangular wing having effective chord-radius ratio of 4; angle-of-attack case.

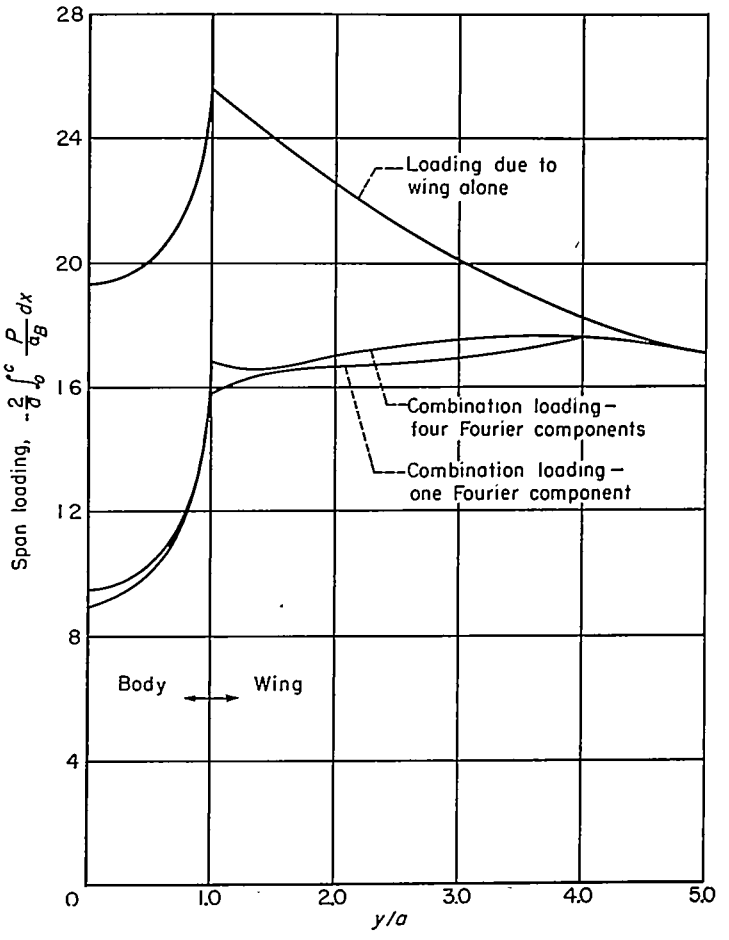

FIGURE 27.—Theoretical span loading for combination of body and rectangular wing having effective chord-radius ratio of 4; angle-of-attack case.

incidence case. Because of the difference in the shape of the span loadings, a different trailing vortex pattern would be associated with each. No effect of wing tips is included in figures 26 and 27.

Lift.—From the theoretical wing pressure distributions of the combination the lift of the wing panels in the presence of the body can be calculated as a function of βA and $c/\beta a$. To show how the body upwash is effective in increasing the lift of the wing, a factor K_W has been calculated. This factor has been defined as

$$K_W=\frac{L_{WC}}{L_W}; \qquad i_W=0 \tag{65}$$

Here L_{WC} is the lift of the panels in the presence of the body and L_W is the lift of the wing panels joined together at angle of attack α_B. In calculating L_{WC} first the lift of the exposed panels as part of the wing alone must be calculated. This was done by the use of reversibility theorems described in reference 21. The lift of the entire wing alone including the blanketed area was so determined. The lift of the blanketed area was then calculated from the potential function given in Appendix C and subtracted from the lift of the entire wing alone to get the lift of the panels. The loss of lift on the panels due to interference as determined by graphical integration was then subtracted to get L_{WC}. The values of K_W so calculated are shown in figure 28 (a) as a function of $c/\beta a$ and in figure 28 (b) as a function of a/s. Figure 28 (a) shows a large effect of βA at constant $c/\beta a$; whereas figure 28 (b) shows a small effect of βA at constant a/s.

In figure 28 (b) the effect of aspect ratio on K_W at a fixed value of a/s is less than the precision of the calculations as indicated by the cross-hatched area. For comparison the values of K_W calculated from slender-body theory have been included in the figure

$$K_W=\frac{\frac{2}{\pi}\left\{\left(1+\frac{a^4}{s^4}\right)\left[\frac{1}{2}\tan^{-1}\frac{1}{2}\left(\frac{s}{a}-\frac{a}{s}\right)+\frac{\pi}{4}\right]-\frac{a^2}{s^2}\left[\left(\frac{s}{a}-\frac{a}{s}\right)-2\tan^{-1}\left(\frac{s}{a}\right)+\pi\right]\right\}}{\left(1-\frac{a}{s}\right)^2} \tag{66}$$

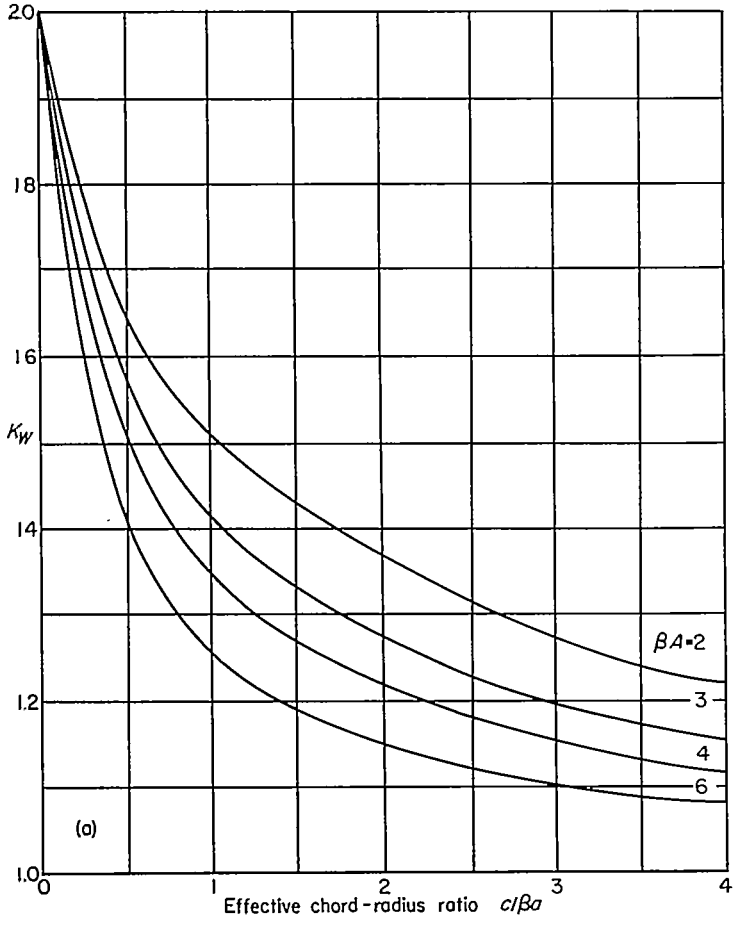

(a) Effect of chord-radius ratio.

FIGURE 28.—Lift effectiveness for rectangular wing in combination with body; angle-of-attack case.

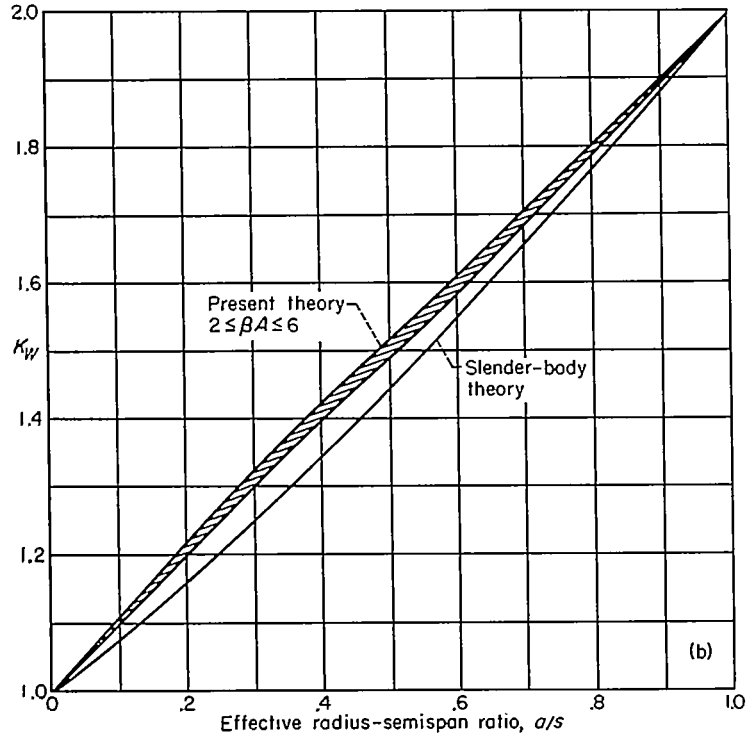

(b) Effect of radius-semispan ratio.

FIGURE 28.—Concluded.

The close agreement between the linear-theory results for the present case and the slender-body-theory results is noteworthy since the rectangular wing and body combinations considered here are not slender. This result suggests that slender-body theory can be used for calculating lift ratios for nonslender configurations.

III. COMPARISON OF EXPERIMENT AND THEORY FOR RECTANGULAR WING AND BODY COMBINATION

APPARATUS AND PROCEDURE

An investigation to evaluate the present theory was made in the Ames 1- by 3-foot supersonic wind tunnel. This wind tunnel was equipped with a flexible-plate nozzle that could be adjusted to give test-section Mach numbers from 1.2 to 2.2. The pressure measurements are obtained as photographic recordings of a multiple-tube manometer board using dibutyl phthalate as the fluid.

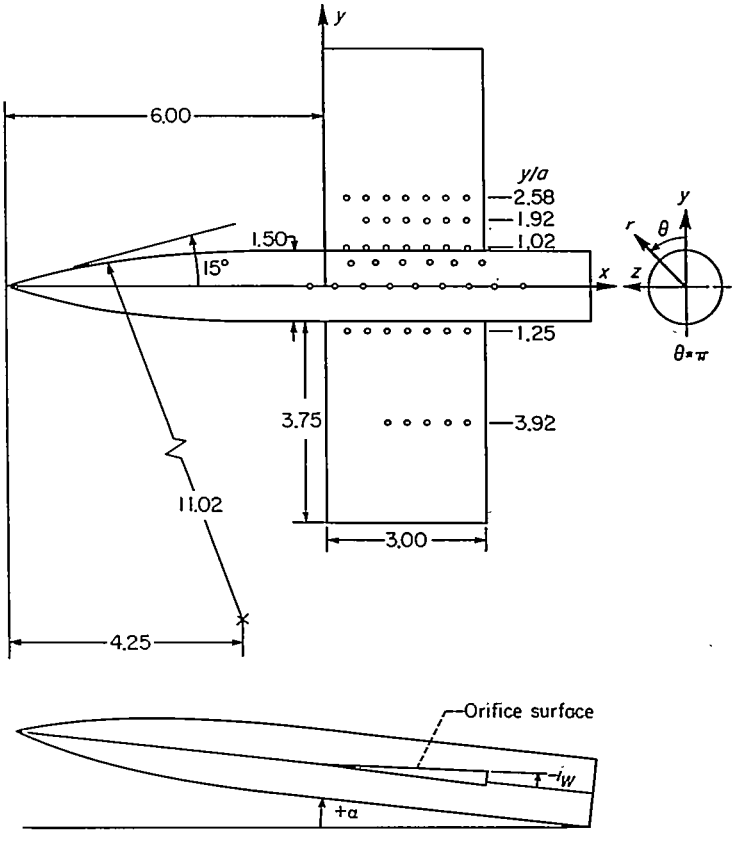

FIGURE 29.—Pressure distribution model (all dimensions in inches).

The sting-supported model, which is diagrammed in figure 29, is a combination consisting of a cylindrical body with an ogival nose and a rectangular, wedge-shaped wing. The dimensions of the model are given in figure 29. The wing was made 10 percent thick to minimize aeroelastic effects. It was mounted in the body by means of a set of angle blocks which enabled the flat wing surface containing the orifices to be set at 0°, −1.9°, −3.8°, and −5.7° angles of incidence with respect to the body center line. The pressure orifices were all located on the upper surface of the model. The 47 orifices were distributed along seven spanwise stations in order to give a comparison with theory for the wing and the body. The locations of the orifices are given in table III.

Since this investigation required a comparison of the data for several Mach numbers and Reynolds numbers at the same values of α_B and i_W, it was necessary to set α_B and i_W accurately for each measurement. The sting support by which the model was mounted had sufficient flexibility that it was deemed necessary to have means for accurately setting the values of α_B and i_W under tunnel operating conditions. The values of i_W were accurately set by means of angle blocks in the body. The angle of attack was set by a special image projection device. A mirror was inserted in the schlieren system so that an image of the model was cast upon a screen. With the wind off, the model was set at the desired value of α_B and the inclination of the model image was marked on the screen. With the tunnel in operation at the desired pressure, the angle of attack of the model was adjusted until the inclination of its image was parallel to the calibration line made on the screen with the wind off. To check this method, a horizontal and vertical wire grid was placed on the tunnel window and schlieren pictures were taken of the model while the tunnel was in operation. These pictures showed that the image projection device set α_B to within $\pm 0.07°$ of the desired value. It was especially necessary to set α_B accurately for the small angles to avoid large percentage errors in the angle setting.

The model angle of attack ranged from $+6°$ to $-6°$ in $2°$ increments, and the wing-incidence angle ranged from $0°$ to $-5.7°$ in $1.9°$ increments. The test was performed at the two Mach numbers 1.48 and 2.00 and at the Reynolds numbers of 0.6, 1.2, and 1.5 million, based on the wing chord. The model was tested for all combinations of these values of the four parameters investigated.

A complete set of data in the form of P for the Reynolds numbers 0.6, 1.2, and 1.5×10^6 at $M=1.48$ and for $R=1.5\times10^6$ at $M=2.00$ is presented in table IV. These values of P are, for the most part, averages of two readings.

REDUCTION AND ACCURACY OF DATA

All data are reduced to the coefficient form $(p-p_1)/q_o$. Actually the quantity $(p-p_T)/q_T$ was measured, and subsequent corrections were applied to change the reference static pressure to p_1 (p_1 is the static pressure at the particular orifice in question when $\alpha_B=i_W=0°$) and the reference dynamic pressure to q_o. Since p_1 includes the effects of nose thickness and stream angle, using p_1 as a reference pressure minimizes these effects and essentially gives only the pressures due to the angle settings of the model. The dynamic pressure was adjusted from q_T to q_o on the basis of a previous pressure survey of the tunnel. This latter adjustment was negligible for $M=1.48$ and amounted to less than a 3-percent correction for $M=2.00$. For the purpose of comparison with theory the pressure coefficient $(p-p_1)/q_o$ is reduced to the parameters $\beta P/\alpha_B$ for $i_W=0°$ and $\beta P/i_W$ for $\alpha_B=0°$.

Two types of errors entered into the experimental investigation: systematic errors and random errors. In this paper accuracy will be taken as the ability of the experiment to give the true values without nose effect or stream angle and, hence, is a measure of the systematic errors. Precision will be taken as the ability to repeat the data and, hence, is a measure of the random errors in the experiment.

Several factors contributed random errors. The major factor was the error in the angle-of-attack setting. The uncertainty in each angle setting was $\pm 0.07°$, but each measurement was dependent upon two angle settings: the setting for the condition represented and the setting to determine the zero correction. This leads to a net uncertainty of $0.1°$ which would account for a 5-percent error for angles of $\pm 2°$. Most of the remainder of the uncertainty in the data is due to the fact that the reference wall static pressure in the tunnel changed slightly from run to run while the total pressure remained constant. Although the magnitude of this pressure change was quite small, it was large enough compared to the small pressure differences for the $2°$ angle settings to cause as much as a 3-percent error. In addition to these factors, between 1-percent and 2-percent uncertainty was observed in reading the data from the manometer-board pictures.

To determine experimentally the precision of the data, a large number of repeat measurements were taken and compared. It was found that for α_B or $i_W=\pm 2°$, two independent determinations of $\beta P/\alpha_B$ or $\beta P/i_W$ differed from each other by ± 7 percent on the average. For α_B or $i_W=\pm 4°$ and α_B or $i_W=\pm 6°$, the experimentally determined precisions of $\beta P/\alpha_B$ and $\beta P/i_W$ are ± 4 percent and ± 2 percent, respectively. The precision in $\beta P/\alpha_B$ increases with the magnitude of the angle because a large part of the random error is due to the angle setting. The known major experimental errors are due to stream-angle and body-nose effects. The effect of these factors was not determined, but, as previously described, corrections were applied to minimize their effect, assuming the effects did not vary appreciably with angle-of-attack settings. This assumption should be good for the body-nose effect. However, it is not necessarily a good assumption for the stream-angle effect since the stream angle varies with vertical location in the tunnel and the model moves approximately 6 inches in a vertical direction between $\alpha_B=+6°$ and $\alpha_B=-6°$. Since the stream-angle correction that was used was obtained for the $\alpha_B=0°$ position in the tunnel, data obtained at $\alpha_B=0°$ should have no appreciable error due to stream angle. For other values of α_B, some error due to stream angle is possible.[5]

For the purposes of this paper, the important question is, "How well does theory predict the experimental data?" Direct comparisons between linear theory and experiment will be made only for $\alpha_B=\pm 2°$ and $i_W=-1.9°$ data. In figure 30 experimental pressure distributions in the wing-body juncture obtained from two independent measurements with $i_W=-1.9°$ and $\alpha_B=0°$ are shown together with a faired curve of their average values. The ± 7-percent limit of precision about the average value is represented by the dotted lines. The figure shows that the theoretical value generally lies between these dotted lines, and therefore the theory predicts the experimental values within the precision of the data in this example.

GENERAL PHYSICAL PRINCIPLES

Before the discussion of the results of the investigation in detail, it is well to give first a general physical description of the effects to be expected. Figures 31 and 32 show

[5] A stream-angle and pressure survey of the wind tunnel in the vertical plane of symmetry indicated that stream-angle variation caused the magnitude of the experimental values of $\beta P/\alpha_B$ to be 4 percent high on the average.

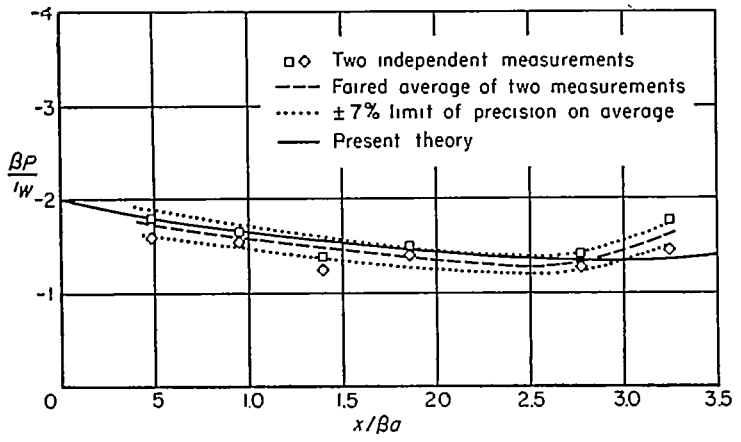

FIGURE 30.—Comparison between two independent readings of pressure distribution in wing-body juncture; $\alpha_B=0$, $i_W=1.9°$, $M=1.48$, $R=1.5\times10^6$.

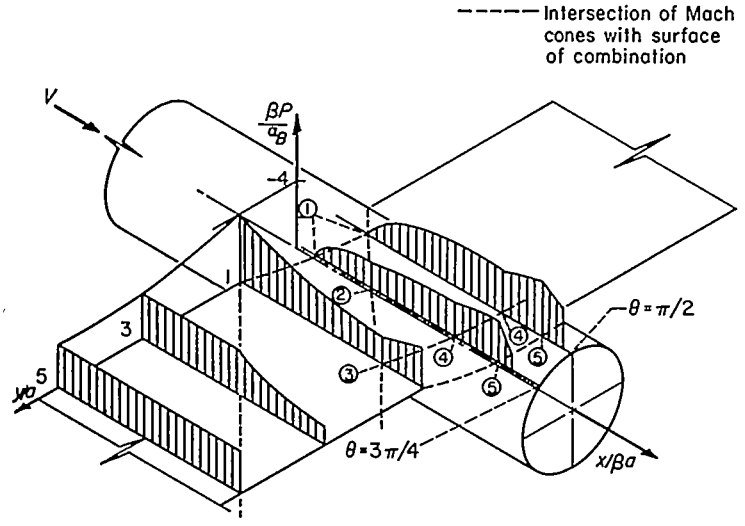

FIGURE 31.—Isometric drawing of pressure distribution acting on combination of body and rectangular wing; angle-of-attack case.

qualitatively the pressure distributions to be expected on a rectangular wing and body combination for the angle-of-attack case and the wing-incidence case, respectively. The chordwise variations of the coefficient, $\beta P/\alpha_B$ or $\beta P/i_W$, are shown for five stations by the shaded areas.[6] These figures show that Mach cones emanating from the wing-body juncture determine the points at which the various effects of wing-body interference are felt. On the cylindrical body the pressure coefficient is zero in front of the Mach helix originating at the leading edge of the wing-body juncture. The body pressure coefficients here are taken as zero because the effects of crossflow on the body pressures are very small, as shown in connection with equation (63). However, as shown by the two stations on the body, the pressure rises abruptly behind this Mach helix, point 1, in both figures. The Mach helices from the two wing panels cross the $\theta=\pi/2$ station simultaneously so that there is only one large increase in the magnitude of the pressure coefficient. These Mach helices cross the $\theta=3\pi/4$ station at two different points so that beyond point 1 there is a secondary increase in the pressure coefficients at point 2. These Mach helices continue to curl around the body until they strike the wing panel at points 3, where part of the pressure disturbance continues along the wing and part of it is reflected along another Mach helix on the body, causing a further increase in the magnitude of the pressure coefficients at points 4. Another pressure disturbance originates at the trailing edge of the wing-body juncture that causes the decrease in the magnitude of the pressure coefficients noted at points 5 of the two figures.

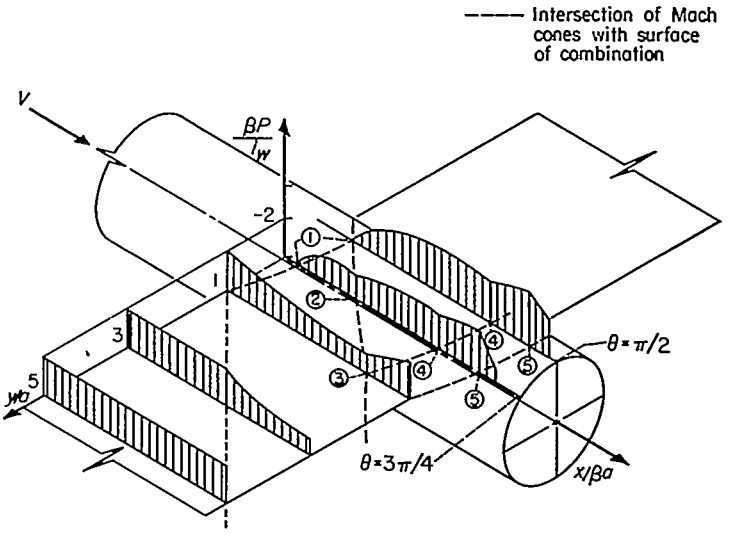

FIGURE 32.—Isometric drawing of pressure distribution acting on combination of body and rectangular wing; wing-incidence case.

On the wing of the combination the pressure coefficient is the same as that for a wing alone in front of the Mach wave from the wing-body juncture, except that when the body is at an angle of attack the body upwash effectively twists the wing in a manner such that $\alpha_W=\alpha_B(1+a^2/y^2)$. Figure 31 shows this effect of body upwash along the leading edge of the wing where the pressure coefficient decreases as y/a increases because of the effective twist of the wing. The importance of body upwash can be seen by comparing the pressure distribution along the leading edge in figure 31 with that in figure 32. The pressure coefficient at the wing-body juncture in figure 31 is twice that in figure 32 where there is no body upwash. The pressure coefficient at any given spanwise station remains nearly constant between the wing leading edge and the Mach wave from the wing-body juncture. Behind the Mach wave, interference from the wing-body juncture causes the pressure coefficient to decrease in magnitude as shown in the two figures.

EFFECTS OF ANGLE OF ATTACK

Comparisons between theory and experiment for the angle-of-attack case are made in figures 33 for data at a Reynolds number of 1.5×10^6 and Mach numbers of 1.48 and 2.00 with $i_W=0°$ and $\alpha_B=\pm2°$ and $\pm6°$.

Pressure distribution in juncture of wing-body combination.—A comparison between linear theory and experiment for the pressure distribution in the wing-body juncture is made in figures 33 (a) and 33 (b) for both Mach numbers. The sketches show the pertinent Mach lines and the span-

[6] The pressure distribution shown for the $\theta=3\pi/4$ station on the body is identical to the pressure distribution for the $\theta=\pi/4$ station due to the symmetry of the model.

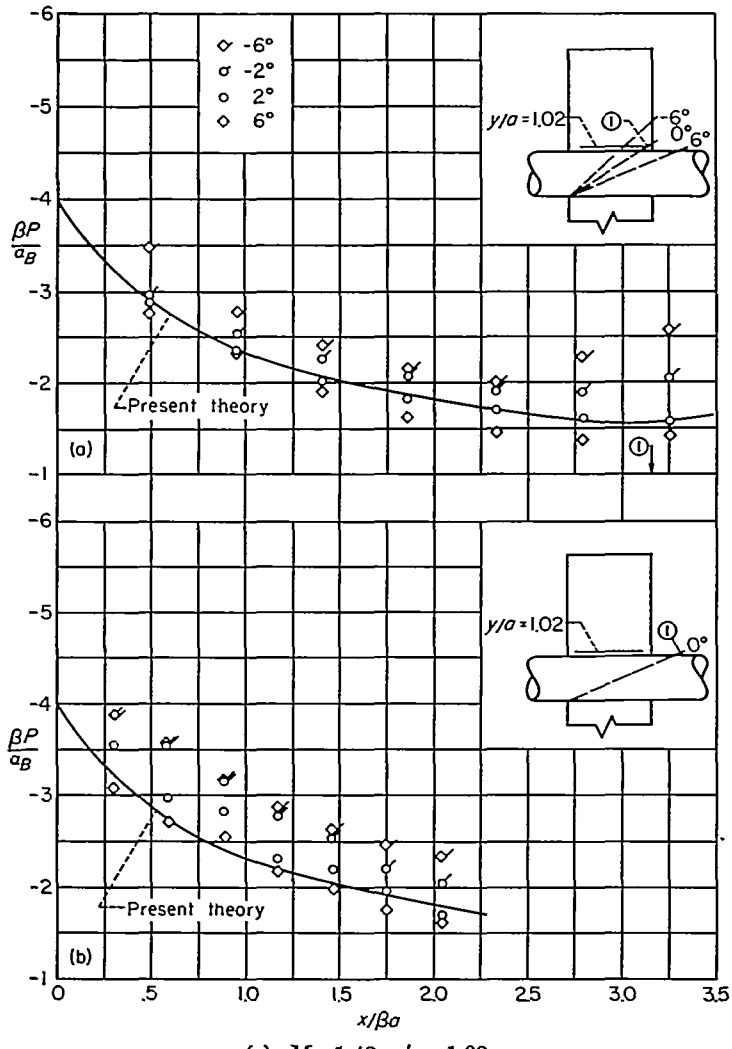

(a) M=1.48, y/a=1.02
(b) M=2.00, y/a=1.02

FIGURE 33.—Pressure distributions due to angle of attack; R=1.5×10⁶.

wise location of the orifices.[7] The experimental data points from the wing surface on which a compression occurs (negative angle of attack) are represented by flagged symbols, and the data points from the surface on which an expansion occurs (positive angle of attack) are represented by unflagged symbols. The figures show that the theory predicts the magnitude of $\beta P/\alpha_B$ about 5 percent below the average of the $\alpha_B = \pm 2°$ experimental values at M=1.48 and about 15 percent below experimental values at M=2.00. The chordwise variation is well predicted by the theory.

Linear theory predicts that the parameter $\beta P/\alpha_B$ is independent of angle of attack. Actually it is not, and the nonlinear effects of angle of attack cause a spread in the data. It is possible to evaluate approximately the variation in the parameter $\beta P/\alpha_B$ with angle of attack at the wing leading edge. First the upwash just in front of the leading edge was calculated using equation (1) which is based on linear theory. Then the pressure coefficients at the wing leading edge were computed using shock-expansion theory. The values of $\beta P/\alpha_B$ for $\alpha_B = -6°$ and $+6°$ so calculated are shown in figure 33 for values of y/a of 1.92, 2.58, and 3.92. For M=1.48 body upwash caused the shock wave to be detached from the wing in the wing-body juncture so that no calculation of the spread could be made there. For M=2.00 it was found that near the wing-body juncture the predicted spread in $\beta P/\alpha_B$ between −6° and +6° was about twice the experimental spread; whereas for y/a greater than about 1.5 the experimental spread was fairly well predicted. This difference between shock-expansion theory and the experimental data in the wing-body juncture is probably due to the combination of several things. First, near the wing-body juncture the body upwash is modified by viscous effects. Second, the theoretical spread was calculated at the leading edge of the wing, and this value was assumed to apply rearward to the first orifice. This assumption is probably good beyond y/a=1.5 where the chordwise changes in pressure are small back to the first orifice, but, in the juncture, the changes in the chordwise direction are large near the wing leading edge so that this assumption is probably invalid. Third, the contribution of the body crossflow field previously mentioned is present (eq. (63)).

Another phenomenon not predicted by linear theory is shown by figure 33 (a). The linear theory predicts that the

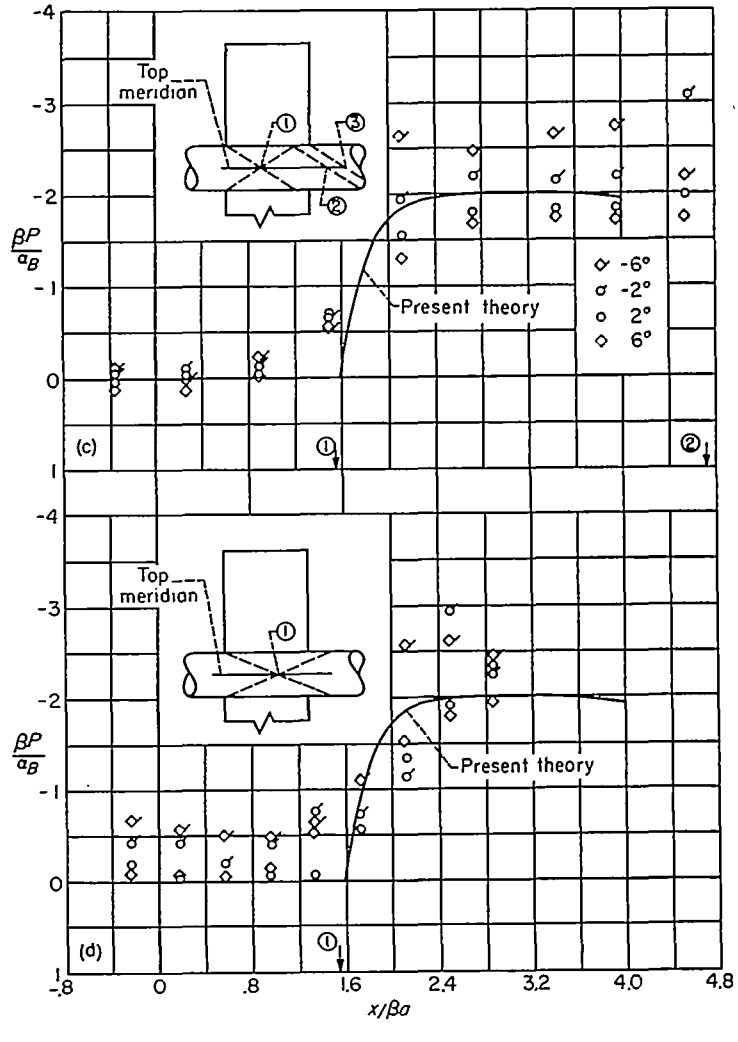

(c) M=1.48, top meridian.
(d) M=2.00, top meridian.

FIGURE 33.—Continued.

[7] The location of these Mach lines is only qualitative because the calculations were made using shock-expansion theory, with the assumption that there was no local Mach number variation behind the leading edge of the wing. To simplify the sketches, the Mach helices on the body are represented as straight lines.

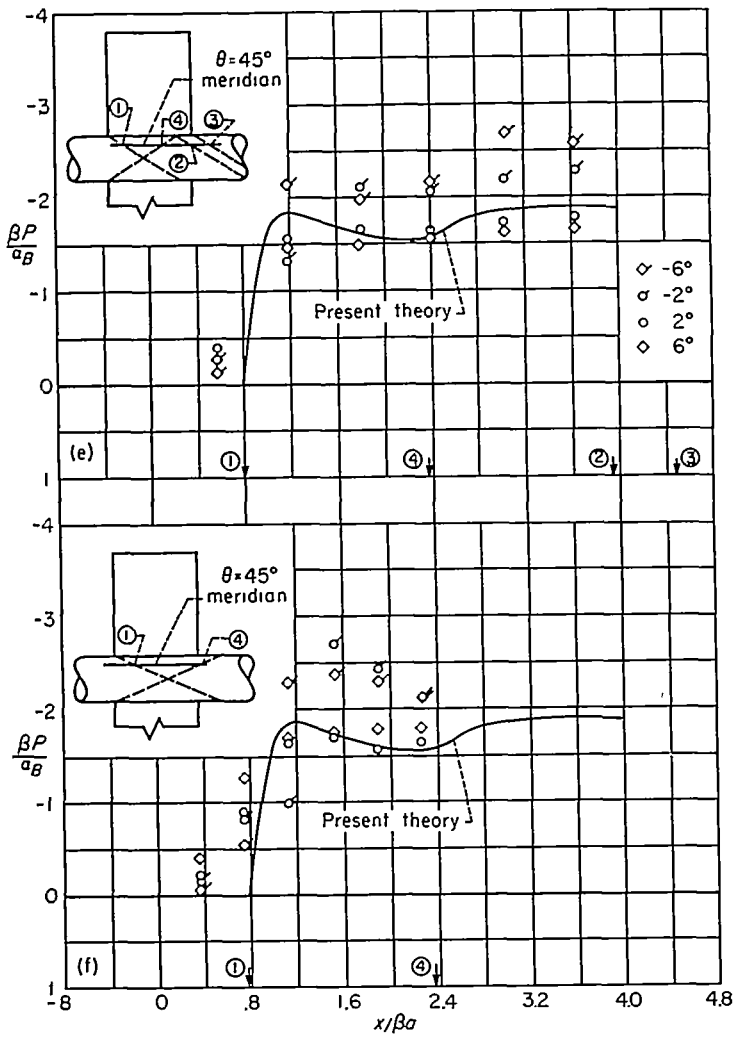

(e) $M=1.48$, $\theta=45°$ meridian.
(f) $M=2.00$, $\theta=45°$ meridian.

FIGURE 33.—Continued.

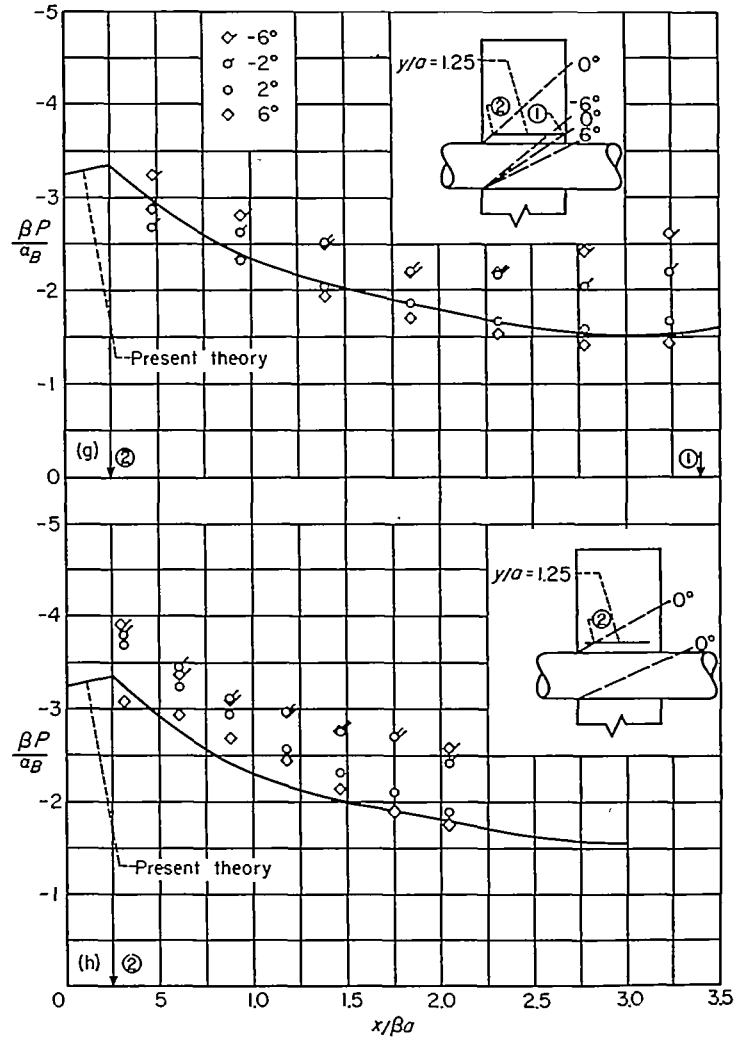

(g) $M=1.48$, $y/a=1.25$
(h) $M=2.00$, $y/a=1.25$

FIGURE 33.—Continued.

Mach helix from the opposite wing panel (see sketch) should intersect the wing-body juncture at point 1, causing an increase in the magnitude of $\beta P/\alpha_B$. This effect is observed experimentally for negative values of α_B in front of point 1 rather than exactly at point 1. The reason is that for negative values of α_B a compression occurs on the orificed surface reducing the local Mach number from the free-stream Mach number, thus increasing the Mach angle and causing the Mach helix to shift forward. The result is the spread of the data shown in figure 33 (a) near point 1. This effect is not shown by figure 33 (b) because the Mach helix lies more rearward for $M=2.00$ so that the orifices do not extend to the Mach helix as shown by the sketch.

Figures 33 (a) and 33 (b) show that Mach number has no effect upon the magnitude of the higher-order spread due to angle of attack or upon the chordwise variation of $\beta P/\alpha_B$, but on the average the magnitude of $\beta P/\alpha_B$ is about 10 percent higher for $M=2.00$ than for $M=1.48$.

Pressure distribution on top meridian of body of wing-body combination.—A comparison between the linear theory and experiment for the pressure distribution on the top meridian of the body is made in figures 33 (c) and 33 (d). These figures show that theory and experiment are in good accord for $\alpha_B=\pm2°$, particularly at $M=1.48$. However, nonlinear effects due to α_B cause a large spread between the data for $\alpha_B=+6°$ and $\alpha_B=-6°$. All the effects predicted to occur on the body in the section of the report "General Physical Principles" are observed experimentally, but not exactly at the points predicted because of nonlinear effects. The pressure rise predicted at point 1 of figures 33 (c) and 33 (d) occurs prematurely and is less abrupt than expected for all angles of attack because of the boundary layer on the body. The variation in local Mach number causes the Mach helices to shift forward for the negative angles of attack as discussed in the section treating the wing-body juncture. The increase in the magnitude of $\beta P/\alpha_B$ expected at point 2, $x/\beta a=3\pi/2$, actually occurs at about $x/\beta a=4$ for $\alpha_B=-2°$. The decrease in magnitude of $\beta P/\alpha_B$ that is expected at point 3 actually occurs at about $x/\beta a=4.0$ for $\alpha_B=-6°$. For the positive angles of attack the Mach helices are shifted rearward so that these effects are not observed experimentally in the range of $x/\beta a$ measured.

Figures 33 (c) and 33 (d) show that, in general, the $M=1.48$ data are predicted better by the theory than are the $M=2.00$ data. For $M=2.00$ there is an unexpectedly large pressure coefficient in front of point 1 for negative

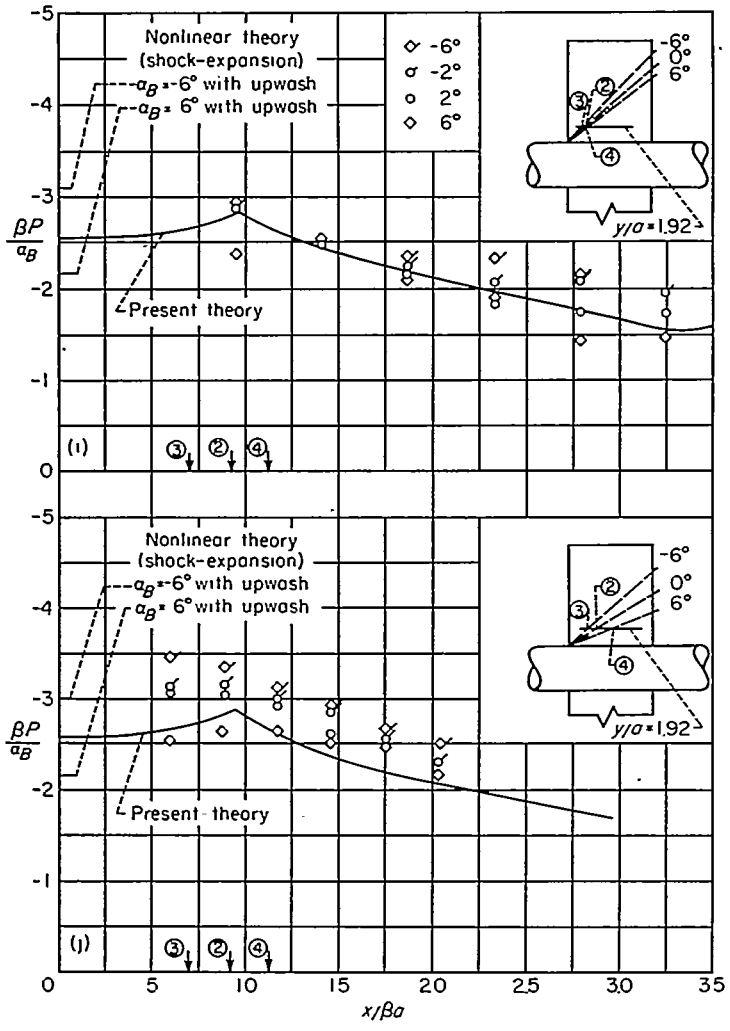

(i) M=1.48, y/a=1.92
(j) M=2.00, y/a=1.92

FIGURE 33.—Continued.

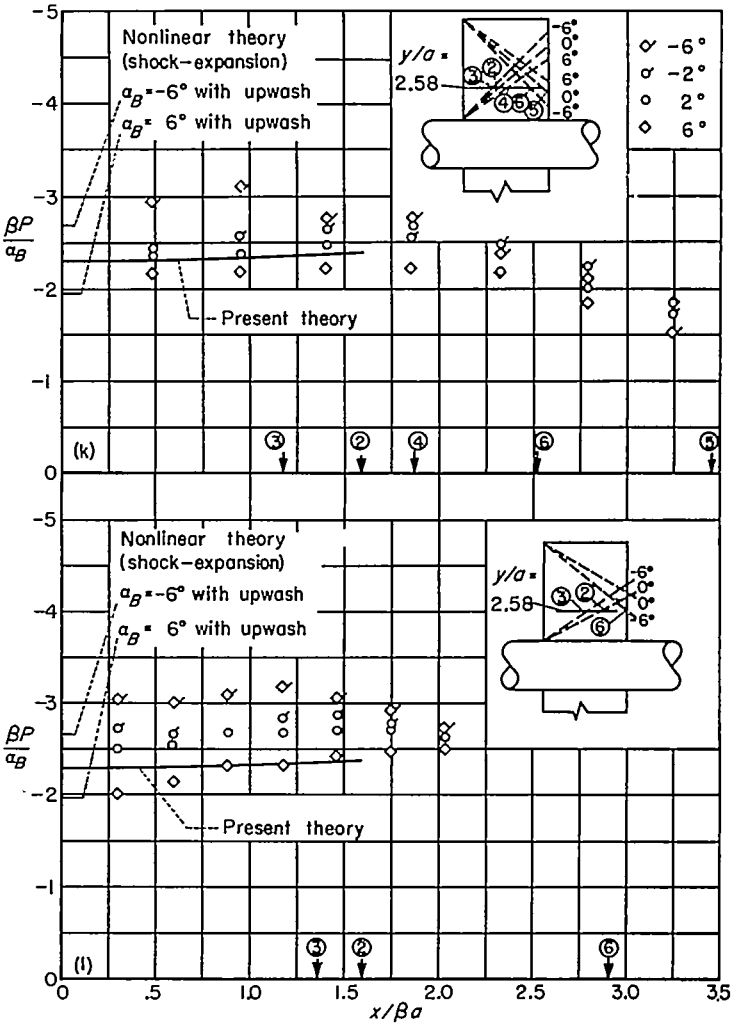

(k) M=1.48, y/a=2.58
(l) M=2.00, y/a=2.58

FIGURE 33.—Continued.

angles of attack. The predicted pressure coefficient due to crossflow is only about 0.1 in units of the ordinate and hence does not account for the observed effect at M=2.00. For α_B=−2° and M=2.00, $\beta P/\alpha_B$ dips slightly near point 1 and then rises and overshoots the α_B=−6° data. This effect is due to the boundary-layer condition on the body and will be discussed in detail in the section dealing with Reynolds number effect.

Pressure distribution on θ=45° meridian of body of wing-body combination.—A comparison between the linear theory and experiment for the pressure distribution on the θ=45° meridian of the body is made in figures 33 (e) and 33 (f). Essentially the same effects are shown on this meridian as on the top meridian.

Just as for the top meridian of the body the experiment is, in general, better predicted by the theory for M=1.48 than for M=2.00, and the same boundary-layer effects are evident near point 1 for M=2.00.

Pressure distribution on wing of wing-body combination.—Experimental chordwise pressure distributions on the wing are shown in figures 33 (g) to 33 (n) for the four spanwise orifice stations y/a=1.25, 1.92, 2.58, and 3.92. In front of the Mach cone from the wing-body juncture no interference is felt from the wing-body juncture so that the theoretical pressure distribution for a wing alone in the body upwash field is used in this region. Figures 33 (g) to 33 (n) show that on the average the wing-alone theory predicts magnitudes of $\beta P/\alpha_B$ about 5 percent below the measurements for α_B= ±2° for M=1.48 and about 12 percent below the measurements for M=2.00. The spread in the data between α_B=+6° and α_B=−6° is fairly well predicted by shock-expansion theory for y/a greater than about 1.5 (figs. 33 (i) to 33(n)). At y/a=1.25 the predicted spread (not shown) is too large, just as for the wing-body juncture.

Some of the interference effects discussed in the section of the report entitled "General Physical Principles" are illustrated in figures 33 (g) to 33 (n). The interference effect from the opposite wing panel is observed in figure 33 (g) where, just in front of point 1, the same spread in the data occurs as in the wing-body juncture. According to linear theory the disturbance originating at the nearer wing-body juncture should be felt at point 2 of figures 33 (i) to 33 (m), and the magnitude of $\beta P/\alpha_B$ should begin to decrease from the wing-alone value there. These figures show that the magnitude of $\beta P/\alpha_B$ does decrease in the neighborhood of point 2. They also show that, in general, the α_B=+6° and the α_B=−6°

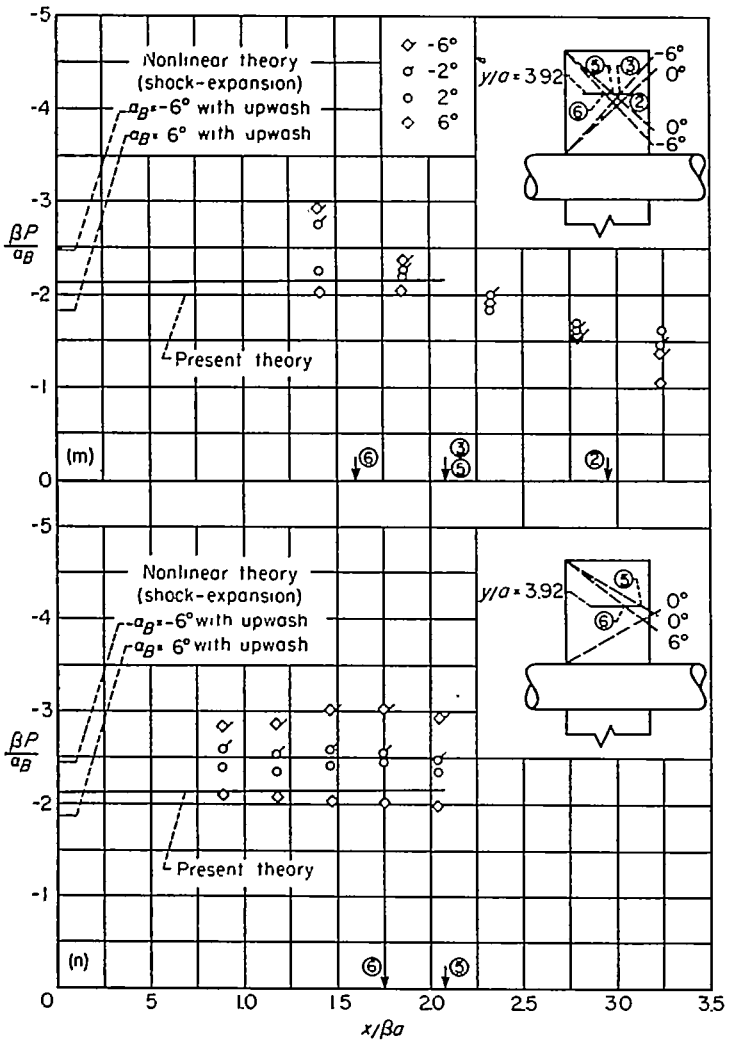

(m) $M=1.48$, $y/a=3.92$
(n) $M=2.00$, $y/a=3.92$

FIGURE 33.—Concluded.

data come together in the neighborhood of point 2. This convergence is due to a variation in the local Mach number with α_B. This is shown by the sketch in figure 33 (j) where the disturbance from the wing-body juncture is first felt at point 3 for $\alpha_B=-6°$, whereas it is first felt at point 4 for $\alpha_B=+6°$. Since the magnitude of $\beta P/\alpha_B$ begins to decrease as soon as this disturbance is felt, the magnitude of $\beta P/\alpha_B$ begins to decrease at a smaller value of $x/\beta a$ for $\alpha_B=-6°$ than for $\alpha_B=+6°$, thus causing the convergence observed. The sketches in figures 33 (k) and 33 (m) show that the disturbance from the wing tip should also cause the $\alpha_B=+6°$ and $\alpha_B=-6°$ data to come together beyond point 6 in these figures. The figures show that the data not only come together but actually cross over and reverse order just beyond point 6.

The only significant effect of Mach number shown by figures 33 (g) to 33 (n) is the approximately 10-percent-larger values of $\beta P/\alpha_B$ for $M=2.00$ than for $M=1.48$. Nearly 40 percent of this difference may be due to differences in stream angle in the wind tunnel for the two Mach numbers.

Span load distribution.—Span loading is defined for both the body and the wing as the integral (see eq. (57))

$$\int_o^{c/\beta a}\left[\left(\frac{\beta P_L}{\alpha_B}\right)-\left(\frac{\beta P_U}{\alpha_B}\right)\right]d\left(\frac{x}{\beta a}\right)=-\int_o^c\left(\frac{2P}{\alpha_B}\right)dx \qquad \text{if } a=1$$

The experimental and theoretical results for the span loading distribution on the wing and body of the combination are presented in figure 34. No account has been taken of tip

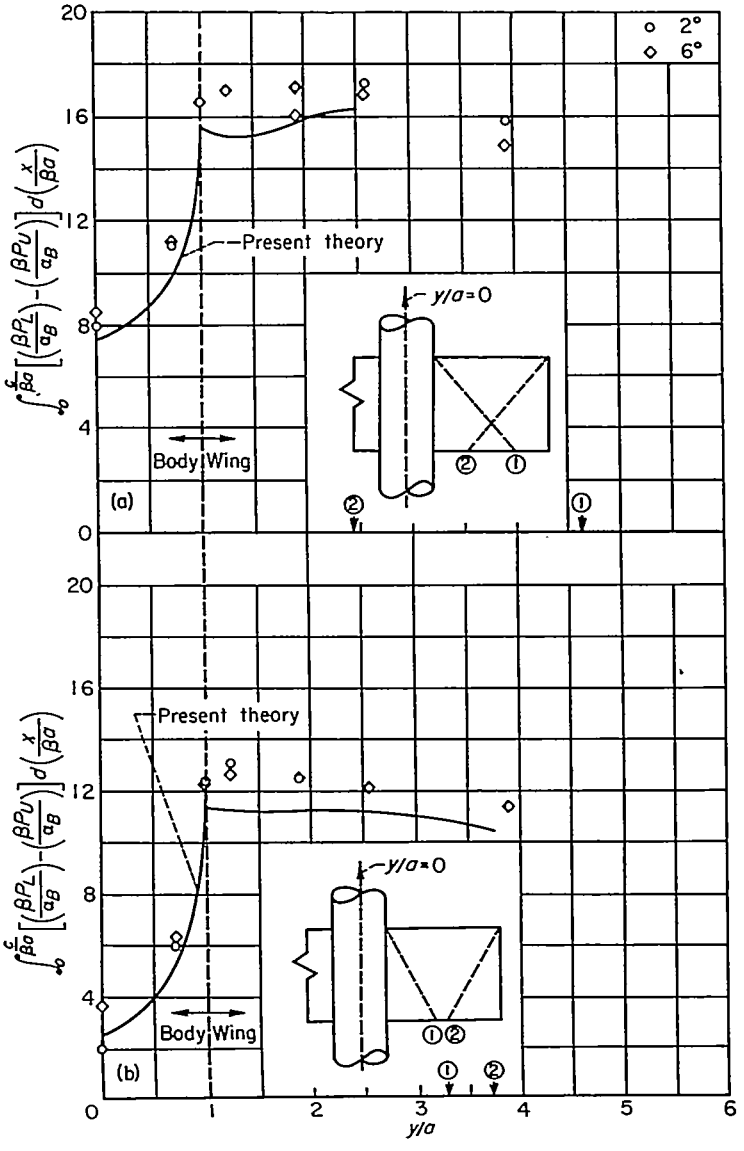

(a) $M=1.48$
(b) $M=2.00$

FIGURE 34.—Span load distributions due to angle of attack; $R=1.5\times10^6$.

effects in calculating the span loading because the twist of the wing makes a determination of these effects a difficult wing problem. The theory is thus valid only inboard of point 2. If an approximate answer is needed, the Busemann tip solution (ref. 20) can be joined onto the span loading at point 2. Figure 34 shows that the theory is generally about 10 percent below experiment. This result is not surprising in view of the comparisons between the experimental and theoretical pressure distributions of figure 33. Of particular interest is the fact that, in general, the higher-order differences due to α_B that were so large for the pressure-distribution results are negligible for the span loading distribution. The only exception is on the top of the body, $y/a=0$, and $M=2.00$, where the effects of boundary-layer and shock-wave inter-

action are large. The explanation for the independence from α_B is that the higher-order effects on the top surface are compensated for by higher-order effects of the same magnitude on the lower surface so that the net loading per unit angle is very nearly independent of angle of attack.

EFFECT OF WING-INCIDENCE ANGLE

Comparison is made between theory and experiment for the wing-incidence case for data taken at a Reynolds number of 1.5×10^6 and Mach numbers of 1.48 and 2.00 with $\alpha_B=0°$ and $i_W=-1.9°$ and $-5.7°$. It will be remembered from the section on the accuracy of data that there is no appreciable error due to stream angle for the wing-incidence case, and the comparison between experiment and theory reflects this fact.

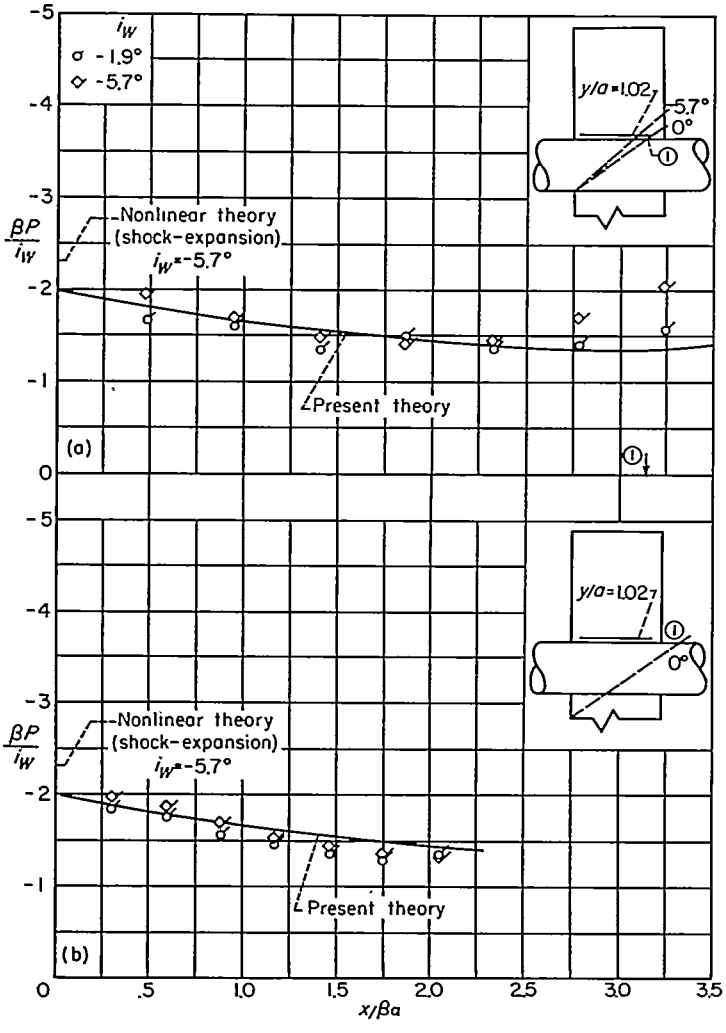

(a) $M=1.48$, $y/a=1.02$
(b) $M=2.00$, $y/a=1.02$

FIGURE 35.—Pressure distributions due to wing incidence; $R=1.5\times10^6$.

Pressure distribution in wing-body junctures.—The linear theory and experimental pressure distributions in the wing-body juncture are compared in figures 35 (a) and 35 (b). The symbols in the figures are flagged to be consistent with the use of flagged symbols for negative angle-of-attack data. The figures show that the experimental values are about 5 percent below those predicted by the theory for $i_W=-1.9°$. The magnitude of the nonlinear effects due to i_W is predicted at the leading edge by shock-expansion theory. Figures

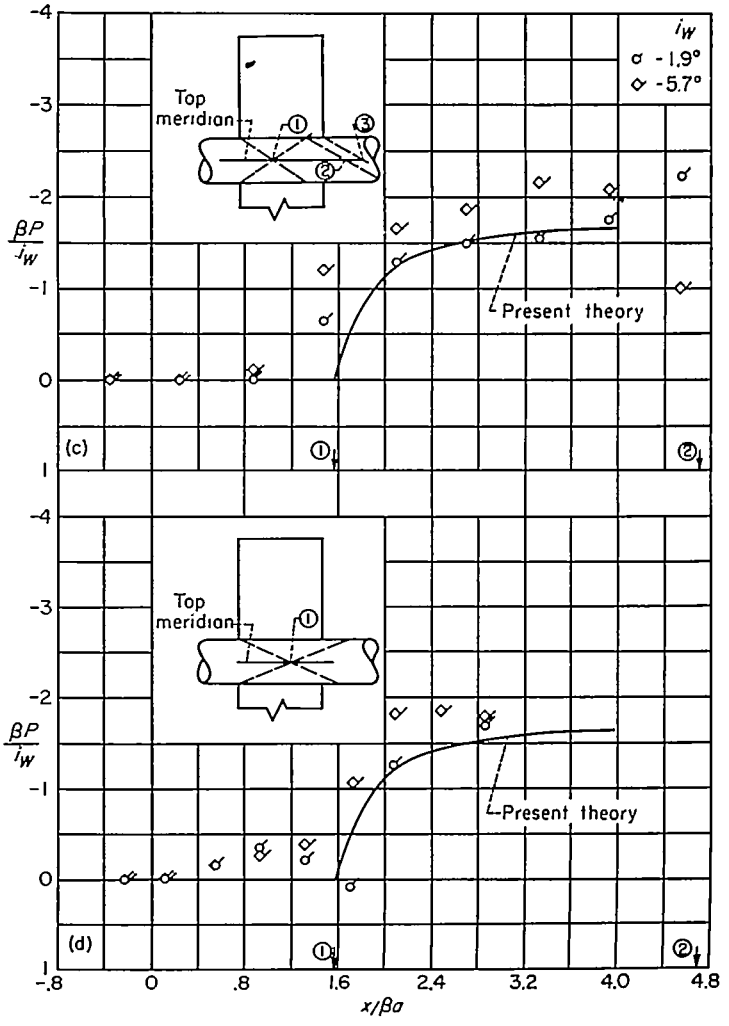

(c) $M=1.48$, top meridian.
(d) $M=2.00$, top meridian.

FIGURE 35.—Continued.

35 (a) and 35 (b) show that the spread predicted in this manner can account for the experimental results. The premature increase in the magnitude of $\beta P/i_W$ near point 1 is due to the effect of the opposite wing panel and variation of the local Mach number as discussed in the angle-of-attack section. No significant effect of Mach number was found on the parameter $\beta P/i_W$.

Pressure distribution on top meridian of body of wing-body combination.—A comparison between the linear theory and experiment for the pressure distribution on the top meridian of the body is made in figures 35 (c) and 35 (d). These figures show that theory and experiment are in good accord for $i_W=-1.9°$. However, nonlinear effects due to i_W cause much larger differences between theory and experiment for $i_W=-5.7°$. This is consistent with the angle-of-attack case where the higher-order effect due to α_B was large for negative angles of attack.

All of the effects observed for the angle-of-attack case due to disturbances from the wing are also shown to occur for the wing-incidence case in figures 35 (c) and 35 (d). The paths of these disturbances as predicted by linear theory are shown on the sketch, and the positions at which the effects are expected to occur are shown on the abscissa.

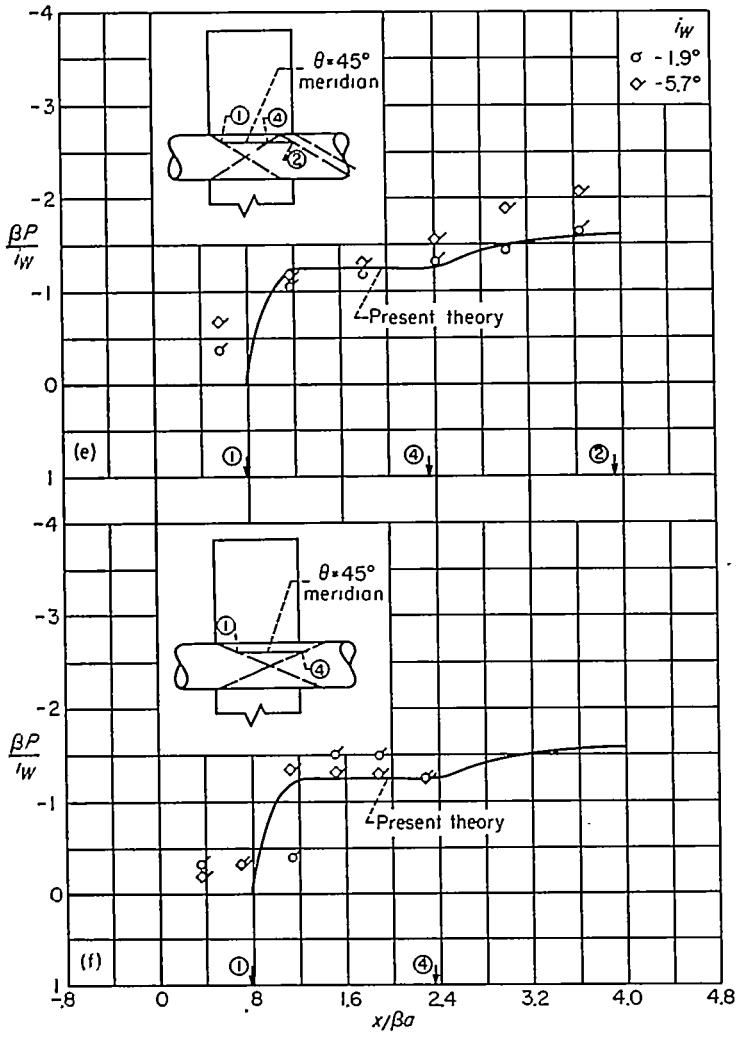

(e) $M=1.48$, $\theta=45°$ meridian.
(f) $M=2.00$, $\theta=45°$ meridian.

FIGURE 35.—Continued.

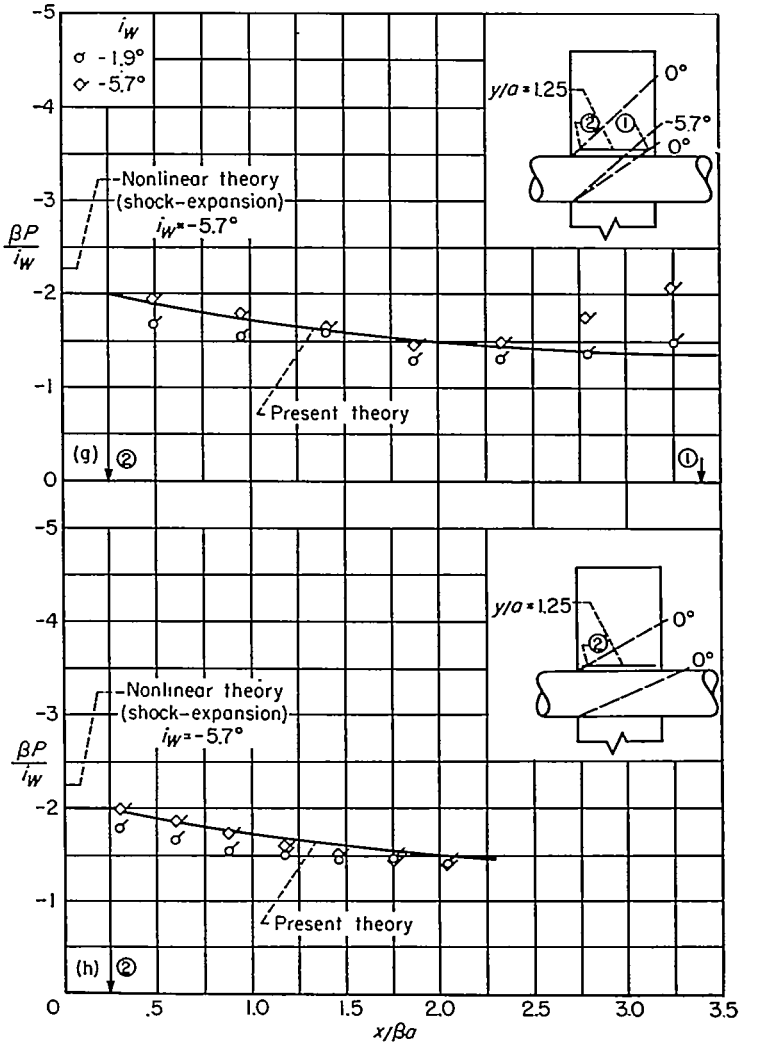

(g) $M=1.48$, $y/a=1.25$
(h) $M=2.00$, $y/a=1.25$

FIGURE 35.—Continued.

The only significant effect of Mach number apparent in figures 35 (c) and 35 (d) is the larger boundary-layer and shock-wave interaction for $M=2.00$ than for $M=1.48$ near point 1. The $M=2.00$ experimental data for $i_W=-1.9°$ dip and then overshoot at this point. This phenomenon is discussed in more detail in the section of the report on Reynolds number effect.

Pressure distribution on $\theta=45°$ meridian of body of wing-body combination.—Linear theory is compared with experimental results for the pressure distribution on the $\theta=45°$ meridian of the body of the combination in figures 35 (e) and 35 (f). The effects shown by the figure are consistent with those shown for the angle-of-attack case and for the wing-incidence case on the top meridian of the body.

Pressure distribution on wing of wing-body combination.—A comparison between linear theory and experiment for the pressure distribution along several spanwise stations is made in figures 35 (g) to 35 (n). The experimental data (figs. 35 (k) and 35 (*l*)) show that, in general, $\beta P/i_W$ for the $i_W=-1.9°$ data is constant and nearly equal to -2 in front of the Mach cone. Behind the Mach cone the theory generally predicts values about 5 percent above the experimental data for $i_W=-1.9°$. The higher-order effects due to i_W cause larger differences between linear theory and experiment for $i_W=-5.7°$. The figures show that these differences are well predicted by shock-expansion theory. The effects due to the influence of the Mach waves are the same as those discussed for the angle-of-attack case. There is no effect of Mach number evident on the wing of the wing-body combination other than that predicted by linear theory.

Span load distribution.—A comparison between the theoretical and experimental results for span load distribution on the wing and body of the combination is made in figure 36 for $i_W=-1.9°$. The decrease in the span loading due to the wing tip was calculated by the method of Busemann (ref. 20). In part (a) of figure 36, interference from both the body and the wing tip is felt between points 1 and 2, but in part (b) no interference is felt between points 1 and 2, and the span loading is that of a two-dimensional wing alone.

Figure 36 shows that, in general, the experiment is 5 percent lower than the linear-theory prediction. Since all pressure measurements for the wing-incidence case were made for negative values of i_W, the experimental values used in this figure were obtained by doubling the values of $\beta P/i_W$ obtained for $i_W=-1.9°$ rather than by considering

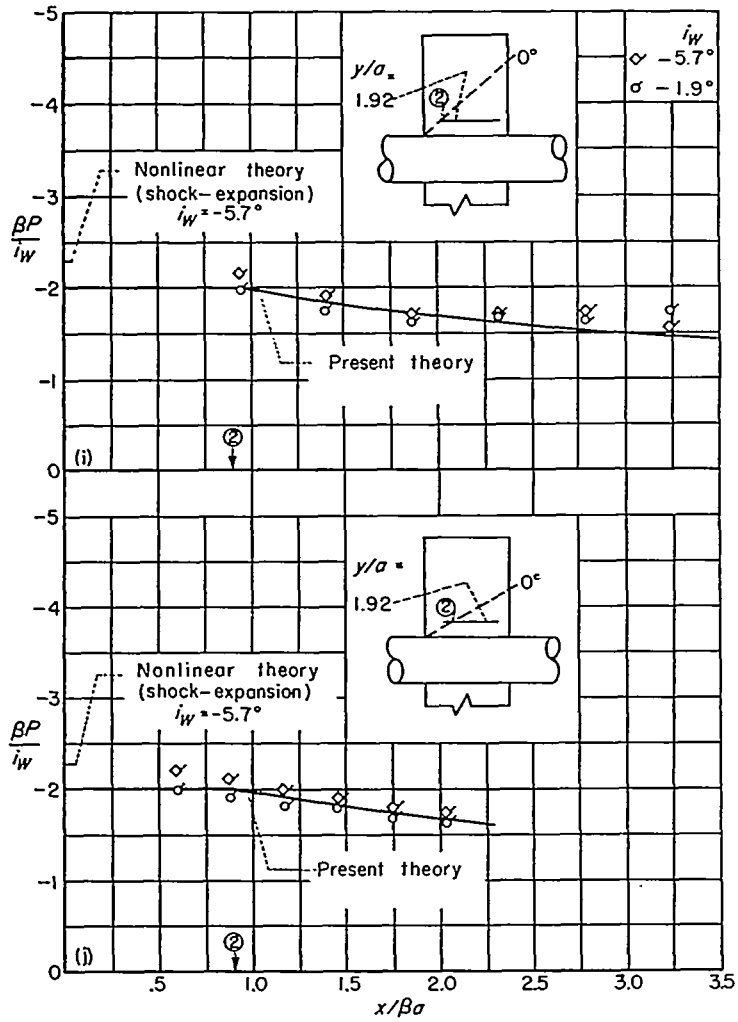

(i) M=1.48, y/a=1.92
(j) M=2.00, y/a=1.92

FIGURE 35.—Continued.

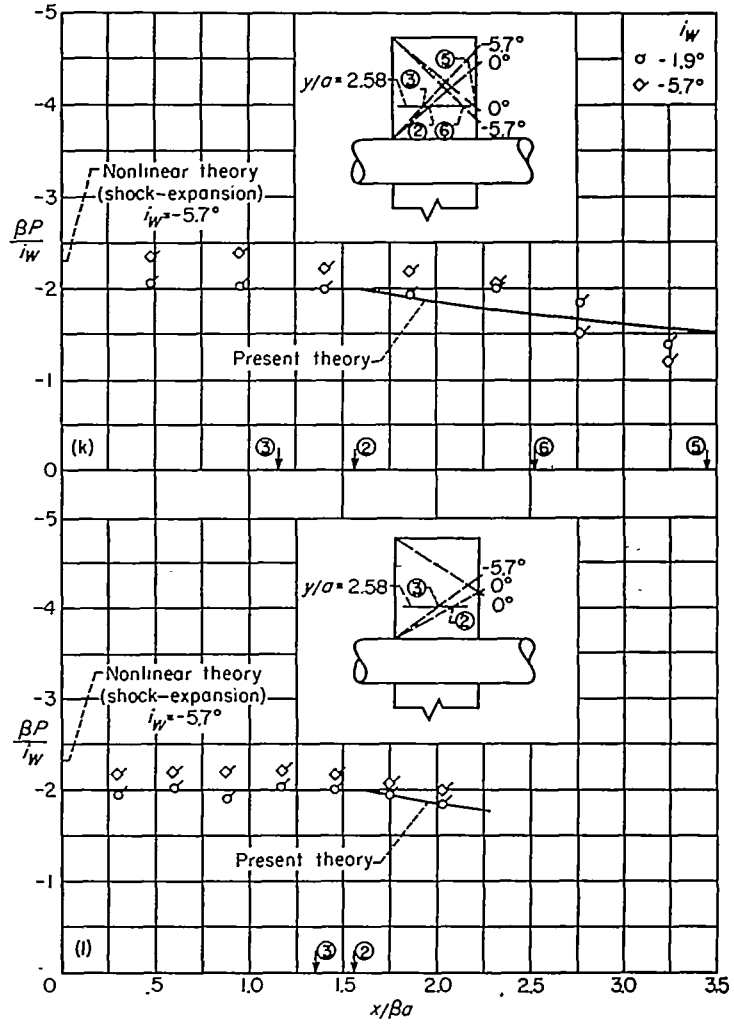

(k) M=1.48, y/a=2.58
(l) M=2.00, y/a=2.58

FIGURE 35.—Continued.

two surfaces as for the angle-of-attack case. Since this increases the nonlinear effects of i_W rather than minimizing them, only the $i_W=-1.9°$ data (for which the nonlinear effects are small) were plotted. However, the present method is applicable to the prediction of the net span loading for larger values of i_W because the nonlinear effects on the upper and lower surfaces tend to cancel each other, as shown for the angle-of-attack case.

EFFECT OF REYNOLDS NUMBER

The primary effect of Reynolds number in this investigation was on the body. Reynolds number was found to have no significant effect on the pressure distribution on the wing of the combination for the range investigated. Figure 37 shows the boundary-layer condition, as observed in schlieren pictures, on top of the body at the point of intersection with the Mach wave from the leading edge of the wing-body juncture for R=0.6 and 1.5×10^6. The transition and separation regions shown in figure 37 indicate approximately the ranges of α_B and i_W in which the boundary layer changes from laminar to turbulent or separated flow at the Mach wave from the wing-body juncture. In laminar and turbulent regions the flow remains laminar or turbulent across the Mach wave. Some of the Reynolds number effect shown by figure 37 may be due to changes in the turbulence level of the wind tunnel.

It is to be expected that data obtained for several angle combinations within any one of the regions shown in figure 37 would show no significant differences due to viscous effects, but that these data would differ from data in other regions. For example, for M=1.48 and $R=0.6\times10^6$ the data for $\alpha_B=-2°$ with $i_W=0°$ should differ from the data for $\alpha_B=-6°$ with $i_W=0°$ because transition occurs at the shock wave for the latter case but not for the former. That there is a difference is shown in figure 38 where the pressure distributions on top of the body for these two conditions are compared. In front of the shock wave the flow is laminar for both angles of attack so that there is no difference in the two sets of data. However, for $\alpha_B=-6°$ transition occurs at the shock wave and the pressure rises as predicted, while for $\alpha_B=-2°$ laminar flow persists behind the point at which the shock is expected and the pressure rise occurs much later than predicted. In fact, the pressure rise does not occur until the transition point shown in the figure is reached, and then it tends to overshoot. This phenomenon of the delayed pressure rise was observed to occur whenever laminar flow

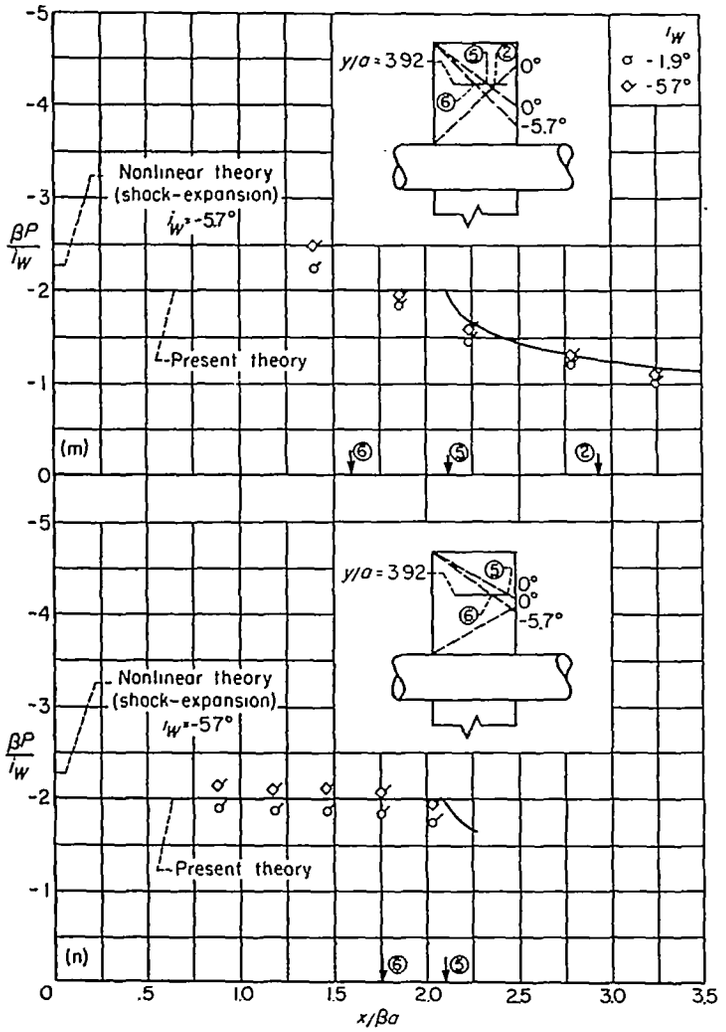

(m) $M=1.48$, $y/a=3.92$
(n) $M=2.00$, $y/a=3.92$

FIGURE 35.—Concluded.

persisted beyond the point at which a shock wave from the wing was predicted to exist. When the disturbance from the wing is an expansion wave, the pressure-coefficient curves rise approximately as predicted, regardless of the type of boundary layer. The conditions for which this delayed pressure rise was observed to occur are shown by the dotted areas in figure 37. Two other examples of this phenomenon may be seen near points 1 of figures 33 (d) and 35 (d) for $\alpha_B=-2°$, $i_W=0°$ and $\alpha_B=0°$, $i_W=-1.9°$, respectively.

In figure 39, the pressure distributions on top of the body are compared for three Reynolds numbers. It is shown that data for the two highest Reynolds numbers, $R=1.2$ and 1.5×10^6, agree well, while the data for the lowest Reynolds number differ from those for the higher Reynolds numbers.

COMPARISON WITH THEORY FROM OTHER SOURCES

The three theories for which numerical results are available are compared in figure 40. The theory due to Ferrari was obtained by cross-plotting from a figure in reference 22 so that the curve shown is only approximate. The theoretical curve due to Morikawa is obtained from tabulated results given in reference 4. The experimental-data region was determined by the extreme values obtained for $\alpha_B=\pm2°$ for

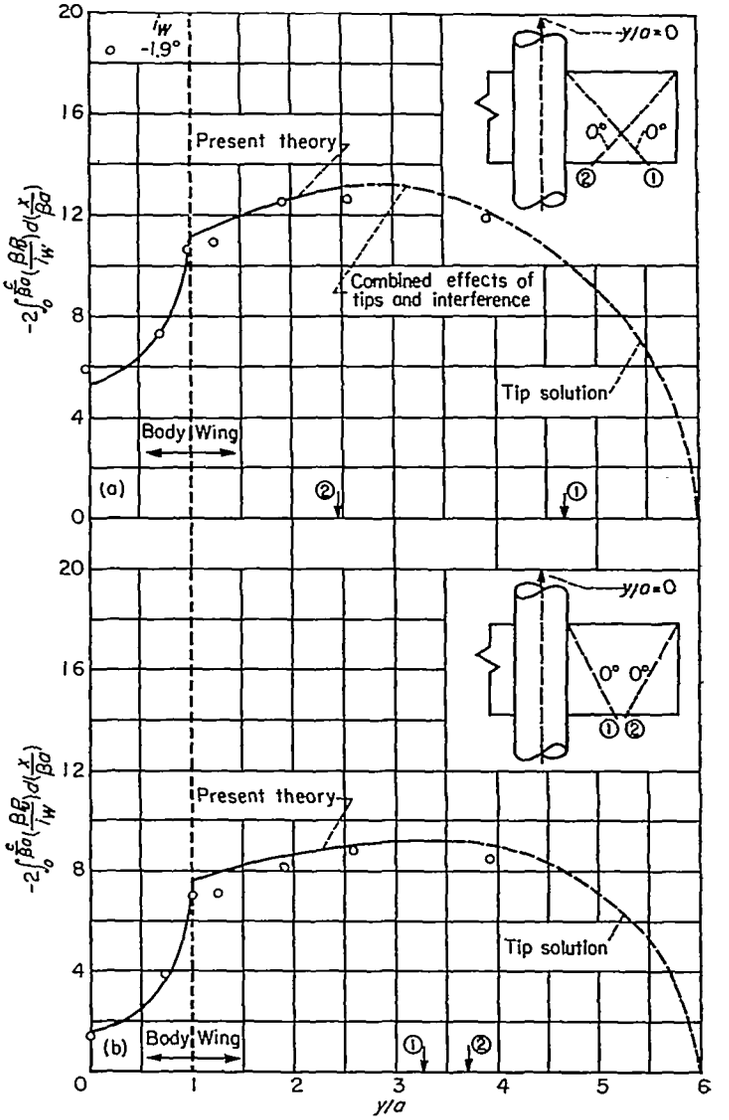

(a) $M=1.48$
(b) $M=2.00$

FIGURE 36.—Span load distributions due to wing incidence; $R=1.5\times10^6$.

Mach numbers 1.48 and 2.00. From this figure it appears that either the theory of Morikawa or the present theory can be used to predict the pressure distribution in the juncture of a wing-body combination. Ferrari's theory predicts values that are somewhat low at the leading edge of the wing, but it appears that if numerical results were available beyond $x/\beta a=0.7$, they would lie within the experimental range. For a more complete comparison of the theories of Ferrari and Nielsen, see references 9 and 23. Except for the present theory, no numerical results for the pressure distribution on the body were available for comparison.

CONCLUSIONS

A theory of wing-body interference for supersonic speeds has been developed. The theory was applied to the calculation of the separate effects of body angle of attack and wing incidence on the pressure distributions acting on a rectangular wing and body combination. On the basis of comparison between the theoretical predictions and experimental

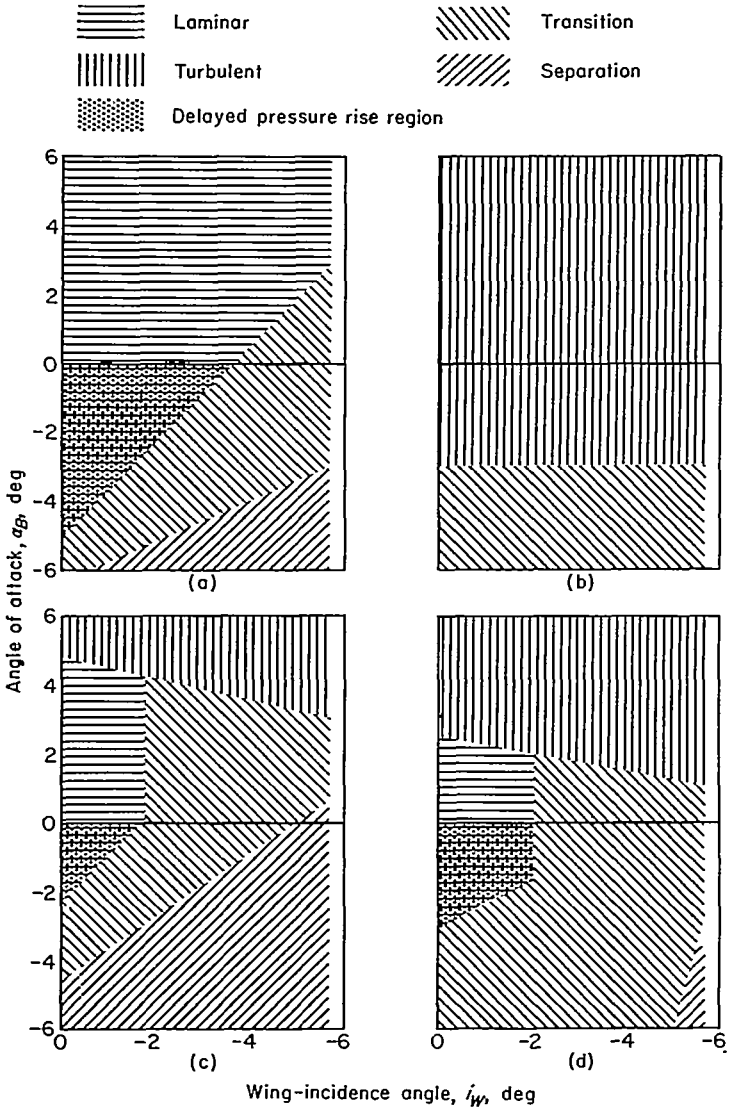

(a) $M=1.48$, $R=0.6\times10^6$ (b) $M=1.48$, $R=1.5\times10^6$
(c) $M=2.00$, $R=0.6\times10^6$ (d) $M=2.00$, $R=1.5\times10^6$

FIGURE 37.—Boundary-layer condition on top meridian of body at point of intersection with Mach helix from wing.

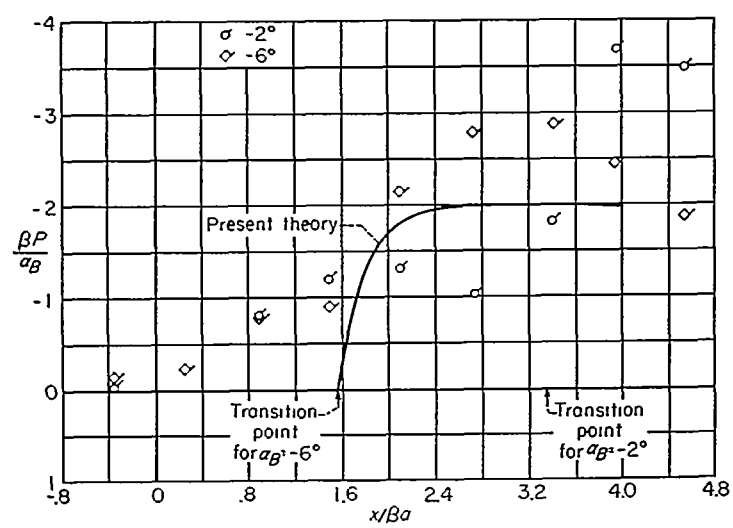

FIGURE 38.—Effect of transition position on pressure distribution on top meridian of body; $M=1.48$, $R=0.6\times10^6$, and $i_W=0°$.

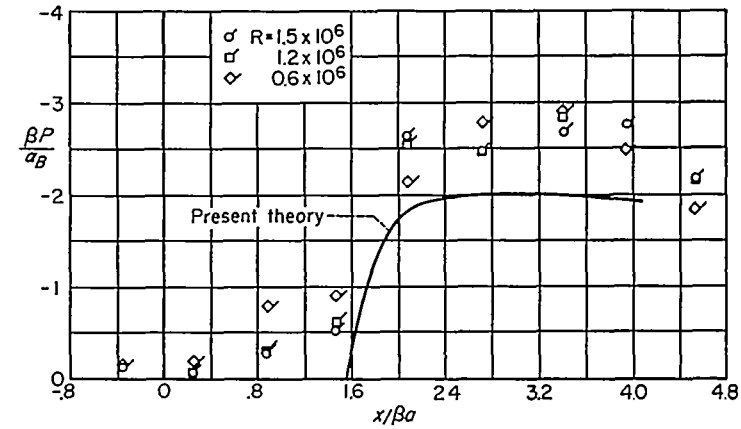

FIGURE 39.—Effect of Reynolds number on pressure distribution on top meridian of body; $M=1.48$, $\alpha_B=-6°$, and $i_W=0°$.

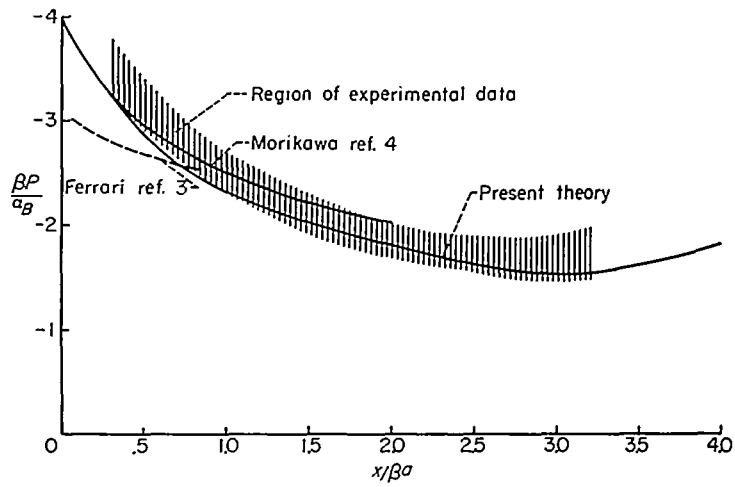

FIGURE 40.—Comparison among several theoretical calculations of pressures in the wing-body juncture of the combination; angle-of-attack case.

measurements, the following conclusions are drawn:

1. The present theory predicts the pressure distributions due to wing incidence about 5 percent high for angles up to 2°. However, the pressure distribution due to angle of attack is predicted about 5 percent low for $M=1.48$ and about 10 percent low at $M=2.00$ for angles between $+2°$ and $-2°$.

2. Nonlinear effects due to angle of attack and wing-incidence angle are large. On the wing the difference from linear theory due to nonlinear effects of angle can be predicted by shock-expansion theory, except near the wing-body juncture for the angle-of-attack case.

3. Span loading was shown to be predicted within ±10 percent for both the body and the wing. The predicted span loadings are high for the wing-incidence case and low for the angle-of-attack case.

4. For the angle-of-attack case, the pressure coefficients on the wing are experimentally about 5 percent higher for $M=2.00$ than for $M=1.48$, when reduced to a form that is theoretically independent of Mach number. Otherwise Mach number has no important effect.

5. Viscous effects are important only on the body where the shock wave from the wing causes large boundary-layer and shock-wave interactions for some angle conditions.

AMES AERONAUTICAL LABORATORY
NATIONAL ADVISORY COMMITTEE FOR AERONAUTICS
MOFFETT FIELD, CALIF., *Jan. 4, 1954*

APPENDIX A

DECOMPOSITION OF BOUNDARY CONDITIONS OF WING-BODY COMBINATION

A detailed analysis of the boundary conditions for a wing-body combination is now carried out for the following conditions:

1. The wing is a flat plate in the $z=0$ plane.
2. The body is an infinite cylinder, the $r=1$ cylinder.
3. The leading edges of the wing are supersonic.
4. The Mach number is $\sqrt{2}$.

Consider a wing-body combination corresponding to figure 4 (a) and shown in greater detail in figure 41 (a). The potentials for the flow must satisfy several conditions:

1. It must be a solution of the wave equation.
2. It must produce no flow normal to solid boundaries.
3. It must produce no upstream-moving disturbances.[8]

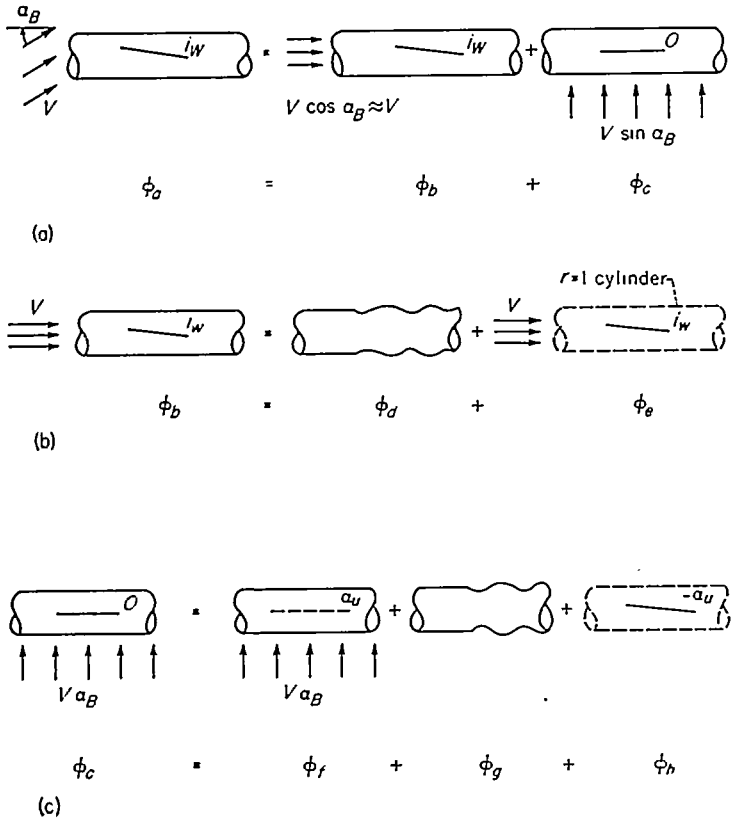

(a) Parallel and crossflow.
(b) Parallel flow.
(c) Crossflow

FIGURE 41.—Decomposition of boundary conditions.

If φ_a is the potential for the complete flow about the wing-body combination, then the boundary condition on the wing is

$$\frac{\partial\varphi_a}{\partial z}=-i_W V; \quad z=0 \tag{A1}$$

and on the body

$$\frac{\partial\varphi_a}{\partial r}=0; \quad r=1 \tag{A2}$$

The first step in the decomposition is to break φ_a into a potential due to flow along the x axis and one along the z axis in accordance with the superposition principle

Potential	φ_a	$=$	φ_b	$+$	φ_c
$\left(\frac{\partial\varphi}{\partial x}\right)_\infty$:	$V\cos\alpha_B$	$=V\cos\alpha_B+$	0		
$\left(\frac{\partial\varphi}{\partial z}\right)_\infty$:	$V\sin\alpha_B$	$=$	0	$+V\sin\alpha_B$	
$\left(\frac{\partial\varphi}{\partial z}\right)_{z=0^+}$ on wing:	$-i_W V$	$=$	$-i_W V+$	0	
$\left(\frac{\partial\varphi}{\partial r}\right)_{r=1}$ on body:	0	$=$	0	$+$	0

The flow conditions at infinity and the prescribed normal velocities at the combination surface also obey the superposition principle.

The next steps in the decomposition are to resolve φ_b and φ_c into potentials that can easily be computed. The decomposition of φ_b into wing-alone and body-alone problems is illustrated in figure 41 (b).

Potential:	φ_b	$=$	φ_d	$+$	φ_e
$\left(\frac{\partial\varphi}{\partial x}\right)_\infty$:	V	$=$	0	$+$	V
$\left(\frac{\partial\varphi}{\partial z}\right)_\infty$:	0	$=$	0	$+$	0
$\left(\frac{\partial\varphi}{\partial z}\right)_{z=0^+}$ on wing:	$-i_W V=$		0	$-$	$i_W V$
$\left(\frac{\partial\varphi}{\partial r}\right)_{r=1}$ on body:	0	$=\sum_{n=0}^{\infty} f_{2n}(x)\cos 2n\theta-$		$\sum_{n=0}^{\infty} f_{2n}(x)\cos 2n\theta$	

The potential φ_e due to the wing alone at incidence i_W produces a velocity field normal to the $r=1$ surface to be occupied by the body. The normal velocity field is decomposed into a Fourier series. Since the wing leading edges are supersonic, we can consider the flow above the $z=0$ plane alone. To preserve the wing-alone boundary condition when φ_d is added, we must confine ourselves to cosine terms, and, because of a vertical plane of symmetry, we must retain only cosine terms of even multiples of θ in the Fourier series. To counteract the distortion of the $r=1$ surface due to the wing alone, a body with opposite distortion is added in the form of φ_d.

[8] Since the surfaces on which the boundary conditions are given are parallel to the x axis, it is necessary to have this condition in order to differentiate upstream from downstream.

The decomposition of φ_c into three components is convenient; a component φ_f associated with cylindrical crossflow, a component φ_g due to a distorted body alone, and a component φ_h due to a twisted wing alone.

Potential:	φ_c	$=$	φ_f	$+$ φ_g	$+$	φ_h
$\left(\frac{\partial\varphi}{\partial x}\right)_\infty$:	0	$=$	0	$+$ 0	$+$	0
$\left(\frac{\partial\varphi}{\partial z}\right)_\infty$:	$\alpha_B V$	$=$	$\alpha_B V$	$+$ 0	$+$	0
$\left(\frac{\partial\varphi}{\partial z}\right)_{z=0^+}$ on wing	0	$=\alpha_B V\left(1+\frac{1}{y^2}\right)+$		0	$-$	$V\alpha_B\left(1+\frac{1}{y^2}\right)$
$\left(\frac{\partial\varphi}{\partial r}\right)_{r=1}$ on cylinder:	0	$=$	0	$+\sum_{n=0}^{\infty} f_{2n}(x)\cos 2n\theta$	$-$	$\sum_{n=0}^{\infty} f_{2n}(x)\cos 2n\theta$

The crossflow associated with φ_f causes an upwash distribution in the $z=0$ plane which requires an equal and opposite twisted wing to counteract it. Again the $r=1$ surface is distorted by the wing-alone flow field, and a cylinder with opposite distortion is introduced in the form of φ_g to counteract the distortion.

Two convenient cases in the wing-body interference problem are differentiated; the wing-incidence case in which $\alpha_B=0$ but $i_W\neq 0$ and the angle-of-attack case in which $i_W=0$ but $\alpha_B\neq 0$. The wing-incidence case is represented by φ_b and the angle-of-attack case by φ_c.

APPENDIX B

ASYMPTOTIC SPAN LOADING FOR FIRST HARMONIC; WING-INCIDENCE CASE

The span loading for the first harmonic as given by equation (57) is

$$\int_0^{\frac{x}{\beta a}}\left(\frac{\beta P_L}{i_W}-\frac{\beta P_U}{i_W}\right)d\left(\frac{x}{\beta a}\right) \tag{B1}$$

Let us take $a=1$, $\beta=1$, and $P_U=-P_L=P_o$; then the span loading is

$$-2\int_0^x\left(\frac{P_o}{i_W}\right)dx=\frac{4}{Vi_W}\int_0^x\frac{\partial\varphi_o}{\partial x}dx=\frac{4\varphi_o}{Vi_W} \tag{B2}$$

The method of calculating the asymptotic formula for the span loading is first to expand the Laplace transform in a series about the origin and then to take the inverse transform term by term.

From equation (17)

$$L\left[-2\int_0^x\left(\frac{P_o}{i_W}\right)dx\right]=\left[\frac{4F_o(s)}{Vi_W}\right]\left[\frac{K_o(sr)}{sK_o'(s)}\right] \tag{B3}$$

It is now necessary to find the series about the origin for the two parts of the transform of equation (B3).

From equation (47) there is obtained

$$F_o(s)=L[f_o(x)]=L\left(\frac{2}{\pi}\int_0^{\sin^{-1}x} i_W V\sin\theta\,d\theta\right) \tag{B4}$$

$$F_o(s)=\frac{2i_W V}{\pi}\int_0^\infty e^{-sx}dx\int_0^{\sin^{-1}x}\sin\theta\,d\theta$$

$$=\frac{2i_W V}{\pi}\int_0^{\pi/2}\sin\theta\,d\theta\int_{\sin\theta}^\infty e^{-sx}dx \tag{B5}$$

$$F_o(s)=\frac{i_W V}{\pi s}\left[\int_0^\pi\sin\theta\cos(is\sin\theta)\,d\theta+i\int_0^\pi\sin\theta\sin(is\sin\theta)\,d\theta\right] \tag{B6}$$

These integrals are given in terms of Anger and Weber functions as given on page 310 of reference 24.

$$\int_0^\pi\sin\theta\cos(is\sin\theta)\,d\theta=\pi E_1(is) \quad \text{(Weber function)}$$

$$\int_0^\pi\sin\theta\sin(is\sin\theta)\,d\theta=\pi J_1(is) \quad \text{(Anger function)}$$

The value of $F_o(s)$ is then

$$F_o(s)=\frac{i_W V}{s}\left[E_1(is)+iJ_1(is)\right] \tag{B7}$$

For small values of s the Anger and Weber functions have the expansion

$$\left.\begin{aligned} E_1(is)&\approx\frac{2}{\pi}\left[1+0(is)^2\right]\\ J_1(is)&\approx\frac{1}{2}\left[is+0(is)^3\right]\end{aligned}\right\} \tag{B8}$$

so that

$$F_o(s)\approx\frac{i_W V}{s}\left[\frac{2}{\pi}-\frac{s}{2}+0(s^2)\right] \tag{B9}$$

The ratio of Bessel functions given in equation (B3) has an expansion around the origin which is a doubly infinite series of products of powers of s and $\log s$.

$$K_o(sr)\approx-(\gamma+\log r/2)-\log s+0(s^2)+0(s^2\log s)$$

$$K_o'(s)\approx-\frac{1}{s}-\frac{s}{2}\log\left(\frac{s}{2}\right)+0(s)+0(s^3\log s)$$

$$\frac{K_o(sr)}{K_o'(s)}\approx s(\gamma+\log r/2)+s\log s+0(s^3)+0(s^3\log^2 s) \tag{B10}$$

From equations (B9) and (B10) we get

$$L\left[-2\int_o^x\left(\frac{P_o}{i_W}\right)dx\right]$$
$$=\left(\frac{4}{Vi_W}\right)\left(\frac{i_WV}{s^2}\right)\left[\frac{2}{\pi}-\frac{s}{2}+0(s^2)\right][s(\gamma+\log r/2)+$$
$$s\log s+0(s^3\log^2 s)]$$

so that

$$L\left[-2\int_o^x\left(\frac{P_o}{i_W}\right)dx\right]=\frac{8}{\pi}\left[\frac{(\gamma+\log r/2)}{s}+\right.$$
$$\left.\frac{\log s}{s}-\frac{\pi}{4}\log s+0(s\log^2 s)\right] \qquad \text{(B11)}$$

Taking the inverse transform with the help of reference 25, page 282, we obtain the desired result.

$$-2\int_o^x\left(\frac{P_o}{i_W}\right)dx\sim\frac{8}{\pi}\left[(\gamma+\log r/2)-\gamma-\log x+\frac{\pi}{4x}\right]$$
$$\sim\frac{8}{\pi}\left[\log\left(\frac{r}{2x}\right)+\frac{\pi}{4x}\right] \qquad \text{(B12)}$$

For any Mach number and body radius

$$-2\int_o^{\frac{x}{\beta a}}\left(\frac{\beta P_o}{i_W}\right)d\left(\frac{x}{\beta a}\right)\sim\frac{8}{\pi}\log\left(\frac{r/a}{2x/\beta a}\right)+\frac{2}{(x/\beta a)}\ \text{as}\ \frac{x}{\beta a}\to\infty \qquad \text{(B13)}$$

APPENDIX C

DETERMINATION OF WING-ALONE POTENTIAL FOR ANGLE-OF-ATTACK CASE

The first step in calculating the potential for the wing alone will be to set up a mathematical model. Since the exposed wing of the combination operates in the body upwash field which effectively twists the wing, the wing-alone model [9] is considered to be twisted in the manner predicted by Beskin upwash theory for $y\geq a$

$$\alpha_W=\alpha_B\left(1+\frac{a^2}{y^2}\right)=\alpha_B\left(1+\frac{1}{y^2}\right) \qquad \text{(C1)}$$

The concealed wing may be extended through the body region in any manner but, since equation (C1) gives $\alpha_W=2\alpha_B$ at both wing-body junctures, it is taken as a flat plate at angle of attack $2\alpha_B$ (see fig. 42).

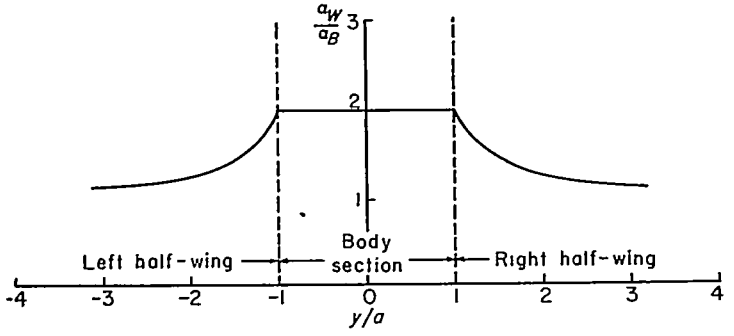

FIGURE 42.—Shape of wing alone with effective twist produced by body upwash field; angle-of-attack case.

The twisting of the wing is accomplished by superimposing a series of flat-plate wings upon a basic flat-plate wing at $\alpha_W=2\alpha_B$ (see fig. 43). Each of the superimposed wings is at an incremental angle of attack, and each successive wing terminates at a value of y greater than the previous one. As these incremental values of α become infinitesimally small, the resulting potential approaches that of a wing with the twist defined by equation (C1).

For the purposes of determining the wing-alone potential, the wing is considered to be composed of the three parts shown in figure 42: the right exposed half-wing, the left exposed half-wing, and the wing section inside the body. The perturbation velocity potential is determined for each of these wing sections and the results added together to obtain the potential for the entire wing alone. Thus,

$$\varphi_W=\varphi_{W_R}+\varphi_{W_L}+\varphi_{W_B} \qquad \text{(C2)}$$

Since the wing may be considered to be composed of an infinite number of flat, rectangular wings, the expression

$$\varphi(\alpha_W,y)=\frac{V\alpha_W}{\pi}\left(-x\cos^{-1}\frac{-y}{\sqrt{x^2-z^2}}-y\cosh^{-1}\frac{x}{\sqrt{y^2+z^2}}+\right.$$
$$\left.z\cos^{-1}\frac{-xy}{\sqrt{y^2+z^2}\sqrt{x^2-z^2}}\right) \qquad \text{(C3)}$$

from reference 6 for the velocity potential of a flat, rectangular wing will be used as the basic relation for the calculations. Equation (C3) gives the velocity potential at any point (x,y,z) due to a flat, rectangular wing at angle of attack α_W, terminating at $y=0$, and extending to ∞ along the positive y axis.[10]

Since the twisted wing was shown to be equivalent to a basic flat-plate wing at angle of attack $2\alpha_B$ plus an infinite number of modifying flat-plate wings (see fig. 43), the potential of the right half-wing may be written as

$$\varphi_{W_R}=\varphi(2\alpha_B,y-1)+\sum_1^N\varphi(\Delta\alpha_i,y-\eta_i) \qquad \text{(C4)}$$

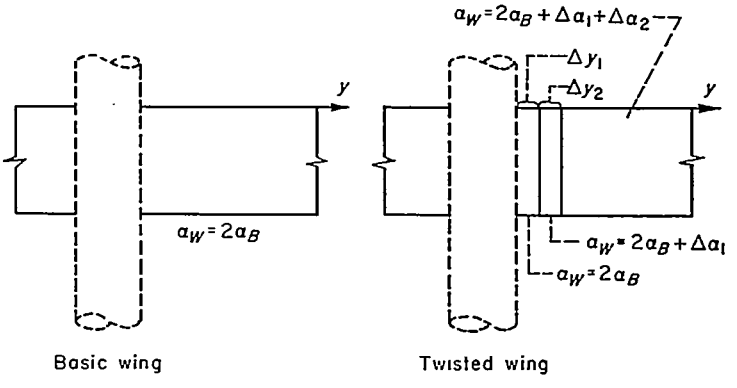

FIGURE 43.—Formation of twisted wing by superposition of infinite number of flat plates.

[9] Both a and β are taken as unity.

[10] The top and bottom wing surfaces are still considered independent.

The first term on the right in equation (C4) is the potential due to the basic exposed half-wing which terminates at the wing-body juncture, $y=1$, and is at angle of attack $2\alpha_B$. The second term is the potential of the N modifying wings each at angle of attack $\Delta\alpha_t$ and terminating at $y=\eta_t$ where $1<\eta_t\leq\infty$. Since equation (C3) is homogeneous with respect to α, equation (C4) may be written

$$\varphi_{W_R}=\varphi(2\alpha_B,y-1)+\sum_1^N \varphi(1,y-\eta_t)\Delta\alpha_t \tag{C5}$$

From equation (C1)

$$d\alpha_W=-\frac{2\alpha_B}{y^3}\,dy \tag{C6}$$

Therefore,

$$\varphi_{W_R}=\varphi(2\alpha_B,y-1)-2\alpha_B\int_1^{\eta_u}\varphi(1,y-\eta)\,\frac{d\eta}{\eta^3} \tag{C7}$$

where the limits of integration are determined by the range of y on the wing included in the fore Mach cone originating from the point for which φ_{W_R} is being determined. From figure 44 it is apparent from the equation of the fore Mach

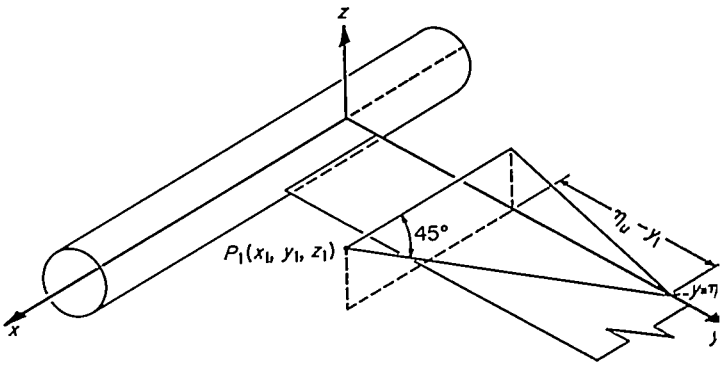

FIGURE 44.—Upper value of y included in the fore Mach cone emanating from P_1; $\beta=1$.

cone emanating from the arbitrary point P_1 for $\beta=1$ that

$$x_1^2=z_1^2+(\eta_u-y_1)^2$$

Therefore, the upper limit of integration is

$$\eta_u=y_1+\sqrt{x_1^2-z_1^2} \tag{C8}$$

The lower limit of integration is at the wing-body juncture $y=1$. From equations (C3), (C7), and (C8),

$$\varphi_{W_R}=R.P.\left\{\frac{2V\alpha_B}{\pi}\left[-x\cos^{-1}\frac{-(y-1)}{\sqrt{x^2-z^2}}-(y-1)\cosh^{-1}\frac{x}{\sqrt{(y-1)^2+z^2}}+z\cos^{-1}\frac{-x(y-1)}{\sqrt{(y-1)^2+z^2}\sqrt{x^2-z^2}}\right]-\right.$$
$$\left.\frac{2V\alpha_B}{\pi}\int_1^{y+\sqrt{x^2-z^2}}\left[-x\cos^{-1}\frac{-(y-\eta)}{\sqrt{x^2-z^2}}-(y-\eta)\cosh^{-1}\frac{x}{\sqrt{(y-\eta)^2+z^2}}+z\cos^{-1}\frac{-x(y-\eta)}{\sqrt{(y-\eta)^2+z^2}\sqrt{x^2-z^2}}\right]\frac{d\eta}{\eta^3}\right\} \tag{C9}$$

Carrying out the integration and combining terms gives

$$\varphi_{W_R}=R.P.\left\{\frac{V\alpha_B}{\pi}\left[-x\cos^{-1}\frac{-(y-1)}{\sqrt{x^2-z^2}}+\right.\right.$$
$$\left(\frac{y}{y^2+z^2}-y\right)\cosh^{-1}\frac{x}{\sqrt{(y-1)^2+z^2}}-$$
$$\frac{xy}{(y^2+z^2)\sqrt{x^2-y^2-z^2}}\cosh^{-1}\frac{x^2-y(y-1)-z^2}{\sqrt{x^2-z^2}}+$$
$$\left.\left.\left(z+\frac{z}{y^2+z^2}\right)\cos^{-1}\frac{-x(y-1)}{\sqrt{(y-1)^2+z^2}\sqrt{x^2-z^2}}\right]\right\} \tag{C10}$$

Equation (C10) gives the potential due to the exposed right half-wing. To this must be added the potentials due to the other two wing sections. The potential due to the section of the wing in the body region is simply the difference between the potentials of two flat wings at $\alpha_W=2\alpha_B$. One of these wings terminates at the wing-body juncture at $y=-1$, figure 42, and extends (through the body) indefinitely in the positive direction. The other wing terminates at the other wing-body juncture, $y=+1$, and also extends indefinitely in the positive y direction. The difference between the potentials of these two wings is the potential of the wing section in the body

$$\varphi_{W_B}=\varphi(2\alpha_B,y+1)-\varphi(2\alpha_B,y-1) \tag{C11}$$

The expression for φ (α_W, y) is given by equation (C3). Since the model is symmetrical about the vertical $y=0$ plane, the potential for the other half-wing is simply obtained by replacing y by $-y$ in equation (C10).

$$\varphi_{W_L}=\varphi_{W_R}(x,-y,z) \tag{C12}$$

Combining equations (C10), (C11), and (C12) gives the potential due to the entire wing alone.

$$\varphi_W=R.P.\frac{V\alpha_B}{\pi}\left\{x\left(\cos^{-1}\frac{1-y}{\sqrt{x^2-z^2}}+\cos^{-1}\frac{1+y}{\sqrt{x^2-z^2}}\right)+\right.$$
$$\left(\frac{y}{y^2+z^2}+y-2\right)\cosh^{-1}\frac{x}{\sqrt{(y-1)^2+z^2}}-$$
$$\left(\frac{y}{y^2+z^2}+y+2\right)\cosh^{-1}\frac{x}{\sqrt{(y+1)^2+z^2}}+\left(\frac{z}{y^2+z^2}-z\right)$$
$$\left[\cos^{-1}\frac{-x(y-1)}{\sqrt{(y-1)^2+z^2}\sqrt{x^2-z^2}}+\cos^{-1}\frac{x(y+1)}{\sqrt{(y+1)^2+z^2}\sqrt{x^2-z^2}}\right]+$$
$$\frac{xy}{(y^2+z^2)\sqrt{x^2-y^2-z^2}}\left[\cosh^{-1}\frac{x^2-y(y+1)-z^2}{\sqrt{x^2-z^2}}-\right.$$
$$\left.\left.\cosh^{-1}\frac{x^2-y(y-1)-z^2}{\sqrt{x^2-z^2}}\right]+2\pi(z-x)\right\} \tag{C13}$$

Investigation of φ_W as given by equation (C13) reveals that there are three regions on the body in which the real part of this expression assumes different forms. A fourth region, region IV, is entirely on the wing and is, therefore, not necessary for determining the normal velocity distribution on the body. These regions are determined by three

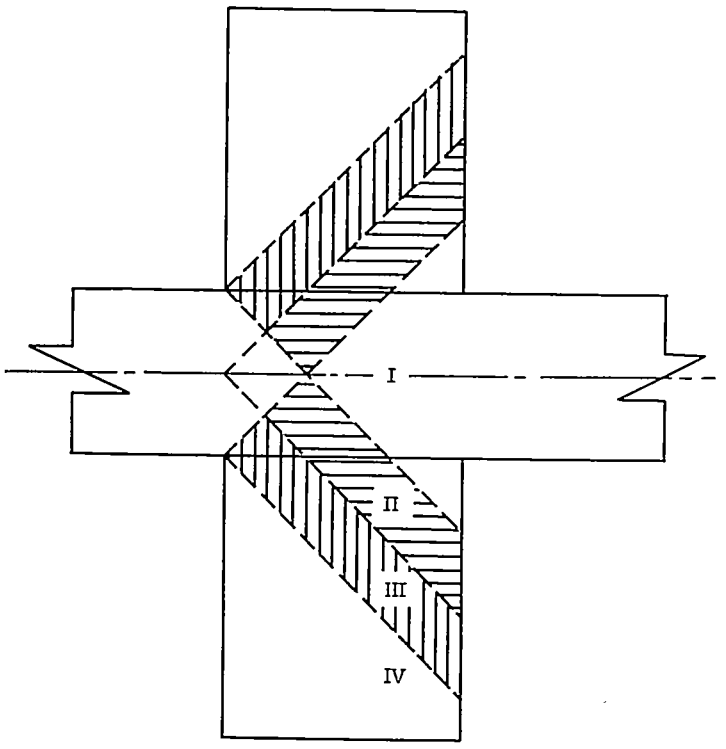

FIGURE 45.—Intersection of characteristic Mach cones with $z=0$ plane showing corresponding regions.

characteristic Mach cones. One of the Mach cones originates on the body axis at $x=0$, and the other two originate at the leading edges of the two wing-body junctures (see fig. 45). The expressions for the real part of φ_W in the three regions on the body are:

Region I:

$$\varphi_W=-\frac{V\alpha_B}{\pi}\left\{-x\left[\cos^{-1}\frac{-(y-1)}{\sqrt{x^2-z^2}}+\cos^{-1}\frac{(y+1)}{\sqrt{x^2-z^2}}\right]-\left(\frac{y}{y^2+z^2}+y-2\right)\cosh^{-1}\frac{x}{\sqrt{(y-1)^2+z^2}}+\left(\frac{y}{y^2+z^2}+y+2\right)\cosh^{-1}\frac{x}{\sqrt{(y+1)^2+z^2}}+\left(z-\frac{z}{y^2+z^2}\right)\left[\cos^{-1}\frac{-x(y-1)}{\sqrt{(y-1)^2+z^2}\sqrt{x^2-z^2}}+\cos^{-1}\frac{x(y+1)}{\sqrt{(y+1)^2+z^2}\sqrt{x^2-z^2}}\right]+\frac{xy}{(y^2+z^2)\sqrt{x^2-y^2-z^2}}\left[\cosh^{-1}\frac{x^2-z^2-y(y-1)}{\sqrt{x^2-z^2}}-\cosh^{-1}\frac{x^2-z^2-y(y+1)}{\sqrt{x^2-z^2}}\right]-2(z-x)\pi\right\} \quad \text{(C14)}$$

Region II:

$$\varphi_W=-\frac{V\alpha_B}{\pi}\left[-x\cos^{-1}\frac{-(y-1)}{\sqrt{x^2-z^2}}-\left(\frac{y}{y^2+z^2}+y-2\right)\cosh^{-1}\frac{x}{\sqrt{(y-1)^2+z^2}}-\left(\frac{z}{y^2+z^2}-z\right)\cos^{-1}\frac{-x(y-1)}{\sqrt{(y-1)^2+z^2}\sqrt{x^2-z^2}}+\frac{xy}{(y^2+z^2)\sqrt{x^2-y^2-z^2}}\cosh^{-1}\frac{x^2-z^2-y(y-1)}{\sqrt{x^2-z^2}}-2(z-x)\pi\right] \quad \text{(C15)}$$

Region III:

$$\varphi_W=-\frac{V\alpha_B}{\pi}\left[-x\cos^{-1}\frac{-(y-1)}{\sqrt{x^2-z^2}}-\left(\frac{y}{y^2+z^2}+y-2\right)\cosh^{-1}\frac{x}{\sqrt{(y-1)^2+z^2}}-\left(\frac{z}{y^2+z^2}-z\right)\cos^{-1}\frac{-x(y-1)}{\sqrt{(y-1)^2+z^2}\sqrt{x^2-z^2}}+\frac{xy}{(y^2+z^2)\sqrt{y^2+z^2-x^2}}\cos^{-1}\frac{x^2-z^2-y(y-1)}{\sqrt{x^2-z^2}}-2(z-x)\pi\right] \quad \text{(C16)}$$

REFERENCES

1. Spreiter, John R.: The Aerodynamic Forces on Slender Plane- and Cruciform-Wing and Body Combinations. NACA Rep. 962, 1950. (Formerly NACA TN's 1662 and 1897.)
2. Browne, S. H., Friedman, L., and Hodes, I.: A Wing-Body Problem in a Supersonic Conical Flow. Jour. Aero. Sci., vol. 15, no. 8, Aug. 1948, pp. 443–452.
3. Ferrari, Carlo: Interference Between Wing and Body at Supersonic Speeds—Theory and Numerical Application. Jour. Aero. Sci., vol. 15, no. 6, June 1948, pp. 317–336.
4. Morikawa, George K.: The Wing-Body Problem for Linearized Supersonic Flow. Calif. Inst. of Tech. Doctoral Thesis, 1949. GALCIT, Jet Propulsion Lab. PR4–116.
5. Bolton-Shaw, B. W.: Wing-Body Interference at Supersonic Speeds—Rectangular Wing at Incidence on a Body at Zero Incidence. English Electric Co. Rep. LA. t. 039.
6. Nielsen, Jack N., and Matteson, Frederick H.: Calculative Method for Estimating the Interference Pressure Field at Zero Lift on a Symmetrical Swept-Back Wing Mounted on a Circular Cylindrical Body. NACA RM A9E19, 1949.
7. Nielsen, Jack N.: Supersonic Wing-Body Interference. Calif. Inst. of Tech. Doctoral Thesis, 1951.
8. von Kármán, Theodore, and Moore, Norton B.: Resistance of Slender Bodies Moving With Supersonic Velocities, With Special Reference to Projectiles. Amer. Soc. Mech. Engrs., vol. 54, Dec. 1932, pp. 303–310.
9. Phinney, R. E.: Wing-Body Interference. Progress Report No. 4. University of Michigan, Eng. Res. Inst., Project M937, April 1952.
10. Nielsen, Jack N., and Pitts, William C.: Wing-Body Interference at Supersonic Speeds With an Application to Combinations With Rectangular Wings. NACA TN 2677, 1952.
11. Bailey, H. E., and Phinney, R. E.: Wing-Body Interference. Final Report. Part I. Theoretical Investigation. University of Michigan, Eng. Res. Inst., 1937–1–F, Jan. 1954.
12. Bailey, H. E., and Phinney, R. E.: Wing-Body Interference. Final Report. Part II. Experimental Investigation of Cylindrical Model. University of Michigan. Eng. Res. Inst., Feb. 1954.
13. Pitts, William C., Nielsen, Jack N., and Gionfriddo, Maurice P.: Comparison Between Theory and Experiment for Interference Pressure Field Between Wing and Body at Supersonic Speeds. NACA TN 3128, 1954.
14. Tsien, H.: Supersonic Flow Over an Inclined Body of Revolution. Jour. Aero. Sci., vol. 5, no. 12, 1938, pp. 480–483.
15. Lagerstrom, P. A., and Van Dyke, Milton D.: General Considerations About Planar and Nonplanar Lifting Systems. Douglas Aircraft Co., Rep. No. SM–13432, June 1949.
16. Ward, G. N.: The Approximate External and Internal Flow Past a Quasi-Cylindrical Tube Moving at Supersonic Speeds. Quart. Jour. Mech. and App. Math., vol. I, pt. 2, June 1948, pp. 225–245.
17. Fraenkel, L. E.: On the Operational Form of the Linearized Equation of Supersonic Flow. Jour. Aero. Sci., vol. 20, no. 9, 1953, Readers Forum, pp. 647–648.
18. Mersman, W. A.: Numerical Calculation of Certain Inverse Laplace Transforms. (Résumé) Vol. 2 of Proc. Intl. Cong. of Mathematicians, Amsterdam, 1954.
19. Lamb, Horace: Hydrodynamics. Sixth Ed., Dover Publications, 1945, p. 527.
20. Busemann, Adolf: Infinitesimal Conical Supersonic Flow. NACA TM 1100, 1947.
21. Alden, Henry L., and Schindel, Leon H.: The Calculation of Wing Lift and Moments in Nonuniform Supersonic Flows. Meteor Rep. No. 53, M. I. T., May 1950.
22. Cramer, R. H.: Interference Between Wing and Body at Supersonic Speeds. Part V—Phase I Wind-Tunnel Tests Correlated With the Linear Theory. Cornell Aero. Lab. Rep. No. CAL/CM–597, Dec. 1950.
23. Lawrence, H. R., and Flax, A. H.: Wing-Body Interference at Subsonic and Supersonic Speeds. Survey and New Developments. Paper presented at the Annual Summer Meeting of the I. A. S., Los Angeles, July 15–17, 1953.
24. Watson, G. N.: A Treatise on the Theory of Bessel Functions. Second Ed. 1944, MacMillan.
25. Carslaw, H. S., and Jaeger, J. C.: Operational Methods in Applied Mathematics. Second Edition 1947, Oxford University Press.

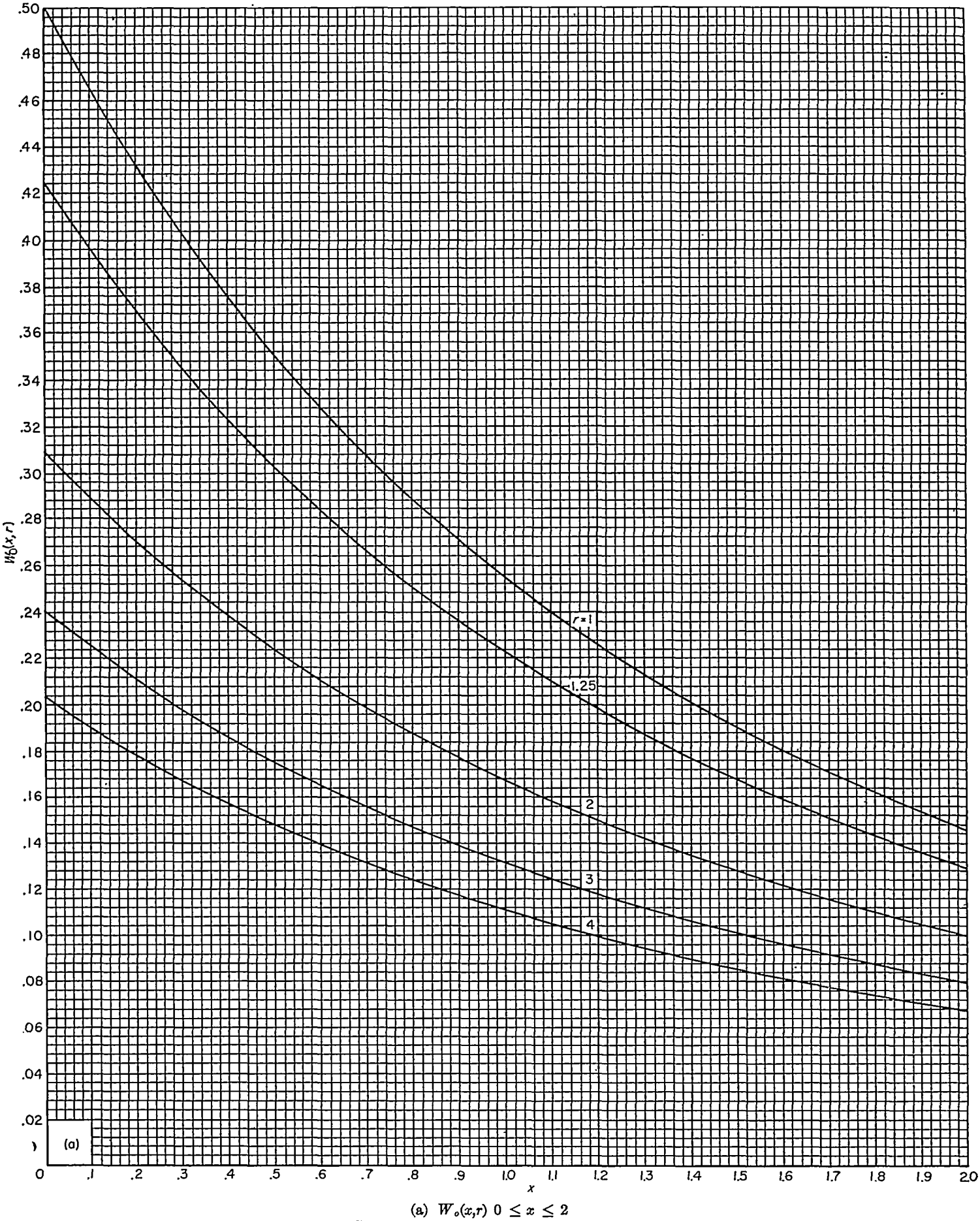

(a) $W_o(x,r)$ $0 \leq x \leq 2$

CHART 1.—Values of $W_{2n}(x,r)$ functions.

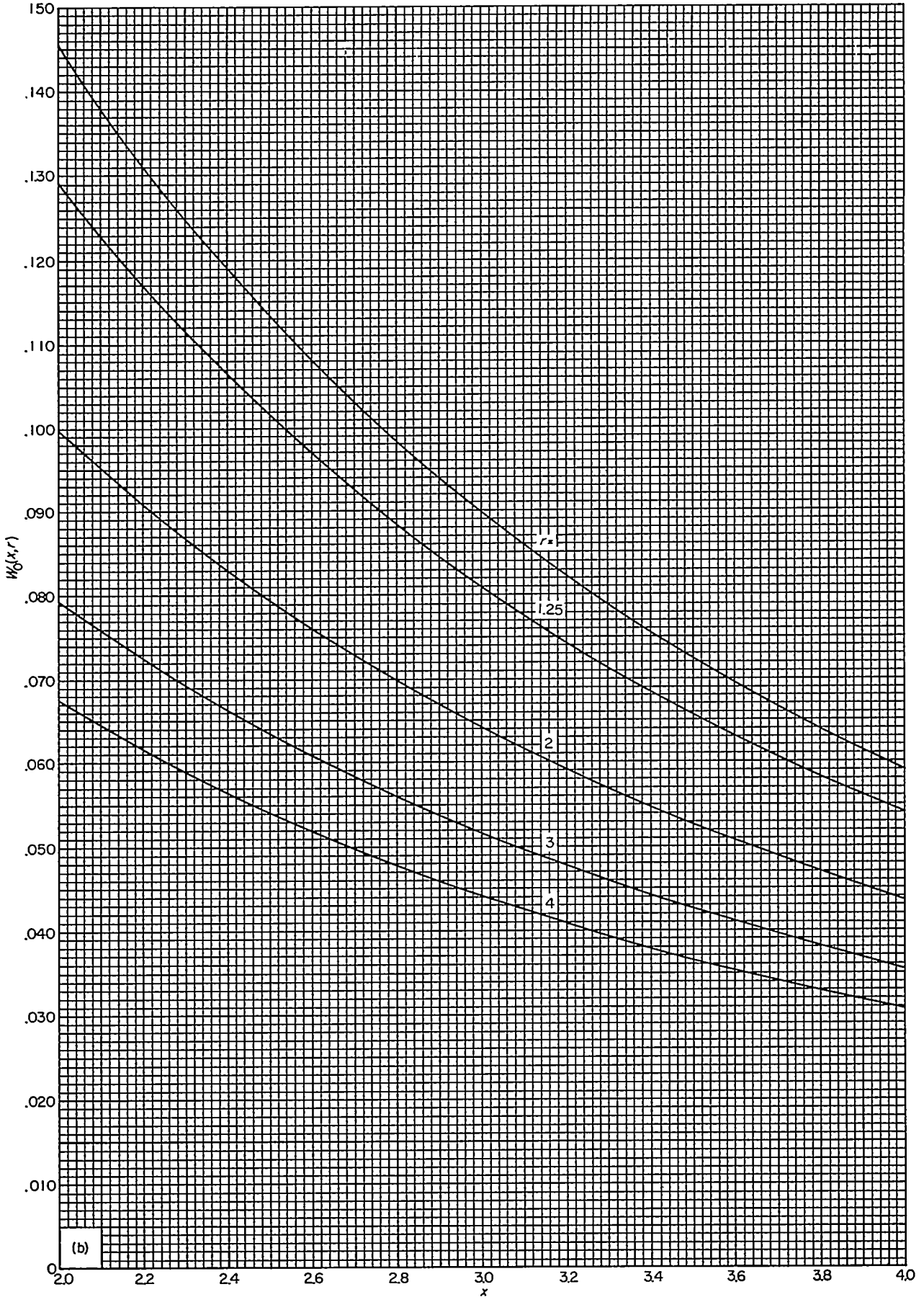

(b) $W_o(x,r)$ $2 \leq x \leq 4$

CHART 1.—Continued.

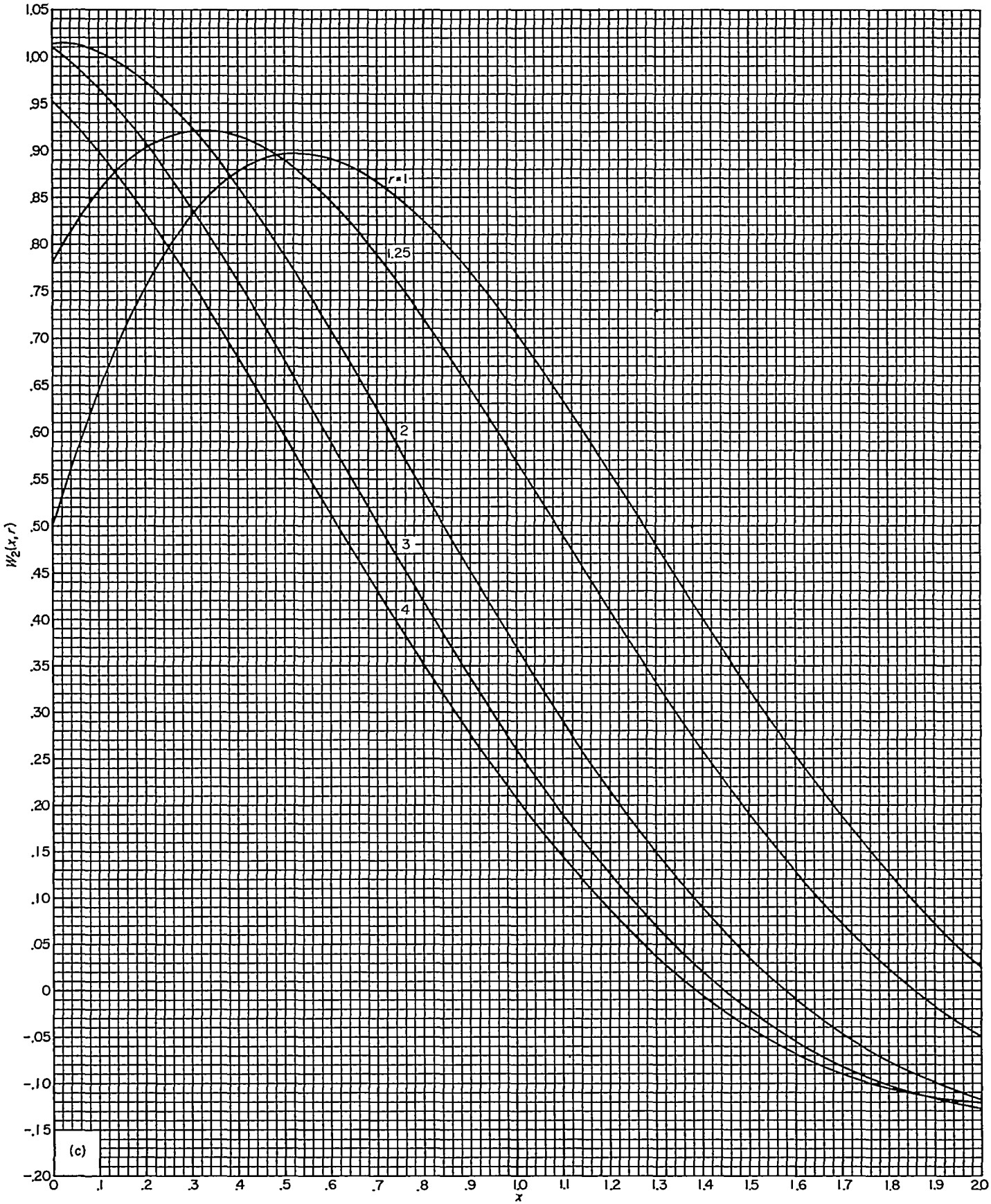

(c) $W_2(x,r)$ $0 \leq x \leq 2$

CHART 1.—Continued.

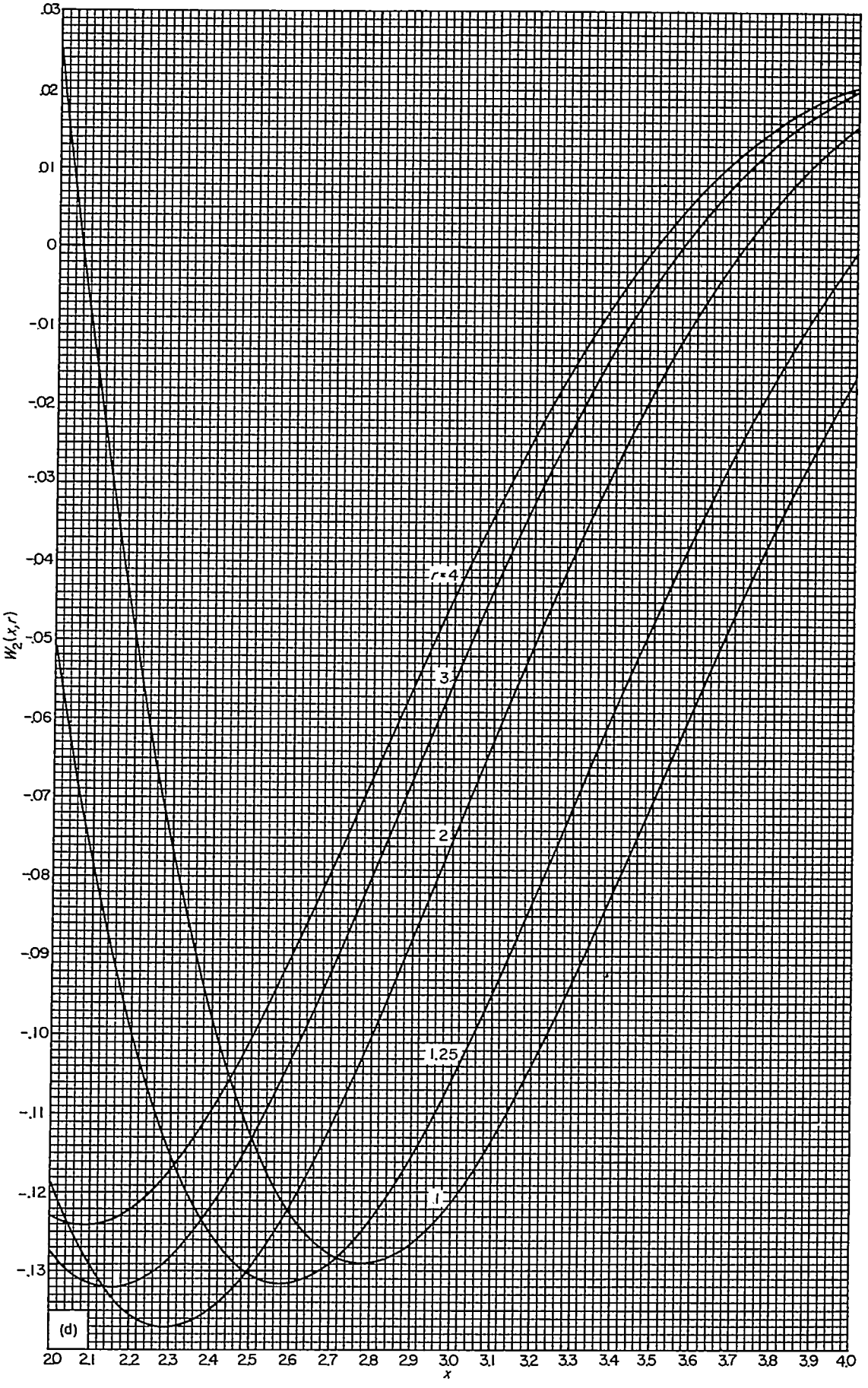

(d) $W_2(x,r)$ $2 \leq x \leq 4$

CHART 1.—Continued.

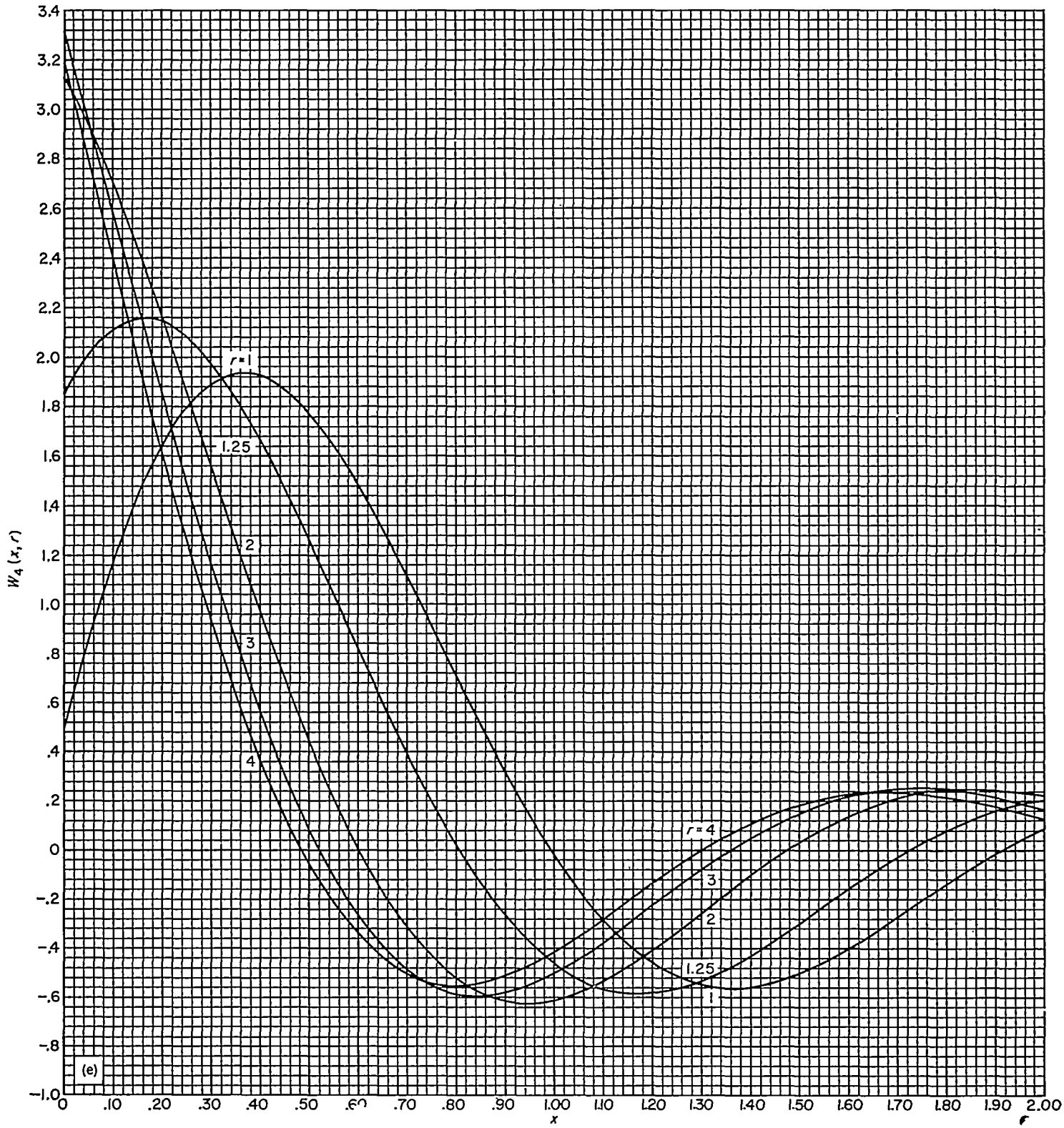

(e) $W_4(x,r)$ $0 \leq x \leq 2$

CHART 1.—Continued.

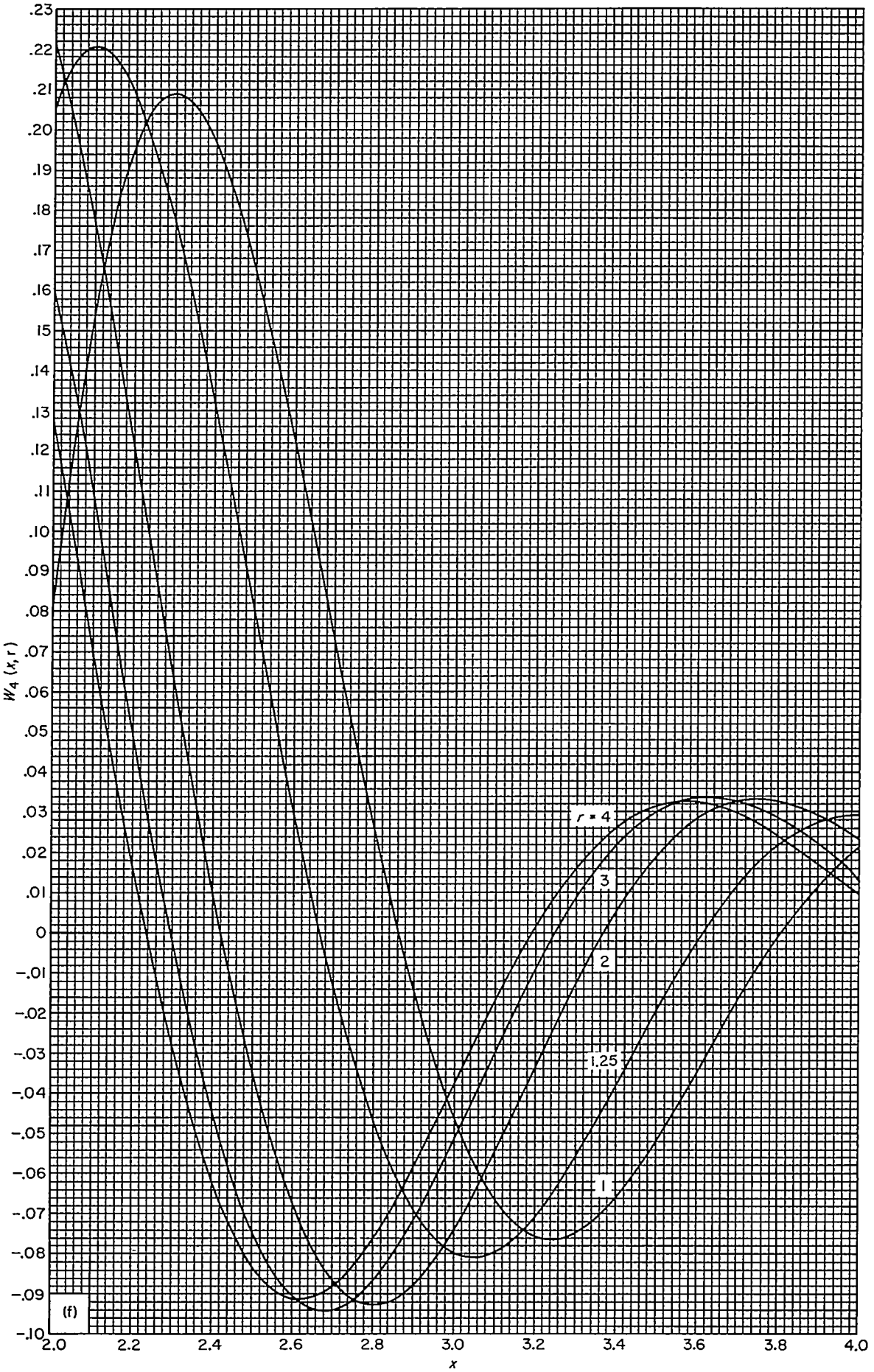

(f) $W_4(x,r)$ $2 \leq x \leq 4$

CHART 1.—Continued.

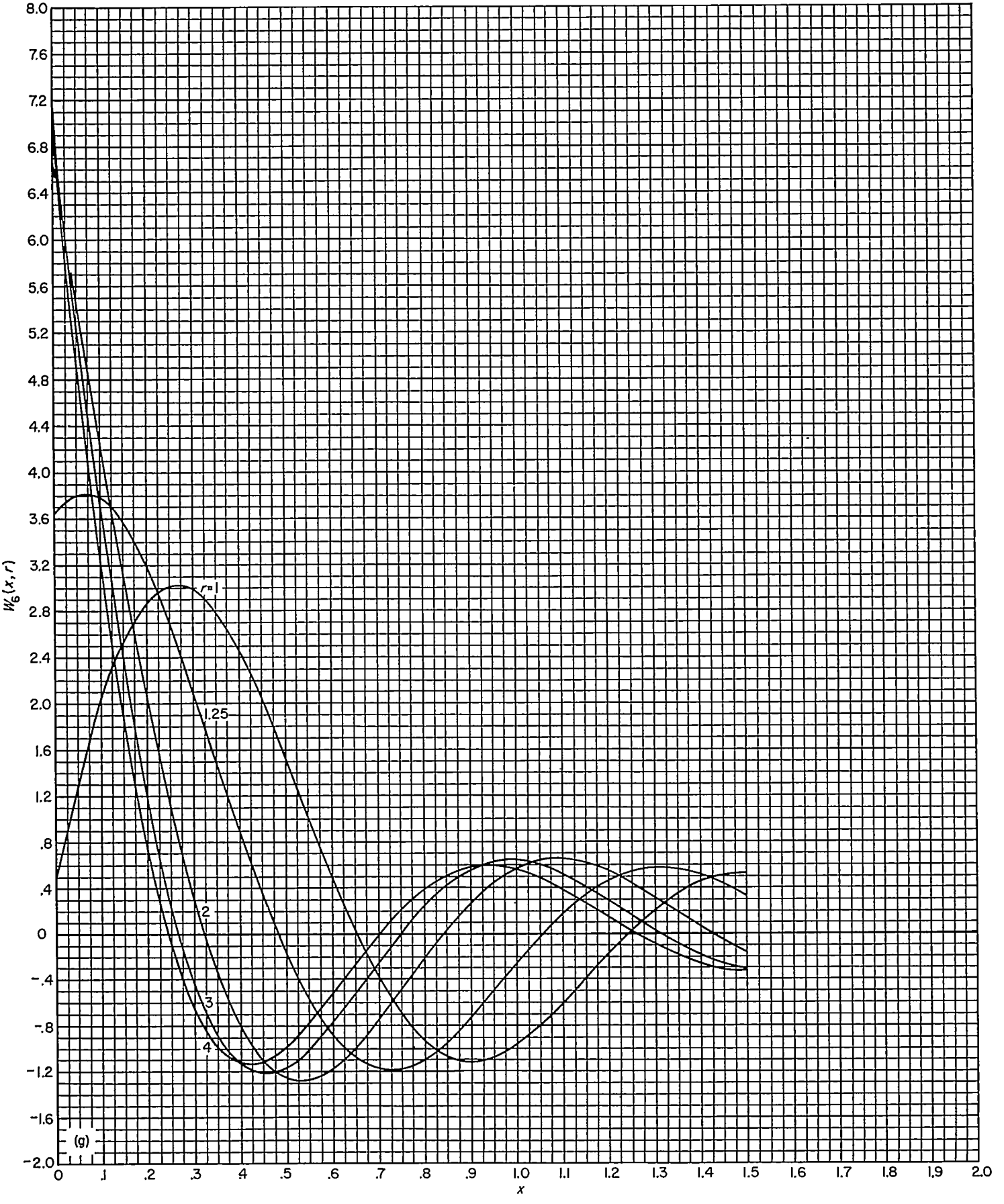

(g) $W_6(x,r)$ $0 \leq x \leq 1.5$

CHART 1.—Concluded.

TABLE I.—VALUES OF $M_{2n}(x)$

x	$M_0(x)$	$M_2(x)$	$M_4(x)$	$M_6(x)$
0	$-\infty$	$-\infty$	$-\infty$	$-\infty$
.05			−.531	−.716
.1	−1.321	−.787	.405	1.334
.15				1.155
.2	−.868	−.166	.902	.735
.25				.279
.3		.131	.831	−.119
.35				−.417
.40	−.538	.304	.560	−.595
.45				−.675
.50			.245	−.655
.6	−.378	.450	−.040	−.417
.7			−.253	−.070
.75				.095
.8	−.292	.457	−.386	.235
.85				.340
.9			−.434	.406
.95				.433
1.0	−.224	.392	−.412	.420
1.1			−.337	.306
1.2	−.180	.294	−.231	.123
1.3			−.115	−.062
1.4	−.147	.188	.000	−.197
1.5			.095	−.256
1.6	−.122	.088	.163	−.239
1.7			.204	−.162
1.8	−.102	.005	.211	−.062
1.9			.197	.036
2.0	−.086	−.058	.164	.105
2.1				.134
2.2	−.073	−.100	.069	.121
2.3			.020	.085
2.4	−.062	−.123	−.022	.036
2.5			−.053	−.013
2.6	−.053	−.126	−.073	−.053
2.7				−.063
2.8	−.045	−.119	−.080	−.059
2.9			−.071	−.042
3.0	−.038	−.103	−.060	−.019
3.1			−.038	.005
3.2	−.031	−.083	−.019	.022
3.3			−.002	.030
3.4	−.026	−.061	.011	.028
3.5			.021	.019
3.6	−.022	−.040	.027	.008
3.7			.027	−.002
3.8	−.018	−.022	.025	−.011
3.9			.022	−.014
4.0	−.016	−.007	.015	−.103

NOTE that $M_{2n}(x) \to -\frac{1}{\pi}\sqrt{\frac{2}{x}}$ as $x \to 0$.

TABLE II.—VELOCITY AMPLITUDE FUNCTIONS

x	Angle of attack case, $f_{2n}(x)$ functions						Wing-incidence case, $f_{2n}(x)$ functions			
	$\frac{f_0}{V\alpha_B}$	$\frac{f_2}{V\alpha_B}$	$\frac{f_4}{V\alpha_B}$	$\frac{f_6}{V\alpha_B}$	$\frac{f_8}{V\alpha_B}$	$\frac{f_{10}}{V\alpha_B}$	$\frac{f_0}{Vi_W}$	$\frac{f_2}{Vi_W}$	$\frac{f_4}{Vi_W}$	$\frac{f_6}{Vi_W}$
0	0	0	0	0	0	0	0	0	0	0
.02	.001	.003	.001	.003	.003	.004	.0001	.0003	.0003	.0003
.04	.003	.008	.004	.007	.005	.007	.0005	.0010	.0010	.0010
.06	.006	.012	.008	.011	.009	.012	.0011	.0023	.0023	.0022
.08	.008	.017	.013	.015	.013	.016	.0020	.0040	.0040	.0038
.10	.011	.022	.019	.020	.017	.020	.0032	.0063	.0061	.0058
.12	.014	.029	.026	.025	.022	.022	.0046	.0091	.0087	.0080
.14	.019	.037	.034	.031	.027	.024	.0063	.0123	.0116	.0104
.16	.024	.047	.043	.037	.033	.025	.0082	.0160	.0148	.0128
.18	.029	.057	.052	.044	.037	.024	.0104	.0201	.0181	.0151
.20	.032	.068	.062	.052	.040	.023	.0129	.0247	.0217	.0171
.22							.0156	.0297	.0253	.0187
.24	.050	.097	.083	.063	.038	.014	.0186	.0350	.0289	.0197
.26							.0219	.0408	.0324	.0201
.28	.068	.127	.103	.067	.026	−.007	.0255	.0469	.0356	.0196
.30	.079	.143	.112	.067	.017	−.022	.0293	.0533	.0395	.0181
.32	.089	.161	.120	.065	.007	−.041	.0335	.0600	.0412	.0155
.34							.0379	.0670	.0432	.0117
.36	.111	.199	.133	.051	−.023	−.080	.0427	.0742	.0445	.0065
.38							.0478	.0815	.0450	−.0001
.40	.136	.238	.140	.026	−.068	−.106	.0531	.0890	.0447	−.0081
.42	.151	.258	.139	.008	−.090	−.114	.0589	.0966	.0433	−.0177
.44							.0649	.1043	.0408	−.0282
.46							.0714	.1119	.0371	−.0410
.48	.196	.315	.126	−.065	−.146	−.121	.0781	.1195	.0320	−.0536
.50	.214	.333	.116	−.086	−.159	−.114	.0853	.1269	.0254	−.0679
.52							.0928	.1342	.0173	−.0829
.54	.299	.369	.088	−.145	−.178	−.082	.1008	.1411	.0074	−.0985
.56	.208	.388	.069	−.175	−.182	−.054	.1092	.1477	−.0041	−.1142
.58							.1180	.1539	−.0174	−.1297
.60	.308	.420	.016	−.236	−.176	.047	.1273	.1596	−.0326	−.1446
.62							.1371	.1646	−.0497	−.1583
.64	.353	.450	−.052	−.286	−.142	.119	.1475	.1688	−.0686	−.1703
.66		.461					.1584	.1722	−.0893	−.1808
.68							.1689	.1746	−.1118	−.1870
.70	.429	.476	−.181	−.322	−.012	.164	.1820	.1757	−.1359	−.1897
.72	.457	.478	−.232	−.323	.075	.163	.1948	.1755	−.1616	−.1898
.74							.2084	.1737	−.1886	−.1838
.76							.2229	.1701	−.2164	−.1739
.78							.2382	.1644	−.2451	−.1565
.80	.587	.456	−.452	−.212	.235	.027	.2546	.1562	−.2738	−.1350
.82							.2722	.1452	−.3021	−.1063
.84	.667	.411	−.552	−.109	.223	−.170	.2912	.1308	−.3292	−.0716
.86							.3118	.1125	−.3539	−.0312
.88							.3342	.0894	−.3751	.0136
.90	.812	.280	−.673	.178	.093	−.234	.3591	.0603	−.3908	.0609
.92							.3871	.0235	−.3983	.1075
.94							.4194	−.0237	−.3939	.1480
.96	1.013	.004	−.623	.397	−.263	.062	.4584	−.0865	−.3704	.1727
.98	1.121	−.250	−.510	.378	−.340	.225	.5098	−.1777	−.3121	.1605
1.00	1.375	−.669	−.053	−.025	−.0268	−.0144	.6366	−.4244	−.0849	−.0364
1.1	1.385	−.651	−.047	−.032	−.0289	−.0078	↓	↓	↓	↓
1.2	1.393	−.631	−.045	−.040	−.0230	−.0108				
1.3	1.402	−.613	−.045	−.045	−.0192	−.0118				
1.4	1.410	−.592	−.048	−.047	−.0156	−.0152				
1.5	1.415	−.572	−.055	−.045	−.0166	−.0146				
1.6	1.421	−.550	−.064	−.040	−.0199	−.0122				
1.7	1.424	−.527	−.075	−.035	−.0224	−.0115				
1.8	1.425	−.503	−.084	−.033	−.0206	−.0135				
1.9	1.424	−.479	−.088	−.036	−.0195	−.0127				
2.0	1.421	−.459	−.087	−.037	−.0203	−.0129				
2.4	1.384	−.434	−.085	−.036	−.0202	−.0129				
2.8	1.356	−.429	−.085	−.036	−.0202	−.0129				
3.2	1.337	−.427	−.085	−.036	−.0202	−.0129				
3.6	1.323	−.426	−.085	−.036	−.0202	−.0129				
4.0	1.314	−.425	−.085	−.036	−.0202	−.0129				

413072—57——85

TABLE III.—ORIFICE LOCATIONS ON WING AND BODY OF WING-BODY COMBINATION

[Dimensions in inches measured from wing leading edge]

y/a=1.020 [1]	y/a=1.253	y/a=1.916	y/a=2.583	y/a=3.916	θ=90°	θ=45°
0.400	0.400	----------	0.400	----------	−0.281	0.468
.775	.775	0.775	.775	----------	.219	.968
1.150	1.150	1.150	1.150	1.150	.719	1.468
1.525	1.525	1.525	1.525	1.525	1.219	1.968
1.900	1.900	1.900	1.900	1.900	1.719	2.468
2.275	2.275	2.275	2.275	2.275	2.219	2.968
2.650	2.650	2.650	2.650	2.650	2.719	
					3.219	
					3.719	

[1] a=0.75 inch.

TABLE IV.—PRESSURE COEFFICIENTS $\left(\frac{p-p_1}{q_0}\right)$

(a) $M=1.48$, $R=1.5\times10^6$

Station	l_w / x/c	$\alpha_B=-6°$				$\alpha_B=-4°$				$\alpha_B=-2°$				$\alpha_B=0°$			$\alpha_B=2°$				$\alpha_B=4°$				$\alpha_B=6°$			
		−5.7°	−3.8°	−1.9°	0°	−5.7°	−3.8°	−1.9°	0°	−5.7°	−3.8°	−1.9°	0°	−5.7°	−3.8°	−1.9°	−5.7°	−3.8°	−1.9°	0°	−5.7°	−3.8°	−1.9°	0°	−5.7°	−3.8°	−1.9°	0°
$y/s=0.170$	0.133	0.622	0.539	0.431	0.334	0.468	0.384	0.273	0.200	0.300	0.232	0.152	0.095	0.160	0.114	0.064	0.072	0.007	−0.046	−0.092	−0.046	−0.094	−0.139	−0.189	−0.143	−0.193	−0.239	−0.268
	.253	.480	.409	.329	.255	.361	.297	.220	.168	.256	.199	.132	.092	.150	.106	.061	.068	.019	−.032	−.076	−.019	−.064	−.109	−.153	−.098	−.134	−.181	−.221
	.383	.405	.354	.290	.232	.323	.263	.197	.149	.224	.166	.112	.072	.135	.088	.042	.058	.014	−.028	−.066	−.059	−.060	−.091	−.125	−.078	−.105	−.151	−.186
	.508	.406	.330	.266	.205	.307	.238	.167	.133	.211	.157	.112	.080	.129	.085	.046	.061	.020	−.017	−.068	.003	−.023	−.067	−.107	−.049	−.083	−.117	−.155
	.633	.442	.344	.270	.194	.322	.247	.176	.126	.223	.156	.104	.061	.133	.084	.042	.063	.029	−.016	−.065	.003	−.025	−.061	−.096	−.036	−.071	−.102	−.141
	.759	.432	.375	.298	.231	.351	.279	.201	.124	.262	.176	.109	.060	.155	.091	.043	.077	.030	−.013	−.062	.014	−.021	−.059	−.090	−.036	−.069	−.098	−.135
	.884	.409	.360	.297	.246	.345	.281	.232	.154	.296	.209	.125	.060	.188	.110	.046	.102	.034	−.010	−.061	.037	−.021	−.059	−.090	−.037	−.074	−.103	−.130
$y/s=0.208$	.133	.579	.478	.390	.316	.434	.340	.281	.197	.307	.225	.140	.085	.177	.110	.064	.070	.007	−.043	−.092	−.047	−.094	−.147	−.196	−.145	−.193	−.238	−.272
	.256	.486	.412	.332	.266	.374	.298	.229	.174	.272	.202	.147	.085	.162	.102	.050	.072	.016	−.030	−.074	−.015	−.062	−.106	−.152	−.096	−.139	−.199	−.225
	.383	.419	.372	.293	.235	.343	.267	.205	.154	.249	.185	.128	.080	.160	.094	.043	.072	.021	−.021	−.065	−.002	−.046	−.081	−.118	−.089	−.099	−.147	−.185
	.508	.401	.334	.275	.207	.311	.247	.180	.130	.222	.166	.112	.071	.138	.083	.043	.064	.019	−.020	−.069	.005	−.034	−.072	−.111	−.060	−.094	−.127	−.165
	.633	.442	.351	.278	.209	.324	.266	.186	.134	.232	.161	.104	.069	.134	.096	.041	.068	.021	−.015	−.063	.015	−.025	−.002	−.098	−.036	−.072	−.109	−.149
	.759	.431	.371	.301	.232	.354	.288	.213	.138	.250	.187	.106	.066	.160	.094	.042	.081	.026	−.013	−.061	.018	−.023	−.059	−.094	−.033	−.070	−.102	−.137
	.884	.404	.355	.266	.250	.339	.290	.231	.166	.261	.206	.136	.071	.190	.116	.047	.102	.034	−.014	−.063	.024	−.023	−.002	−.100	−.036	−.075	−.105	−.139
$y/s=0.319$	.258	.603	.432	.355	.282	.400	.319	.260	.180	.297	.224	.152	.092	.197	.127	.063	.089	.020	−.038	−.091	−.012	−.060	−.113	−.160	−.098	−.136	−.188	−.227
	.383	.437	.384	.315	.244	.364	.294	.220	.156	.262	.195	.133	.079	.172	.111	.056	.088	.026	−.026	−.081	−.002	−.056	−.100	−.152	−.088	−.138	−.192	−.234
	.508	.392	.345	.302	.224	.331	.274	.207	.144	.251	.180	.122	.071	.159	.102	.051	.068	.028	−.021	−.068	.012	−.039	−.096	−.134	−.060	−.107	−.157	−.202
	.633	.414	.314	.278	.223	.301	.257	.210	.140	.241	.179	.120	.069	.160	.099	.052	.087	.033	−.010	−.060	.022	−.024	−.070	−.113	−.039	−.085	−.133	−.179
	.759	.412	.328	.247	.204	.306	.235	.194	.143	.234	.176	.123	.066	.159	.105	.051	.068	.041	−.007	−.060	.034	−.014	−.059	−.101	−.026	−.068	−.101	−.133
	.884	.360	.323	.254	.189	.305	.231	.176	.123	.210	.159	.113	.066	.142	.096	.055	.089	.043	−.007	−.066	.031	−.016	−.059	−.096	−.036	−.068	−.092	−.140
$y/s=0.431$	.133	.639	.539	.411	.285	.500	.365	.283	.167	.337	.236	.148	.078	.216	.135	.065	.116	.040	−.018	−.076	.020	−.020	−.094	−.142	−.069	−.114	−.161	−.208
	.258	.537	.476	.362	.307	.451	.364	.270	.181	.335	.246	.163	.083	.217	.135	.064	.109	.037	−.021	−.076	.014	−.043	−.097	−.144	−.069	−.118	−.161	−.209
	.383	.456	.413	.368	.265	.395	.328	.245	.170	.304	.234	.160	.095	.201	.129	.063	.099	.038	−.026	−.079	.010	−.047	−.099	−.147	−.073	−.122	−.167	−.213
	.508	.400	.364	.323	.265	.338	.306	.245	.165	.289	.231	.144	.082	.198	.123	.061	.106	.034	−.027	−.085	.010	−.061	−.102	−.150	−.071	−.120	−.170	−.211
	.633	.366	.311	.269	.230	.304	.260	.231	.162	.244	.204	.144	.090	.182	.124	.063	.114	.045	−.015	−.069	.030	−.031	−.085	−.135	−.048	−.102	−.154	−.208
	.759	.366	.362	.216	.177	.347	.296	.171	.154	.190	.167	.117	.071	.130	.099	.053	.090	.040	−.012	−.063	.029	−.026	−.080	−.126	−.046	−.101	−.154	−.202
	.884	.354	.290	.194	.145	.254	.181	.140	.101	.166	.120	.091	.060	.109	.075	.043	.068	.030	−.010	−.069	.020	−.013	−.064	−.133	−.015	−.063	−.127	−.177
$y/s=0.652$	.258	.451	.406	.357	.280	.396	.339	.288	.182	.330	.260	.160	.088	.227	.150	.068	.137	.058	−.013	−.072	.046	−.021	−.083	−.144	−.035	−.093	−.143	−.195
	.508	.358	.318	.274	.227	.305	.263	.211	.148	.249	.195	.128	.072	.178	.117	.057	.106	.045	−.014	−.071	.023	−.029	−.084	−.140	−.047	−.096	−.148	−.197
	.633	.306	.293	.224	.185	.254	.212	.171	.124	.204	.157	.103	.064	.145	.096	.045	.079	.028	−.017	−.069	.012	−.032	−.078	−.120	−.048	−.097	−.136	−.184
	.759	.285	.228	.189	.154	.217	.178	.142	.103	.170	.129	.068	.062	.118	.078	.037	.062	.019	−.020	−.064	.003	−.033	−.069	−.104	−.049	−.092	−.118	−.149
	.884	.310	.206	.104	.133	.196	.155	.122	.091	.147	.111	.076	.047	.100	.068	.031	.053	.015	−.020	−.062	−.001	−.033	−.066	−.080	−.048	−.079	−.094	−.099
$\phi=90°$	−.094	.011	.013	.011	.012	.002	.001	.002	.001	.002	.011	.002	.003	−.002	0	0	−.003	−.002	−.002	0	.001	.002	.003	.003	.008	.006	.009	.008
	.073	.012	.003	.001	.002	.001	−.002	−.001	−.000	.002	.001	.002	.003	−.003	−.001	0	−.004	−.002	−.002	−.001	.001	.007	.003	.003	.012	.013	.013	.013
	.240	.036	.058	.035	.005	.043	.030	.015	.003	.020	.009	.005	.005	.010	.002	.001	.004	.002	.001	−.001	.004	.003	.003	.003	.010	.009	.011	.023
	.410	.480	.345	.068	.051	.318	.139	.070	.033	.198	.115	.064	.021	.109	.066	.020	.041	.007	−.013	−.022	−.005	−.023	−.032	−.034	−.030	−.040	−.045	−.043
	.573	.459	.406	.314	.255	.364	.234	.210	.144	.250	.174	.110	.052	.150	.091	.040	.074	.021	−.020	−.059	.005	−.028	−.069	−.081	−.054	−.057	−.111	−.126
	.740	.445	.393	.334	.236	.381	.308	.211	.157	.278	.186	.119	.070	.168	.102	.048	.087	.030	−.017	−.063	.017	−.031	−.074	−.107	−.049	−.091	−.131	−.102
	.900	.411	.368	.324	.259	.356	.308	.232	.147	.288	.212	.152	.069	.197	.110	.049	.103	.036	−.015	−.069	.026	−.026	−.072	−.111	−.041	−.086	−.130	−.109
	1.073	.346	.325	.293	.205	.306	.274	.242	.178	.248	.214	.148	.070	.189	.134	.054	.124	.045	−.013	−.069	.037	−.021	−.070	−.114	−.035	−.081	−.125	−.108
	1.240	.179	.301	.314	.312	.167	.173	.170	.172	.158	.134	.129	.099	.001	.064	.009	.060	.045	−.011	−.064	.018	−.026	−.075	−.116	−.060	−.091	−.124	−.108
$\phi=45°$	.156	.296	.136	.026	.010	.066	.028	.045	.010	.066	.044	.025	.009	.062	.032	.012	.018	−.001	−.011	−.014	−.013	−.019	−.017	−.014	−.038	−.041	−.045	−.026
	.322	.307	.201	.250	.207	.277	.229	.167	.131	.192	.141	.086	.042	.106	.071	.033	.045	.009	−.023	−.060	−.006	−.043	−.073	−.096	−.064	−.085	−.122	−.145
	.490	.456	.334	.238	.192	.312	.224	.163	.128	.213	.160	.102	.060	.118	.078	.037	.057	.018	−.017	−.064	.006	−.033	−.069	−.092	−.047	−.083	−.112	−.145
	.656	.458	.355	.311	.209	.305	.269	.186	.194	.268	.170	.110	.067	.142	.087	.041	.071	.024	−.017	−.063	.011	−.028	−.063	−.097	−.045	−.080	−.112	−.149
	.823	.422	.374	.318	.200	.306	.295	.229	.161	.273	.202	.117	.070	.172	.100	.046	.065	.026	−.015	−.059	.016	−.025	−.057	−.104	−.046	−.083	−.116	−.158
	.990	.369	.391	.295	.245	.317	.278	.227	.185	.256	.200	.143	.074	.189	.133	.052	.119	.038	−.015	−.068	.027	−.025	−.069	−.111	−.046	−.087	−.121	−.100

TABLE IV.—PRESSURE COEFFICIENTS $\left(\frac{p-p_1}{q_a}\right)$—Continued

(b) $M=1.48$, $R=1.2\times10^6$

Station	i_w / x/c	$\alpha_B=-6°$				$\alpha_B=-4°$				$\alpha_B=-2°$				$\alpha_B=0°$			$\alpha_B=2°$				$\alpha_B=4°$				$\alpha_B=6°$			
		−5.7°	−3.8°	−1.9°	0°	−5.7°	−3.8°	−1.9°	0°	−5.7°	−3.8°	−1.9°	0°	−5.7°	−3.8°	−1.9°	−5.7°	−3.8°	−1.9°	0°	−5.7°	−3.8°	−1.9°	0°	−5.7°	−3.8°	−1.9°	0°
$y/s=0.170$	0.123	0.622	0.510	0.411	0.335	0.453	0.352	0.274	0.200	0.297	0.222	0.151	0.096	0.180	0.113	0.051	0.070	0.001	−0.046	−0.092	−0.048	−0.093	−0.139	−0.178	−0.151	−0.196	−0.231	−0.270
	.238	.475	.404	.322	.262	.363	.295	.230	.174	.255	.190	.132	.081	.157	.105	.048	.076	.017	−.034	−.078	−.023	−.064	−.109	−.150	−.096	−.138	−.182	−.224
	.383	.405	.356	.277	.230	.328	.265	.198	.150	.222	.170	.114	.074	.134	.087	.041	.064	.015	−.029	−.068	−.012	−.055	−.095	−.137	−.071	−.111	−.153	−.194
	.508	.415	.333	.272	.206	.317	.244	.188	.140	.214	.161	.114	.067	.125	.084	.045	.053	.019	−.017	−.059	.003	−.037	−.070	−.114	−.048	−.092	−.120	−.156
	.633	.440	.351	.281	.203	.336	.269	.182	.134	.231	.161	.109	.064	.131	.083	.040	.060	.022	−.013	−.053	.011	−.024	−.068	−.097	−.033	−.066	−.101	−.137
	.759	.434	.376	.299	.238	.352	.282	.209	.137	.253	.184	.110	.063	.150	.092	.042	.080	.031	−.010	−.050	.019	−.019	−.064	−.093	−.029	−.064	−.096	−.128
	.884	.409	.360	.299	.248	.344	.282	.222	.174	.253	.200	.136	.070	.161	.118	.043	.109	.038	−.008	−.049	.030	−.016	−.065	−.099	−.031	−.071	−.101	−.130
$y/s=0.203$	.133	.580	.478	.389	.317	.442	.344	.270	.200	.303	.223	.149	.089	.181	.112	.053	.061	.002	−.047	−.100	−.049	−.093	−.143	−.195	−.155	−.191	−.240	−.280
	.268	.485	.409	.329	.264	.377	.299	.230	.170	.257	.202	.136	.083	.156	.108	.049	.072	.017	−.033	−.080	−.021	−.067	−.111	−.160	−.103	−.143	−.196	−.239
	.383	.434	.373	.302	.233	.350	.286	.206	.155	.244	.182	.129	.077	.148	.098	.045	.077	.022	−.024	−.067	−.005	−.050	−.088	−.128	−.070	−.107	−.148	−.190
	.508	.409	.344	.287	.217	.326	.263	.195	.140	.229	.160	.116	.070	.134	.088	.043	.071	.023	−.014	−.057	.007	−.034	−.074	−.116	−.044	−.083	−.126	−.164
	.633	.441	.350	.287	.222	.329	.263	.195	.142	.231	.166	.111	.068	.134	.084	.040	.070	.023	−.012	−.053	.014	−.025	−.062	−.101	−.033	−.072	−.110	−.147
	.759	.432	.372	.300	.240	.352	.287	.215	.151	.262	.192	.114	.067	.102	.095	.041	.082	.027	−.012	−.051	.021	−.021	−.067	−.094	−.028	−.067	−.101	−.134
	.884	.406	.356	.296	.248	.340	.278	.227	.174	.261	.206	.143	.078	.191	.119	.060	.108	.037	−.011	−.053	.030	−.030	−.067	−.095	−.029	−.071	−.104	−.136
$y/s=0.319$	.268	.501	.430	.349	.280	.408	.319	.246	.186	.295	.224	.153	.093	.198	.137	.061	.084	.018	−.039	−.094	−.018	−.069	−.118	−.165	−.099	−.142	−.190	−.236
	.383	.437	.366	.313	.242	.372	.287	.222	.163	.263	.196	.134	.080	.173	.112	.063	.088	.023	−.029	−.083	−.009	−.068	−.111	−.163	−.090	−.143	−.191	−.236
	.508	.396	.349	.303	.229	.337	.282	.209	.151	.256	.184	.123	.073	.160	.103	.049	.090	.029	−.020	−.068	.011	−.040	−.088	−.136	−.056	−.107	−.155	−.203
	.633	.419	.319	.278	.230	.311	.264	.216	.162	.243	.188	.123	.069	.164	.101	.048	.094	.035	−.013	−.058	.024	−.024	−.068	−.116	−.033	−.085	−.134	−.187
	.759	.411	.329	.254	.207	.312	.244	.198	.153	.224	.179	.131	.072	.157	.100	.051	.101	.043	−.006	−.053	.038	−.012	−.060	−.106	−.021	−.078	−.109	−.133
	.884	.378	.319	.266	.185	.303	.290	.172	.130	.213	.154	.111	.068	.140	.094	.061	.087	.030	−.006	−.054	.034	−.018	−.060	−.106	−.018	−.047	−.094	−.124
$y/s=0.431$	.133	.632	.536	.407	.284	.500	.384	.251	.172	.330	.232	.146	.080	.216	.135	.062	.112	.030	−.020	−.078	.018	−.042	−.090	−.148	−.085	−.115	−.104	−.210
	.268	.533	.473	.379	.297	.450	.354	.266	.188	.333	.247	.164	.084	.217	.135	.062	.111	.036	−.022	−.079	.014	−.044	−.090	−.147	−.070	−.117	−.164	−.209
	.383	.457	.410	.360	.270	.402	.333	.244	.178	.308	.226	.150	.089	.209	.139	.060	.101	.032	−.026	−.080	.011	−.040	−.090	−.146	−.073	−.120	−.166	−.213
	.508	.401	.361	.333	.271	.363	.309	.260	.179	.290	.226	.147	.066	.203	.120	.069	.100	.035	−.025	−.084	.012	−.050	−.104	−.154	−.070	−.122	−.170	−.214
	.633	.395	.304	.267	.227	.295	.250	.216	.170	.258	.198	.143	.064	.178	.134	.060	.115	.045	−.014	−.070	.031	−.031	−.085	−.135	−.044	−.100	−.153	−.204
	.759	.394	.304	.216	.170	.285	.204	.167	.133	.256	.182	.112	.071	.153	.094	.048	.098	.030	−.018	−.064	.027	−.029	−.081	−.128	−.041	−.100	−.154	−.199
	.884	.356	.279	.199	.161	.261	.184	.141	.109	.196	.133	.090	.066	.109	.073	.037	.068	.030	−.009	−.056	.024	−.019	−.070	−.127	−.017	−.074	−.133	−.177
$y/s=0.662$	.333	.440	.396	.348	.276	.388	.331	.251	.184	.314	.237	.157	.088	.221	.147	.069	.137	.056	−.011	−.074	.040	−.022	−.080	−.136	−.031	−.091	−.148	−.190
	.508	.356	.313	.270	.225	.304	.269	.206	.154	.248	.194	.128	.071	.176	.115	.054	.103	.042	−.012	−.074	.023	−.031	−.083	−.134	−.043	−.096	−.148	−.192
	.633	.307	.264	.223	.185	.264	.211	.159	.130	.199	.155	.107	.065	.141	.095	.044	.079	.025	−.017	−.069	.011	−.030	−.076	−.118	−.048	−.098	−.132	−.176
	.759	.294	.230	.190	.157	.221	.180	.143	.112	.169	.130	.088	.054	.119	.078	.037	.061	.017	−.017	−.062	.004	−.034	−.080	−.101	−.040	−.080	−.118	−.162
	.884	.313	.211	.167	.136	.202	.156	.124	.096	.148	.112	.083	.047	.100	.067	.032	.053	.013	−.019	−.060	−.001	−.033	−.066	−.093	−.045	−.072	−.101	−.094
$\phi=90°$	−.094	.012	.013	.013	.014	.003	.005	.003	.007	.003	.003	.002	.001	0	.003	.001	−.002	−.004	0	−.002	.001	.003	.003	.004	.012	.012	.011	.014
	.073	.036	.010	.004	.004	.025	.010	.003	.001	.007	.006	.003	.002	−.002	0	0	−.003	.003	0.000	0	.002	.004	.006	.006	.016	.016	.014	.019
	.240	.052	.069	.067	.029	.068	.047	.044	.027	.029	.021	.016	.009	.011	.005	.001	.006	.002	.002	.001	.006	.005	.006	.006	.018	.014	.016	.031
	.410	.449	.320	.063	.059	.315	.148	.037	.041	.198	.103	.046	.034	.112	.056	.020	.042	.007	−.011	−.020	.003	.020	.029	.031	.031	.043	.042	.036
	.573	.469	.403	.309	.249	.370	.278	.213	.111	.253	.179	.111	.054	.151	.093	.039	.078	.020	−.019	−.061	.005	.030	.068	.091	.038	.068	.114	.128
	.740	.445	.396	.338	.240	.378	.311	.217	.166	.293	.190	.124	.074	.189	.102	.045	.090	.029	−.018	−.069	.017	.033	.078	.112	.048	.092	.134	.104
	.900	.411	.363	.328	.275	.357	.309	.247	.157	.289	.221	.124	.071	.204	.113	.048	.109	.038	−.014	−.069	.029	.030	.073	.118	.038	.085	.131	.109
	1.073	.340	.322	.292	.266	.307	.273	.245	.202	.249	.220	.163	.074	.193	.145	.059	.139	.033	−.010	−.068	.049	.017	.067	.113	.034	.076	.124	.104
	1.240	.174	.196	.207	.206	.185	.169	.176	.173	.122	.133	.134	.111	.068	.093	.073	.004	.070	.001	−.062	.024	.017	.049	.119	.031	.081	.127	.102
$\phi=48°$	.150	.262	.089	.037	.027	.066	.035	.031	.030	.040	.025	.022	.016	.060	.024	.011	.009	−.001	−.007	−.030	−.014	−.008	−.022	−.023	−.030	−.033	−.037	−.019
	.323	.357	.306	.246	.199	.280	.231	.159	.055	.206	.161	.089	.021	.111	.074	.034	.053	.009	−.023	−.069	−.011	−.043	−.070	−.096	−.062	−.098	−.124	−.145
	.489	.429	.354	.344	.192	.342	.292	.178	.141	.216	.163	.116	.062	.118	.077	.035	.059	.018	−.016	−.067	.005	.030	.070	.096	.040	.065	.113	.143
	.656	.454	.394	.315	.209	.371	.296	.191	.136	.264	.177	.119	.073	.145	.090	.041	.074	.025	−.014	−.062	.019	.027	.062	.097	.041	.077	.111	.143
	.823	.421	.374	.317	.265	.354	.299	.243	.102	.277	.211	.125	.072	.153	.100	.044	.090	.029	−.015	−.060	.017	.027	.065	.106	.041	.081	.118	.153
	.990	.386	.340	.299	.251	.315	.279	.231	.195	.256	.211	.165	.081	.191	.142	.058	.133	.046	−.011	−.067	.035	.020	.066	.108	.037	.080	.120	.150

TABLE IV.—PRESSURE COEFFICIENTS $\left(\frac{p-p_1}{q_0}\right)$—Continued

(c) $M=1.48$, $R=6.0\times10^6$

Station	$\frac{t}{w}$ / $\frac{x}{c}$	$\alpha_B=-6°$				$\alpha_B=-4°$				$\alpha_B=-2°$				$\alpha_B=0°$			$\alpha_B=2°$				$\alpha_B=4°$				$\alpha_B=6°$			
		−5.7°	−3.8°	−1.9°	0°	−5.7°	−3.8°	−1.9°	0°	−5.7°	−3.8°	−1.9°	0°	−5.7°	−3.8°	−1.9°	−5.7°	−3.8°	−1.9°	0°	−5.7°	−3.8°	−1.9°	0°	−5.7°	−3.8°	−1.9°	0°
$y/s=0.170$	0.133	0.663	0.525	0.421	0.332	0.470	0.370	0.288	0.218	0.320	0.252	0.167	0.100	0.202	0.121	0.054	0.007	0.003	−0.049	−0.093	−0.046	−0.089	−0.127	−0.171	−0.118	−0.160	−0.203	−0.248
	.258	.508	.406	.324	.255	.378	.300	.232	.173	.263	.211	.148	.086	.162	.111	.047	.073	.016	−.035	−.070	−.019	−.063	−.097	−.141	−.092	−.125	−.161	−.202
	.383	.406	.374	.294	.224	.344	.268	.200	.143	.238	.177	.118	.072	.135	.092	.040	.060	.014	−.031	−.070	−.011	−.052	−.089	−.129	−.073	−.106	−.140	−.181
	.508	.450	.374	.306	.228	.348	.277	.198	.144	.233	.171	.114	.070	.133	.091	.046	.065	.023	−.019	−.060	.007	−.035	−.074	−.114	−.047	−.083	−.140	−.151
	.633	.444	.374	.312	.243	.348	.291	.211	.146	.250	.182	.111	.063	.141	.092	.044	.070	.029	−.016	−.068	.015	−.024	−.067	−.105	−.025	−.062	−.103	−.128
	.759	.420	.370	.307	.251	.342	.287	.232	.172	.251	.202	.124	.066	.165	.102	.047	.036	.033	−.011	−.067	.030	−.016	−.058	−.096	−.011	−.046	−.083	−.096
	.884	.388	.333	.278	.237	.309	.259	.208	.162	.232	.185	.133	.074	.161	.105	.052	.093	.046	−.011	−.063	.041	−.015	−.064	−.106	−.006	−.033	−.093	−.078
$y/s=0.208$	.133	.600	.494	.398	.316	.446	.356	.276	.210	.306	.235	.159	.094	.177	.109	.062	.068	.004	−.047	−.096	−.037	−.094	−.141	−.193	−.139	−.182	−.226	−.271
	.258	.519	.428	.338	.269	.396	.311	.241	.183	.273	.215	.149	.098	.166	.107	.049	.070	.013	−.034	−.080	−.016	−.063	−.108	−.158	−.068	−.133	−.184	−.231
	.383	.478	.395	.314	.243	.367	.296	.218	.163	.247	.191	.133	.096	.154	.101	.047	.072	.021	−.034	−.088	−.002	−.048	−.096	−.145	−.066	−.098	−.153	−.197
	.508	.451	.378	.316	.237	.355	.287	.208	.150	.247	.178	.121	.071	.142	.095	.047	.073	.027	−.031	−.088	.006	−.038	−.074	−.116	−.049	−.092	−.153	−.150
	.633	.439	.371	.312	.249	.346	.289	.217	.149	.253	.185	.118	.067	.149	.095	.049	.077	.031	−.016	−.056	.016	−.038	−.096	−.107	−.026	−.069	−.126	−.130
	.759	.421	.363	.309	.245	.337	.279	.220	.160	.250	.192	.123	.070	.152	.102	.049	.090	.039	−.012	−.057	.033	−.017	−.060	−.101	−.001	−.043	−.111	−.089
	.884	.387	.339	.274	.223	.312	.251	.200	.153	.232	.177	.118	.062	.139	.098	.052	.091	.042	−.013	−.051	.044	−.009	−.061	−.104	−.012	−.046	−.116	−.068
$y/s=0.319$	.258	.526	.453	.360	.282	.427	.334	.255	.191	.303	.233	.157	.094	.188	.125	.060	.093	.028	−.036	−.090	−.003	−.060	−.112	−.165	−.085	−.130	−.183	−.234
	.383	.481	.407	.340	.268	.360	.321	.234	.170	.288	.214	.144	.095	.180	.116	.063	.093	.028	−.028	−.080	.005	−.060	−.101	−.154	−.073	−.121	−.164	−.202
	.508	.449	.371	.323	.260	.353	.307	.226	.167	.276	.213	.137	.079	.178	.113	.062	.096	.034	−.019	−.067	.022	−.031	−.080	−.129	−.040	−.087	−.126	−.185
	.633	.420	.344	.289	.240	.337	.270	.224	.168	.258	.202	.136	.070	.171	.116	.064	.100	.041	−.013	−.061	.034	−.020	−.069	−.117	−.020	−.069	−.131	−.178
	.759	.396	.321	.259	.204	.308	.241	.183	.148	.200	.165	.110	.070	.141	.103	.062	.089	.042	−.012	−.059	.035	−.016	−.068	−.115	−.013	−.068	−.130	−.136
	.884	.372	.307	.245	.188	.263	.223	.167	.124	.193	.143	.097	.069	.119	.082	.043	.073	.037	−.011	−.057	.032	−.011	−.063	−.111	−.000	−.060	−.088	−.071
$y/s=0.431$	.133	.641	.551	.417	.297	.518	.364	.261	.176	.344	.245	.158	.084	.211	.134	.062	.111	.040	−.022	−.079	.023	−.038	−.091	−.147	−.061	−.107	−.152	−.199
	.258	.543	.434	.404	.300	.464	.371	.274	.197	.343	.265	.168	.093	.217	.138	.063	.112	.040	−.023	−.078	.030	−.040	−.090	−.140	−.063	−.108	−.149	−.194
	.383	.470	.420	.375	.302	.408	.369	.278	.192	.333	.250	.183	.090	.218	.132	.061	.112	.039	−.024	−.078	.030	−.041	−.091	−.143	−.062	−.103	−.153	−.197
	.508	.430	.361	.319	.272	.348	.310	.259	.195	.287	.240	.165	.093	.212	.140	.064	.123	.046	−.023	−.083	.029	−.040	−.100	−.154	−.048	−.104	−.160	−.198
	.633	.380	.304	.256	.213	.283	.243	.202	.159	.218	.180	.135	.083	.163	.116	.056	.101	.042	−.018	−.072	.031	−.030	−.085	−.139	−.035	−.090	−.151	−.190
	.759	.339	.286	.225	.178	.204	.208	.163	.127	.177	.147	.104	.064	.127	.092	.046	.078	.030	−.014	−.062	.027	−.022	−.072	−.125	−.022	−.078	−.135	−.165
	.884	.368	.287	.221	.165	.200	.199	.145	.110	.166	.123	.087	.053	.109	.076	.039	.097	.032	−.010	−.060	.027	−.014	−.067	−.108	−.011	−.064	−.111	−.134
$y/s=0.652$	.383	.422	.370	.323	.257	.358	.311	.236	.163	.289	.219	.142	.073	.196	.131	.061	.134	.050	−.012	−.069	.035	−.025	−.082	−.136	−.031	−.085	−.110	−.169
	.508	.372	.316	.272	.224	.303	.260	.209	.155	.239	.194	.128	.069	.173	.114	.057	.090	.030	−.013	−.064	.028	−.020	−.080	−.128	−.034	−.084	−.102	−.157
	.633	.342	.272	.226	.188	.257	.217	.173	.131	.199	.160	.109	.063	.140	.097	.046	.062	.020	−.016	−.066	.023	−.020	−.067	−.104	−.030	−.069	−.125	−.127
	.759	.334	.246	.197	.160	.229	.186	.144	.110	.169	.135	.092	.052	.117	.079	.038	.065	.022	−.016	−.048	.016	−.023	−.066	−.088	−.029	−.058	−.116	−.126
	.884	.319	.241	.181	.141	.221	.167	.128	.098	.151	.119	.082	.046	.103	.069	.033	.060	.021	−.016	−.045	.015	−.023	−.066	−.080	−.024	−.056	−.103	−.096
$\theta=90°$	−.094	.070	.018	.013	.012	.031	.011	.006	.006	.019	.011	.006	.001	.013	.006	.001	.009	−.003	−.003	−.004	−.002	−.002	−.001	0	.012	.010	.012	.020
	.073	.089	.061	.061	.018	.067	.066	.036	.009	.053	.050	.021	.007	.033	.025	.009	.018	.003	−.004	−.004	0	−.002	−.002	−.001	.015	.018	.016	.024
	.240	.275	.110	.067	.070	.102	.074	.067	.035	.058	.056	.049	.026	.031	.032	.028	.017	.007	−.005	−.007	.003	−.003	−.006	−.009	.012	.013	.009	.019
	.410	.369	.308	.182	.093	.291	.172	.074	.036	.144	.092	.049	.038	.038	.027	.022	.015	.012	−.011	−.023	.004	−.014	−.023	−.037	−.012	−.021	−.024	−.012
	.573	.439	.383	.207	.207	.356	.278	.196	.088	.246	.158	.049	.042	.137	.080	.020	.024	.017	−.015	−.041	.014	−.024	−.064	−.078	−.030	−.064	−.090	−.090
	.740	.459	.397	.338	.260	.380	.326	.237	.167	.317	.216	.133	.083	.197	.116	.013	.101	.021	−.016	−.054	.034	−.022	−.066	−.104	−.018	−.068	−.111	−.123
	.906	.428	.364	.320	.277	.389	.312	.257	.181	.302	.248	.154	.060	.236	.145	.030	.162	.033	−.013	−.007	.049	−.015	−.078	−.119	−.001	−.061	−.115	−.145
	1.073	.348	.303	.268	.220	.295	.262	.224	.196	.246	.219	.173	.118	.204	.165	.101	.161	.094	−.008	−.062	.097	−.004	−.060	−.114	.041	−.041	−.094	−.101
	1.240	.172	.178	.189	.178	.139	.164	.154	.145	.100	.126	.118	.111	.087	.090	.085	.063	.060	−.006	−.044	.063	.010	−.044	−.085	.024	0	−.071	−.102
$\theta=45°$	.156	.133	.072	.063	.057	.060	.055	.060	.046	.041	.045	.038	.024	.020	.020	.018	.013	.001	−.014	−.021	−.019	−.033	−.040	−.045	−.006	−.071	−.078	−.086
	.223	.428	.307	.177	.079	.270	.195	.078	.049	.199	.098	.050	.033	.090	.053	.034	.011	.010	−.022	−.042	−.015	−.048	−.075	−.102	−.076	−.102	−.130	−.156
	.439	.471	.406	.300	.215	.370	.271	.196	.158	.220	.172	.119	.064	.128	.091	.024	.063	.018	−.018	−.054	−.004	−.040	−.066	−.099	−.020	−.060	−.083	−.109
	.656	.451	.402	.333	.248	.369	.315	.211	.138	.278	.181	.100	.066	.147	.084	.042	.059	.024	−.017	−.063	.015	−.023	−.059	−.094	−.011	−.053	−.092	−.103
	.823	.411	.374	.294	.273	.346	.299	.250	.184	.273	.237	.141	.062	.204	.117	.041	.107	.033	−.014	−.063	.042	−.012	−.060	−.102	−.009	−.062	−.090	−.112
	.990	.344	.312	.274	.236	.286	.266	.212	.169	.230	.192	.141	.062	.174	.122	.074	.122	.007	−.009	−.064	.048	.006	−.004	−.114	.012	−.043	−.104	−.100

TABLE IV.—PRESSURE COEFFICIENTS $\left(\frac{p-p_1}{q_0}\right)$—Concluded

(d) $M=2.00$, $R=1.5\times10^6$

Station	i_W / x/c	$\alpha_B=-6°$				$\alpha_B=-4°$				$\alpha_B=-2°$				$\alpha_B=0°$				$\alpha_B=2°$				$\alpha_B=4°$				$\alpha_B=6°$			
		−5.7°	−3.8°	−1.9°	0°	−5.7°	−3.8°	−1.9°	0°	−5.7°	−3.8°	−1.9°	0°	−5.7°	−3.8°	−1.9°	0°	−5.7°	−3.8°	−1.9°	0°	−5.7°	−3.8°	−1.9°	0°	−5.7°	−3.8°	−1.9°	0°
$y/s=0.170$	0.133	0.390	0.337		0.231	0.288	0.247	0.196	0.149	0.211	0.164	0.116	0.077	0.113	0.072	0.035	0.024	−0.010	−0.040	−0.072	−0.050	−0.080	−0.107	−0.131	−0.123	−0.148	−0.163	−0.187
	.258	.354	.311		.214	.268	.230	.183	.133	.192	.150	.106	.070	.106	.069	.033	.030	.002	−.029	−.061	−.023	−.069	−.097	−.112	−.099	−.124	−.141	−.165
	.383	.306	.306		.191	.231	.197	.157	.129	.161	.120	.085	.057	.097	.063	.030	.029	−.003	−.032	−.068	−.034	−.067	−.090	−.105	−.093	−.116	−.134	−.155
	.508	.287	.249		.174	.218	.184	.150	.113	.152	.124	.089	.056	.087	.061	.028	.034	.010	−.017	−.048	−.013	−.057	−.082	−.087	−.065	−.083	−.107	−.133
	.633	.302	.229		.169	.198	.168	.135	.103	.130	.111	.080	.051	.081	.057	.020	.035	.011	−.016	−.045	−.010	−.061	−.082	−.080	−.061	−.072	−.092	−.119
	.760	.243	.214		.150	.184	.157	.125	.093	.125	.103	.074	.046	.077	.053	.024	.035	.013	−.012	−.040	−.005	−.036	−.049	−.074	−.041	−.061	−.081	−.106
	.884	.230	.201		.142	.170	.144	.118	.089	.120	.096	.069	.041	.078	.061	.026	.037	.014	−.010	−.035	−.002	−.029	−.048	−.068	−.035	−.055	−.074	−.099
$y/s=0.206$	.133	.396	.337		.236	.317	.252	.200	.161	.212	.164	.118	.076	.118	.072	.034	.027	−.007	−.041	−.074	−.017	−.076	−.106	−.132	−.120	−.143	−.161	−.180
	.258	.347	.294		.204	.276	.226	.181	.140	.191	.148	.105	.069	.109	.067	.031	.027	−.003	−.035	−.065	−.038	−.068	−.097	−.122	−.108	−.134	−.151	−.177
	.383	.316	.270		.187	.250	.207	.166	.128	.175	.136	.097	.063	.098	.063	.029	.028	.002	−.030	−.060	−.020	−.056	−.085	−.110	−.092	−.117	−.137	−.162
	.508	.293	.251		.177	.228	.189	.152	.119	.161	.128	.091	.059	.091	.061	.028	.030	.005	−.024	−.061	−.021	−.046	−.074	−.097	−.078	−.103	−.123	−.147
	.633	.275	.236		.169	.211	.178	.144	.111	.150	.119	.086	.055	.084	.060	.027	.032	.008	−.019	−.047	−.014	−.037	−.064	−.087	−.060	−.088	−.104	−.129
	.759	.261	.229		.161	.200	.170	.137	.106	.141	.113	.081	.054	.082	.056	.026	.036	.013	−.016	−.043	−.007	−.030	−.058	−.079	−.047	−.070	−.090	−.115
	.884	.249	.220		.155	.188	.161	.130	.100	.132	.105	.075	.048	.079	.054	.026	.038	.015	−.012	−.038	−.004	−.028	−.050	−.073	−.030	−.050	−.070	−.106
$y/s=0.319$	.258	.388	.324		.208	.305	.242	.185	.135	.209	.158	.107	.063	.120	.081	.038	.049	.013	−.025	−.059	−.013	−.047	−.080	−.111	−.078	−.101	−.125	−.154
	.383	.349	.298		.201	.275	.227	.180	.135	.197	.150	.103	.063	.121	.078	.037	.047	.013	−.025	−.061	−.018	−.049	−.082	−.112	−.078	−.108	−.131	−.158
	.508	.330	.275		.187	.250	.208	.165	.124	.185	.141	.099	.060	.113	.078	.034	.050	.015	−.022	−.056	−.018	−.046	−.079	−.107	−.080	−.108	−.131	−.158
	.633	.299	.256		.175	.232	.193	.155	.113	.172	.132	.091	.057	.108	.070	.034	.050	.017	−.017	−.055	−.007	−.040	−.072	−.101	−.072	−.102	−.124	−.154
	.759	.279	.239		.161	.216	.179	.141	.104	.160	.124	.085	.051	.102	.067	.032	.050	.018	−.014	−.050	−.004	−.038	−.063	−.090	−.056	−.096	−.120	−.150
	.884	.262	.224		.151	.211	.166	.130	.090	.150	.115	.079	.046	.098	.066	.031	.050	.019	−.012	−.047	0	−.028	−.053	−.076	−.043	−.076	−.100	−.132
$y/s=0.431$	.133	.363	.294		.185	.274	.215	.162	.116	.195	.145	.097	.055	.124	.079	.037	.060	.023	−.014	−.050	.012	−.024	−.068	−.089	−.038	−.070	−.097	−.122
	.258	.335	.295		.182	.270	.216	.163	.118	.196	.146	.096	.053	.125	.081	.039	.060	.023	−.015	−.051	.009	−.027	−.061	−.092	−.041	−.074	−.100	−.130
	.383	.375	.303		.187	.283	.220	.165	.118	.198	.147	.097	.056	.125	.079	.037	.069	.022	−.017	−.053	.004	−.032	−.066	−.097	−.049	−.081	−.106	−.140
	.508	.357	.299		.192	.280	.224	.171	.123	.202	.151	.101	.057	.126	.081	.039	.069	.022	−.016	−.054	0	−.036	−.070	−.101	−.055	−.088	−.112	−.141
	.633	.331	.281		.184	.269	.218	.165	.120	.193	.146	.099	.057	.123	.080	.038	.067	.021	−.017	−.056	−.005	−.040	−.073	−.105	−.063	−.093	−.117	−.147
	.759	.314	.268		.176	.246	.201	.157	.115	.183	.139	.096	.056	.119	.077	.037	.066	.020	−.018	−.055	−.009	−.040	−.076	−.105	−.063	−.097	−.121	−.150
	.884	.297	.253		.166	.232	.190	.148	.108	.163	.132	.000	.053	.114	.074	.035	.067	.021	−.018	−.053	−.008	−.038	−.073	−.101	−.007	−.038	−.122	−.152
$y/s=0.582$	.133	.347	.280		.170	.270	.211	.160	.112	.195	.144	.096	.059	.123	.080	.030	.065	.026	−.013	−.048	.014	−.023	−.060	−.090	−.033	−.067	−.096	−.126
	.258	.356	.286		.173	.270	.209	.156	.110	.191	.140	.092	.061	.122	.078	.030	.061	.025	−.013	−.047	.011	−.024	−.060	−.090	−.033	−.065	−.094	−.125
	.383	.359	.293		.183	.274	.215	.162	.115	.193	.142	.093	.062	.122	.078	.035	.060	.022	−.015	−.048	.008	−.027	−.061	−.090	−.035	−.067	−.094	−.123
	.759	.345	.285		.183	.263	.209	.160	.116	.186	.138	.092	.062	.118	.076	.035	.058	.022	−.016	−.049	.006	−.029	−.063	−.090	−.037	−.068	−.094	−.121
	.884	.317	.268		.177	.248	.193	.152	.112	.174	.130	.088	.060	.110	.070	.033	.053	.020	−.018	−.047	.003	−.029	−.061	−.087	−.038	−.067	−.092	−.120
$\phi=90°$	−.004	.040	.039		.040	.022	.020	.019	.020	.008	.007	.007	.008	−.001	−.001	−.001	−.002	−.001	−.001	−.004	.008	.007	.008	.001	−.002	−.002	−.001	−.004
	.073	.033	.033		.033	.022	.018	.018	.020	.008	.007	.007	.008	0	−.001	0	.006	.004	−.001	0	.013	.013	.013	0	.009	.009	.007	−.004
	.240	.027	.026		.027	.016	.014	.014	.016	.023	.012	.004	.002	.009	.007	.003	.010	.008	0	−.001	.011	.010	.011	.001	.005	.006	.006	−.004
	.410	.031	.042		.028	.027	.031	.014	.011	.032	.028	.020	.007	.016	.013	.007	.010	.009	−.001	−.002	.006	.007	.007	0	.003	.003	.001	−.005
	.573	.195	.073		.039	.134	.046	.036	.022	.031	.025	.021	.015	.021	.008	.004	.022	.012	0	−.001	−.001	.007	−.013	−.015	−.024	−.027	−.029	−.033
	.740	.268	.196		.066	.193	.126	.046	.034	.118	.068	.011	.011	.061	.018	−.002	.039	.013	−.003	−.016	−.006	−.024	−.039	−.048	−.041	−.054	−.061	−.068
	.906	.272	.230		.154	.213	.180	.145	.090	.155	.115	.080	.022	.103	.070	.024	.048	.030	−.009	−.027	−.003	−.029	−.060	−.066	−.044	−.066	−.079	−.093
	1.073	.272	.242		.159	.212	.180	.130	.100	.166	.120	.084	.069	.106	.073	.041	.048	.020	−.013	−.039	−.003	−.033	−.060	−.080	−.045	−.071	−.090	−.109
	1.240	.264	.232		.147	.193	.170	.130	.090	.155	.117	.077	.046	.102	.067	.033	.040	.018	−.018	−.048	−.010	−.036	−.065	−.088	−.046	−.073	−.096	−.120
$\phi=45°$	.156	.004	.021		.003	.003	.026	.012	.004	.027	.022	.010	.009	.011	.009	.006	−.002	0	−.002	−.003	−.005	−.005	−.006	−.006	−.023	−.023	−.022	−.024
	.323	.108	.121		.032	.140	.062	.030	.031	.030	.022	.019	.016	.016	.009	.008	.015	.001	−.011	−.018	−.020	−.031	−.039	−.043	−.060	−.068	−.069	−.074
	.490	.146	.176		.137	.140	.138	.116	.090	.125	.100	.042	.019	.077	.044	.007	.024	.004	−.016	−.034	−.016	−.034	−.043	−.066	−.057	−.076	−.057	−.103
	.666	.217	.186		.143	.166	.142	.122	.093	.130	.106	.061	.054	.074	.053	.028	.029	.009	−.013	−.034	−.012	−.031	−.061	−.070	−.053	−.069	−.086	−.106
	.823	.257	.194		.138	.179	.141	.116	.089	.120	.077	.072	.048	.069	.045	.028	.033	.013	−.009	−.032	−.006	−.024	−.047	−.070	−.044	−.063	−.083	−.109
	.990	.253	.200		.131	.194	.141	.111	.083	.117	.080	.053	.043	.071	.046	.024	.035	.014	−.010	−.034	−.007	−.028	−.058	−.073	−.043	−.065	−.088	−.110